Politecnico di Torino

Politecnico di Torino
Master's Degree in Biomedical Engineering
October 2021

Master's Degree Thesis

Development of artificial intelligence algorithms for optimizing patient positioning for cardiac SPECT in nuclear medicine

---

Candidate:

Davide Tucci
Matriculation number: 269635

Supervisor:

Prof. Filippo Molinari

Co-supervisor:
Eng. Luca Rinaudo

Abstract

Cardiac SPECT is a non-invasive tomographic nuclear medicine technique which allows to perform a myocardial perfusion imaging (MPI). During this procedure, a specifically designed radiotracer is administered to a patient and it concentrates in the heart tissues. The 3D distribution of the radiopharmaceutical activity inside the heart is reconstructed by collecting enough 2D projection images around the patient.
This technique is a powerful tool for coronary artery disease (CAD) diagnosis. Comparing two sets of images, one acquired after a stress test and another in a rest state, a SPECT MPI study highlights possible perfusion defects, which may result in a myocardial ischemia or a myocardial infarction.
D-SPECT is a cardiac-dedicated system which fits the left side of the patient's chest with its curved geometry.
This camera shows a much greater sensitivity, a higher reconstructed resolution and an improved energy resolution, compared to the conventional systems.
The D-SPECT image quality may be degraded by several factors. Detector and patient chair positions are not defined in advance, so that the patient-detector configuration depends on the operator and on the patient characteristics. In addition, the cardiac region should be identified on the pre-scan in order to focus the final acquisition on the heart. This procedure is strongly operator-dependent.
This work was carried out in collaboration with the company Tecnologie Avanzate (Turin, Italy) and it was aimed at developing artificial intelligence algorithms which facilitate cardiac SPECT procedures, providing the operator with indications about the patient positioning and the heart location in the preliminary scan.
711 scans related to 158 different patients were collected, using a D-SPECT system at the Nuclear Medicine Department of the San Giovanni Battista University Hospital of Turin. A graphical user interface (GUI) was developed to allow experts to select the heart position in the pre-scan and to indicate possible corrections to the patient-detector configuration. Specifically, the technicians denoted the pre-scans for which the head detector or the patient chair are not in the right position. They also labelled the acquisitions which presented a great extra-cardiac activity, suggesting the patient to drink cold water.
Support vector machine (SVM) models were trained by using the collected information. A classifier for detecting the heart position was developed, showing a sensitivity up to 96%.
In order to assist the operator during the diagnostic test, two classifiers were developed. One has the aim to distinguish among three different pre-scan categories:

raise the chair, lower the chair or leave the chair as it is for the semi-upright position; move the detector head towards the patient's feet, towards the patient's head or leave the detector head as it is for the supine configuration. The second classifier is useful to discern between two other classes: make the patient drink or not drink cold water, depending on the external activity. On average, these algorithms achieved an accuracy of 71.8%. Even if these algorithms did not achieve optimal results, they are surely a good starting point to make the diagnostic work easier for the operators.

Acknowledgements

Firstly, I would like to thank Prof. Filippo Molinari for the opportunity to work on this project in collaboration with a company.

I would also like to express my gratitude to the company Tecnologie Avanzate and in particular to Eng. Luca Rinaudo, who supported me during my work with patience and dedication.

I would also like to thank Dr. Roberta Casoni and Prof. Desiree Deandreis for allowing me to complete my thesis in a hospital context despite the problems arising from the pandemic situation.

I would also like to say thank you to all the people who have been close to me during my studies.

Thank you, Paola, for believing in me even when I was not able to do it. You have been for me a fellow, a friend, a family. I owe you so much more than these words, but I think you will appreciate to see your real name on my thesis: remember that you are the Fairy of Wonders!

Thank you, Marco, for welcoming me to a safe place to study, taking care of the housework and preparing meals, reminding me when it was time to rest. I hope there is some relaxation for both of us now.

A big thank you also to Carmen and Paolo, because I was able to study many times in your houses looking at your beatiful mountains.

I would also like to thank Daniela and her family for their big warm hearts. She made me feel at ease in the difficult moments of my life.

Thank you, Beatrice, Silvia and Arturo. I know it has not been easy to put up with me over the past two years. Even though our studies took so much effort, I am happy that they allowed me to meet faithful friends like you. Now it's time to plan another beautiful trip!

Thank you, Erika, for being my best friend for over fourteen years. During all this time we have given ourselves many gifts, but in this moment I am giving you a very special one. Have you ever thought your name would end up on an engineering thesis? I hope that we will be able to celebrate this milestone together, remembering where we started from and imagining where we would go.

One of my thanks is going very far, to my Icelandic friends, Kristján and Hjördís, the Chief and the Cat Lady, who make me feel at home in the most colorful and warmest house in the world!
Finally, I would like to say thank you to my family. Without a family the life of a person would be completely different. I hope this achievement will make you happy and proud. A big thank you especially to my grandpa Mimì, our light in the dark.

Contents

List of Figures

List of Tables

Acronyms

1D One-Dimensional.

2D Two-Dimensional.

3D Three-Dimensional.

ATP Adenosine Triphosphate.

AV Atrio-Ventricular.

BMI Body Mass Index.

CAD Coronary Artery Disease.

CT Computed Tomography.

CZT Cadmium Zinc Telluride.

ECG Electrocardiogram.

ECT Emission Computed Tomography.

EDV End Diastolic Volume.

FOV Field Of View.

FWHM Full Width at Half Maximum.

GLCM Gray-Level Co-occurence Matrix.

GUI Graphical User Interface.

HEGP High-Energy General Purpose.

HLA Horizontal Long Axis.

LA Left Atrium.

LEAP Low-Energy All-Purpose.

LEGP Low-Energy General Purpose.

LEHR Low-Energy High-Resolution.

LSF Line Spread Function.

LV Left Ventricle.

LVEDV Left Ventricle End Diastolic Volume.

LVEF Left Ventricle Ejection Fraction.

MEGP Medium-Energy General Purpose.

MPI Myocardial Perfusion Imaging.

MRT Magnetic Resonance Tomography.

OOB Out Of Bag.

PET Positron Emission Tomography.

PHA Pulse Height Analyzer.

PMT Photomultiplier Tube.

QC Quality Control.

RA Right Atrium.

ROI Region Of Interest.

RSNA Radiological Society of North America.

RV Right Ventricle.

SA Short Axis.

SI International System.

SNR Signal-to-Noise Ratio.

SOM Self-Organizing Map.

SPECT Single Photon Emission Computed Tomography.

SVM Support Vector Machine.

US Ultrasound.

VLA Vertical Long Axis.

Chapter 1

Introduction

Single-photon emission computed tomography (SPECT) belongs to tomographic nuclear medicine techniques. This method allows to acquire medical images non-invasively. A radiopharmaceutical is administered to the patient and it is specifically designed to spread in the organs whose metabolic activity is to be studied. The radiotracer is able to emit gamma-rays which are collected by one or more gamma-cameras, responsible for the conversion of the gamma-photons into images. Acquiring several 2D projection of the radioactivity, it is possible to reconstruct the 3D distribution of the radionuclide inside the region of interest.
The procedure just mentioned can be aimed at analyzing blood perfusion through the myocardium and it is known as cardiac SPECT or SPECT-Myocardial Perfusion Imaging (MPI). This technique is among the most applied to diagnose a coronary artery disease (CAD), which is the first cause of death in Western world [55].
Conventional SPECT detectors are often characterized by a low sensitivity, since almost all the emitted photons are absorbed by the collimator. New cardiac-dedicated cameras, such as the D-SPECT, have been developed in order to improve the image quality. In the D-SPECT system, the camera consists of 9 pixelated CZT detector columns, arranged in a curved configuration that encloses the left side of the patient's chest. The final acquisition is always preceded by a short-lasting pre-scan. The operator indicates the heart region on these preliminary images, so that the detectors can focus the sampling on the patient's heart. A wide-angle collimator combined with a fast region-centric acquisition allows the device to obtain a much higher sensitivity compared to the traditional systems.
Performing a diagnostic test using D-SPECT can present some issues, since several factors may affect the quality of the produced images. The operator should choose the correct position for the patient, in order to place the heart as close as possible to the detector. Even if a good patient/detector configuration is found, the acquisition may become critical in presence of particular patient characteristics, such

as a high BMI or restricted mobility. As previously mentioned, the technician is also responsible for selecting a ROI which encloses the heart activity in the pre-scan images. High extra-cardiac activity can increase the complexity of this task; artifacts may appear in the reconstructed images if a wrong ROI positioning is performed.
The purpose of this work is to create a system that supports medical staff during these procedures, by using artificial intelligence algorithms. The software should provide possible corrections of the patient positioning and also detect the heart location in the pre-scan images.
This manuscript is organized as follows. Chapter 2 contains the information about the context within which this study is inserted, from the function and assessment of the heart to the definition of a D-SPECT system. In Chapter 3 the methods adopted for this work are described, whilst the obtained results are reported in Chapter 4. These results are analyzed and discussed in Chapter 5 and, finally, the conclusions of this work are reported in Chapter 6.

Chapter 2

Background

2.1 Function and assessment of the heart

2.1.1 Anatomy of the heart

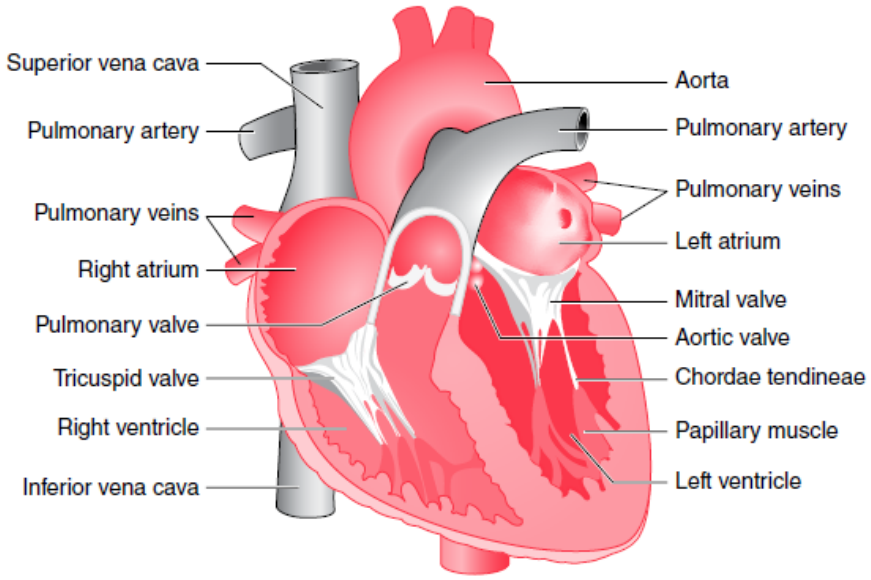

Figure 2.1.1: Cardiac anatomy [36].

The heart is a muscular, cone-shaped organ which consists of four hollow chambers: the two upper chambers called atria and the two ventricles below (figure 2.1.1). Heart muscle can be considered as a double pump, in which the left and right sides work separately at different pressure levels [52].

The concurrent pumping of both sides allows heart to perform its functions correctly. The top part of the heart is called base and it connects to the aorta, vena cava, pulmonary arteries and veins. The apex corresponds to the bottom of the heart [32].
The atria and the ventricles are separated by the annulus fibrosus (also called atrio-ventricular ring), a layer of connective tissue which constitutes the cardiac skeleton. The task of maintaining blood flow in the forward direction rests with the valves, which form a part of the AV ring and open or close depending on the pressure gradient. A muscular wall, named septum, vertically separates the two parts of the heart: interatrial septum divides the two atria and the two ventricles are split by interventricular septum [36].
The heart is characterized by a three-layer wall, composed by the pericardium, the myocardium and the endocardium. The heart, the roots of the aorta and pulmonary arterial trunk are enclosed by the pericardium. This is the external layer of the cardiac wall and it in turn is formed by an outer fibrous layer and an internal serous layer (also known as epicardium). The space between these two layers is filled by a fluid, which decreases friction during myocardial contraction. Cardiac muscle cells known as myocytes populate the thick middle layer of the heart wall, the myocardium. Surrounded by connective tissue and a network of capillaries, myocytes are responsible for the heart contraction. The endocardium is the inner layer and is composed of a continuous layer of endothelial cells, which facilitates blood flow through the heart chambers [36].

2.1.2 The cardiac cycle

The cardiac cycle is composed by two main stages: the phase of myocardial relaxation is called ventricular diastole, during which the ventricles dilate to enable blood entering; on the other hand, during ventricular systole the ventricles contract to force the blood out into the arteries. A rate of approximately 70-75 cycles per minute is maintained at rest and it decreases during sleep [52].
Two circulatory cycles carry blood to and from the heart, the pulmonary and systemic circulation. Right atrium (RA) and right ventricle (RV) are involved in pulmonary circulation (figure 2.1.2). Deoxygenated blood from the body is drained into the RA by the superior and inferior vena cava. Also the coronary sinus, a large cardiac vein, enables the return of deoxygenated blood from the myocardium to the RA. The valves that connect each atrium to the corresponding ventricle are called atrioventricular valves. The right atrioventricular valve, also known as tricuspid valve, opens to enable deoxygenated blood to enter the RV and the ventricular diastole phase starts. The atrial kick indicates the additional blood pressure obtained by the atrial contraction, which increases the end diastolic volume (EDV) of the ventricles. Then, the systole period begins, during which the

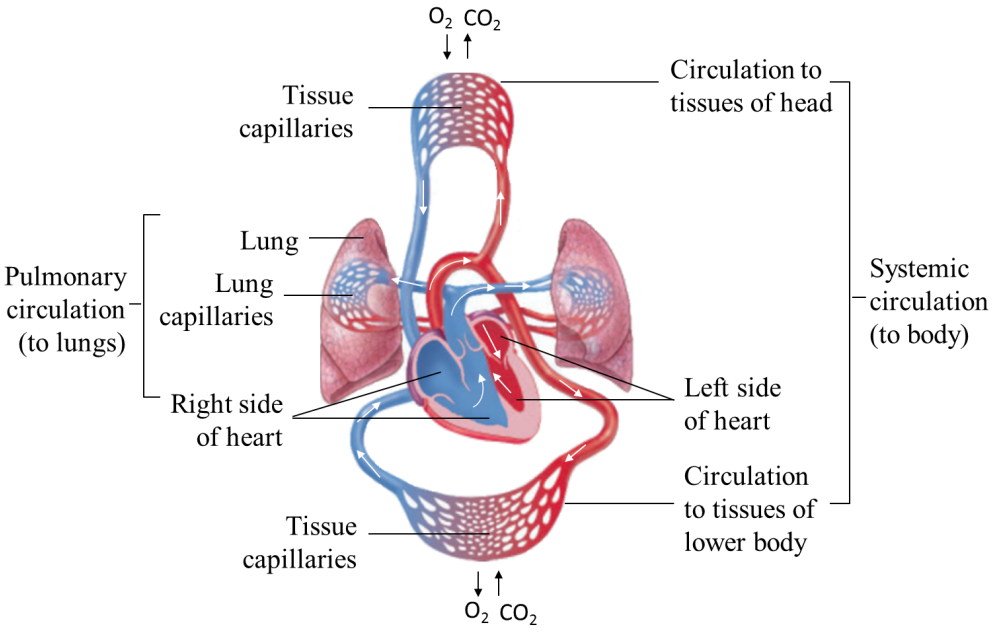

Figure 2.1.2: Systemic and pulmonary circulation. Deoxygenated blood is represented in the color blue and oxygenated blood in red. White arrows represents the blood flow. Image adapted [46].

tricuspid valve is closed thanks to the three papillary muscles contraction. In this way blood regurgitation into the RA is prevented. The pulmonary (semilunar) valve opens only when RV pressure is higher than the pressure within the pulmonary circulation. The blood flows into the pulmonary arterial trunk until a new ventricular diastole starts, closing the pulmonary valve and enabling blood to enter again the RV [36].

Within the alveoli and pulmonary capillaries gaseous exchange occurs: carbon dioxide is released into the lungs and the blood is enriched with oxygen. Systemic circulation involves left atrium (LA) and left ventricle (LV). Four pulmonary veins carry oxygenated blood to the LA. The left atrioventricular valve, named bicuspid or mitral valve, is forced to open by the pressure increase within the LA and the blood starts entering the LV. According to Frank-Starling Law, if a larger volume of blood flows into the ventricle during diastole period, ventricular myocites will be more stretched, enabling an increase in the contraction force during systolic phase. Also in this case, once systolic contraction begins, the mitral valve is closed by the two papillary muscles contraction preventing regurgitation. The pressure within the LV continues to increase until it exceeds the pressure in the aorta, causing the aortic (semilunar) valve opening. The amount of blood that is pushed into the systemic circulation, in order to reach all the tissues of the body, is named stroke

volume. The ejection fraction of the LV (LVEF) is defined as the ratio between stroke volume and the left ventricular EDV (LVEDV). Its range of values at rest is approximately 60-70%. When systole ends and diastole starts again, a little portion of blood in the aorta fall back towards the LV, enabling the aortic valve closing and the coronary arteries perfusion [36].
Oxygenated blood and nutrients are transported to the heart tissues by coronary arterial circulation (figure 2.1.3). The two main arteries of these circulation are the left and right coronary arteries, which stem from the root of the aorta and penetrate the myocardium. The coronary veins are responsible of the venous return from the heart. These veins drain into the coronary sinus, which carries the deoxygenated blood to the vena cava [57].

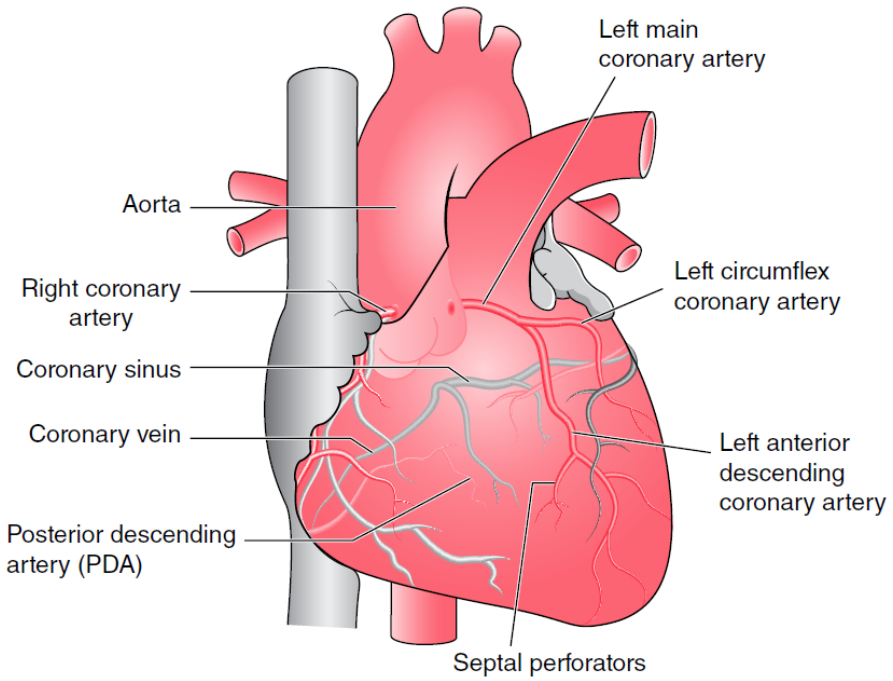

Figure 2.1.3: Coronary circulation [36].

2.1.3 Cardiac conduction system and the electrocardiogram (ECG)

Within the myocardium specialised myocytes, which generate and transmit an electrical impulse across the heart, constitute the cardiac conduction system (figure 2.1.4). The sino-atrial node, composed by special pacemaker cells, is located on the posterior wall of the RA. These self-excitable cells are able to spontaneously

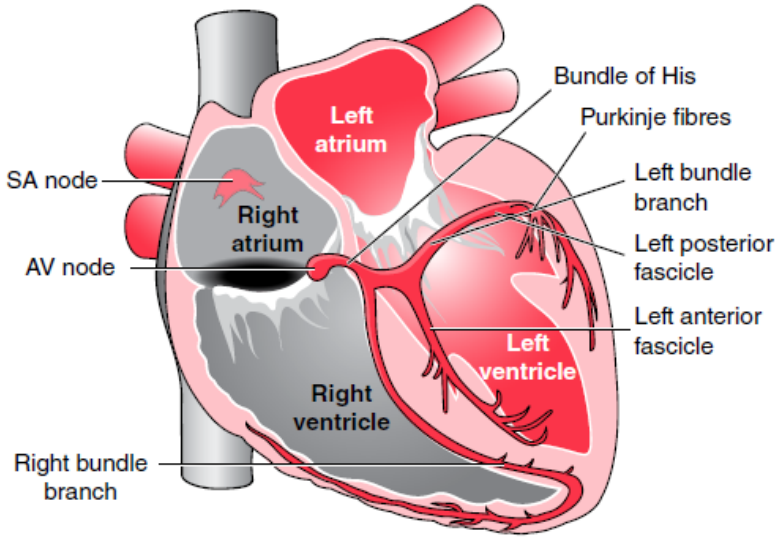

Figure 2.1.4: Cardiac conduction system. SA: sino-atrial. AV: atrio-ventricular [36].

depolarise without an external stimulus, determining the heart rate. The impulse produced by the sino-atrial node is transferred to the surrounding atrial myocytes by transition cells, provoking depolarisation and contraction in both atria. Once the stimulus reaches the AV node, its direct transmission to the ventricles is impeded by the AV ring and the impulse is transmitted to His-Purkinje system. The Bundle of His conducts the stimulus rapidly to two bundle branch systems. Conduction to the RV is provided by the right bundle branch. The left bundle branch divide into two branches named fascicles: the stimulus reaches anterior and lateral walls of the LV by the left anterior fascicle whilst the left posterior fascicle allows to stimulate the posterior wall of the LV. All these branches are connected to a network of Purkinje fibres, which transfer the impulse to the papillary muscles and then very fast to the myocardial cells of the ventricles. It takes less than 200 ms for the electrical impulse to travel from the sinus node to the myocardial cells in the ventricles [36].

The propagation of the cardiac electrical activity can be recorded externally and it is commonly called electrocardiogram (ECG), which is detected by electrodes attached to the skin. The signal has a special shape that repeats with a certain rate, imposed by the pacemaker cells. The repeated sequence is formed by the P and T waves and the QRS complex. The P wave is produced by the depolarization of the atria, the QRS complex corresponds to the ventricular depolarization and during repolarization of the ventricles T wave is created. Since atrial repolarization

is contemporary with depolarization of the ventricles, it is hidden by the QRS complex which presents an higher amplitude [52]. Figure 2.1.5 shows how left ventricular volume changes related to the ECG cycle.

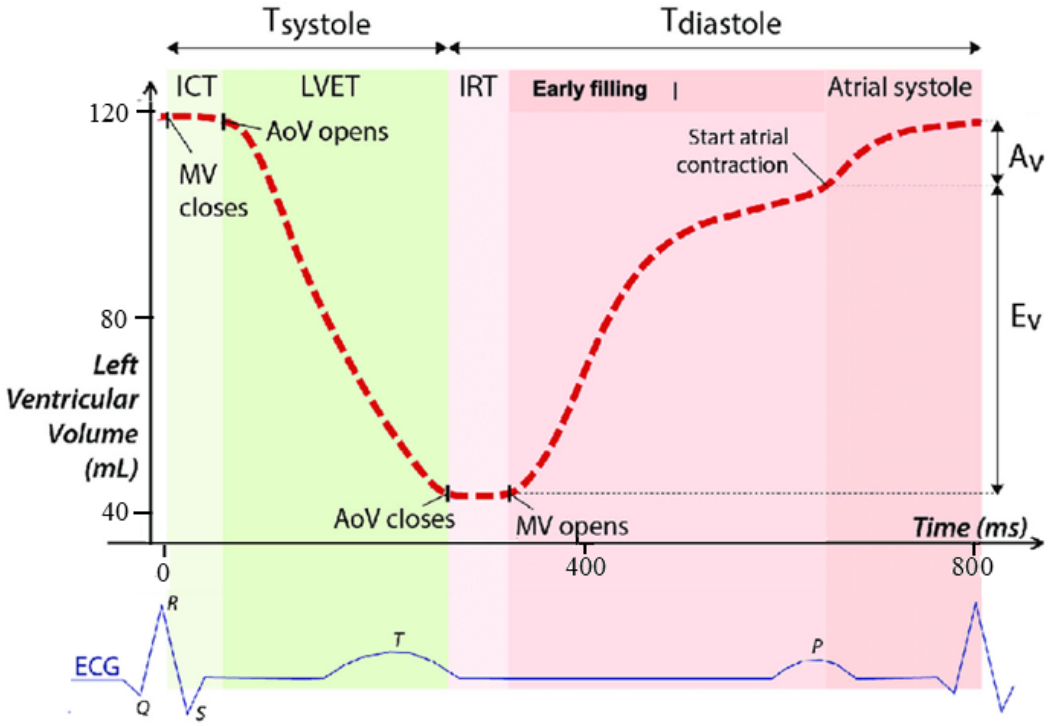

Figure 2.1.5: LV volume related the ECG cycle. The red dashed line represents the LV volume-time curve and the blue track at the bottom corresponds to an ECG cycle. $T_{systole}$: time from the R-peak of the ECG to the end of the systole. $T_{diastole}$: time from the end of the systole to the end of the diastole. ICT: isovolumetric contraction time. LVET:left ventricular ejection time. IRT: isovolumetric relaxation time. E_V: early volume increase. A_V: late volume increase due to atrial contraction (atrial kick). AoV: aortic valve. MV: mitralic valve. Image adapted [31].

2.1.4 Coronary artery disease (CAD)

Coronary Artery Disease, also known as atherosclerotic heart disease or coronary heart disease, is the most common cardiovascular disease [21]. Although the risk of death from CAD decreased between 1980 and 2010 for a given age in developed countries [40], this disease remains the first cause of death in Italy and in the

Western world [55]. Smoking, diabetes, obesity, high blood pressure, alcohol abuse, lack of exercise and high blood cholesterol are considered risk factors [39].
CAD occurs when coronary arteries fail to supply oxygen and nutrients (e.g. adenosine triphosphate, ATP) to the heart muscle cells [35]. The blood flow is hindered by the buildup of atheromatous plaques, which are made up of fat, cholesterol, calcium, and other substances found in the blood [45]. Coronary artery stenosis refers to an abnormal narrowing of coronary arteries (figure 2.1.6) and it can cause angina pectoris (i.e. chest pain, also named angina), myocardial infarction and sudden cardiac death [58].

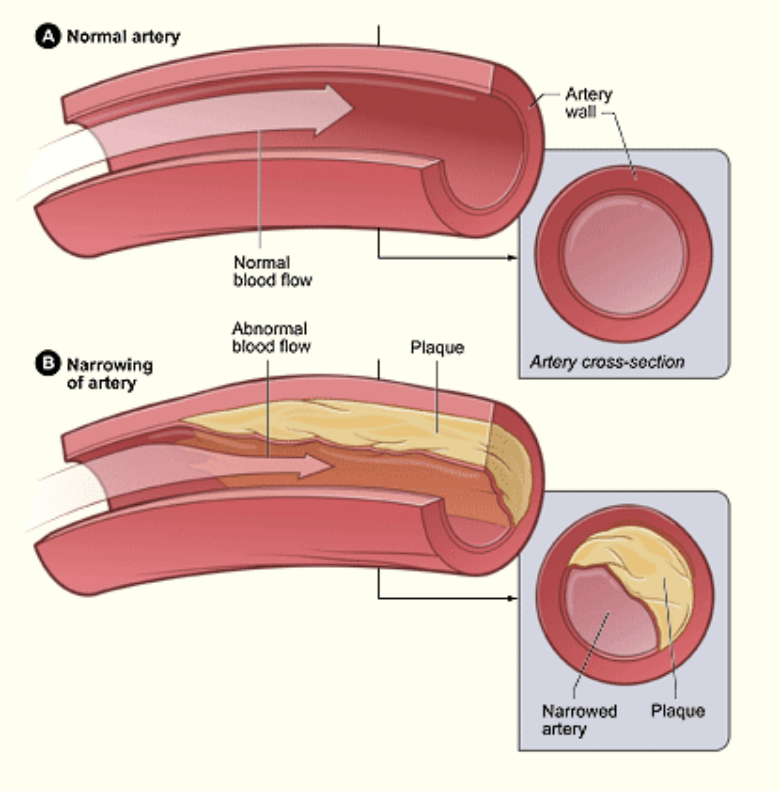

Figure 2.1.6: Plaque buildup in an artery. A normal artery allows a normal blood flow, whilst the presence of a plaque hinders the blood flow, making the artery narrower. Image adapted [50].

When myocardial metabolic need is not satisfied by the blood perfusion, ischemia occurs. This condition can be followed by a cascade of events, from a pure metabolic disturbance to cell death [43]. If the perfusion reduction persists, it causes an impaired myocardial relaxation: energy is needed during relaxation phase, so this is the first affected process when supply of ATP is reduced by ischemia [19]. This phenomenon can trigger diastolic dysfunction, which includes a

severe increase in the filling pressure of the LV, perceived by the patient as breathlessness condition [3]. ATP insufficiency can cause alterations in depolarization and repolarization processes, which can be observed as changes in the ECG [28]. Moreover, the accumulation of metabolites and adenosine causes the patient to experience chest pain [53]. If the ischemic condition lasts enough, an irreversible cell rupture and necrosis occurs, known as myocardial infarction. It is also possible that an ischemic event occurs without cell death: in this case the heart presents a normal perfusion at rest, so a physical stress testing is needed to identify ischemia [28].

2.2 Nuclear Medicine: physical principles

Unless otherwise indicated, sections 2.2, 2.3, 2.4 refer to the contents of "Bioimmagini" course held by Prof. Filippo Molinari at the Politecnico di Torino.
Single-photon emission computed tomography (SPECT) is a medical imaging procedure which, together with positron emission tomography (PET), belongs to tomographic nuclear medicine techniques. Whereas computed tomography (CT), magnetic resonance tomography (MRT) and diagnostic ultrasound (US) allow to obtain an anatomical description of the analyzed volume, the peculiarity of nuclear medicine methods lies in providing functional information, monitoring the metabolic activity in the scanned region. This characteristic is obtained by an emission imaging procedure, based on a radiation source located inside the patient's body: a radiopharmaceutical, which consists of a specific ligand involved in physiological processes labeled with a γ-emitting radionuclide, is administered to the patient (by injection, inhalation or ingestion). A gamma camera (or Anger camera) is used to collect γ-ray photons and it provides a two-dimensional projection image. Acquiring multiple projections at different views around the patient, an estimate of the three-dimensional radiopharmaceutical distribution is obtained, applying a tomographic reconstruction algorithm.

2.2.1 Basic physical principles

A radionuclide, or radioisotope, is an atom in an unstable state due to an excess of protons or neutrons at the nucleus level. In this condition, the atom tries to return to a stable state by carrying out a certain number of spontaneous disintegrations of its own nucleus; this process is called radioactive decay and it involves emission of radiation by the unstable nucleus with consequent loss of energy.
The activity in nuclear physics is the ability of a radioactive material to produce radiation by means of a certain number of spontaneous nuclear disintegrations in the unit of time. The becquerel (symbol: Bq) is the derived unit of activity for the International System of Units (SI, abbreviated from the French translation).

One becquerel is defined as the activity of a radioactive material in which one nucleus decays per second (i.e. one nuclear disintegration per second). For nuclear medicine applications, the becquerel is a small unit, so that the curie (Ci) is usually preferred. The curie is an older, non-SI unit of radioactivity defined as the activity of one gram of radium-226. One curie corresponds to 37 GBq.
The time necessary for the stabilization of a single radionuclide is stochastic. The decay follows a statistical law which is based on a Poisson distribution. This means that the decay rate can be studied on a macroscopic level: considering an object composed by a single chemical element which contains N_0 active radioisotopes at the instant t_0, the number of radioactive atoms N, which have not yet disintegrated at the instant t, can be calculated by (2.2.1), in which λ is the decay constant of the considered radionuclide.

$$N(t) = N_0 \cdot e^{-\lambda(t-t_0)} \tag{2.2.1}$$

The time required for the number of radioactive atoms to reduce to half of its initial value is called half-life ($T_{1/2}$) and its formula is (2.2.2).

$$T_{1/2} = \frac{\ln 2}{\lambda} \tag{2.2.2}$$

2.2.2 Radioactive decay mechanisms

There are many different types of radioactive decay, depending on the radiation emitted. Those most closely related to the field of nuclear medicine are listed here:

- In **α-decay** an heavy atomic nucleus emits an alpha particle, which consists of two neutrons and two protons bound together. Since the number of protons changes, an atom of a different chemical element is created, with a mass number reduced by four and an atomic number reduced by two. Alpha particles are absorbed by the surrounding matter because of their relatively large mass and their electric charge of $+2e$ (e stands for elementary charge). Hence these particles are not used in imaging but they can have a therapeutic use. For example, radium-226 decays in radon-222 with an α-decay:

$$^{226}_{88}\mathrm{Ra} \rightarrow {}^{222}_{86}\mathrm{Rn} + \alpha \tag{2.2.3}$$

- In **β-decay** a beta particle (electron or positron) is emitted and it takes place in two ways:

  1. **β^--decay** is typical of neutron-rich nuclei. A neutron transforms in a proton and the nucleus emits an electron (e^-) and an antineutrino ($\bar{\nu}_e$). The atomic number increases by one but the mass number remains

constant. The emitted electrons do not exit from the body because of their low energy. Therefore also these particles are not useful for imaging purposes. An example of this form of decay is given by molybdenum-99 which decays in technetium-99m:

$$^{99}_{42}\mathrm{Mo} \rightarrow {}^{99m}_{43}\mathrm{Tc} + e^- + \bar{\nu}_e \tag{2.2.4}$$

The production of technetium-99m is very important for nuclear medicine as it is one of the most used radionuclides in SPECT imaging.

2. On the contrary, proton-rich nuclei usually undergo a **β^+-decay**, in which a proton transforms in a neutron and the nucleus emits a positron (e^+) and a neutrino (ν_e) in so-called positron emission. The atomic number decreases by one but the mass number remains constant. This type of decay occurs only when the energy difference between the decaying nucleus (called parent radionuclide) and the produced nuclide (called daughter radionuclide) is equal to 1022 keV. This is the case of gallium-68 which becomes zinc-68:

$$^{68}_{31}\mathrm{Ga} \rightarrow {}^{68}_{30}\mathrm{Zn} + e^+ + \nu_e \tag{2.2.5}$$

β^+-decay is at the basis of PET imaging. Emitted positron loses its energy very rapidly because of the interactions with atomic electrons in the tissue. Then it annihilates with an electron, producing an energy of 1022 keV, which is released in the form of two colinear γ photons, each with an energy of 511 keV. These annihilation photons are so energetic that they are likely to escape the human body and can be detected by an external device.

- **γ-decay** normally follows other forms of decay, such as α-decay or β-decay: after an alpha or a beta particle is emitted, the obtained nucleus is usually left in an excited state and it can decay by emitting a γ-ray photon. An example of γ-decay is the decay scheme of cobalt-60: first a β^--decay occurs from cobalt-60 to excited nichel-60 and then excited nichel-60 decays to the ground state by emitting gamma rays.

$$^{60}_{27}\mathrm{Co} \rightarrow {}^{60}_{28}\mathrm{Ni} + e^- + \bar{\nu}_e + \gamma \tag{2.2.6}$$

- **electron capture** occurs when a proton-rich nucleus absorbes an inner atomic electron, causing the transformation of a proton into a neutron and the emission of a neutrino. The mass number does not change but the atomic number decreases by one. If the resulting daughter radionuclide is in an excited state, then it returns to its ground state. Usually, a gamma ray is emitted during this transition. Iodine-123 follows this decay mechanism:

$$^{123}_{53}\mathrm{I} + e^+ \rightarrow {}^{123}_{52}\mathrm{Te} + \nu_e + \gamma \tag{2.2.7}$$

- **isomeric transition** is similar to any gamma emission, but it involves the intermediate metastable excited state of the nuclei. Nuclides with equal atomic number and equal mass number, but in a different energy state are known as nuclear isomers. Atoms can show an excited nuclear state that follows the emission of a β-particle or other type of excitation. In some cases, these nuclei are able to stay in a metastable state for a long time (hours, days and sometimes much longer) before undergoing γ-decay. These long-lived excited radionuclides are known as isomeric states (or isomers) and their decay is termed isomeric transitions. An example is the decay of the isomer or metastable state of technetium, named technetium-99m:

$$^{99m}_{43}\mathrm{Tc} \rightarrow ^{99}_{43}\mathrm{Tc} + \gamma \tag{2.2.8}$$

  SPECT, unlike PET, uses radionuclides emitting a single γ-photon at each disintegration. These radioisotopes decay by electron capture or by isomeric transition.

2.2.3 Gamma-photons interactions

Gamma-ray photons are the radiations that are imaged in both PET and SPECT. These particles interact with matter (crystals, tissues, etc.) in different ways:

- **Photoelectric effect**: it consists in the emission of an electron (called photoelectron) from an atom caused by an interaction with an incident γ-photon, which gives all its energy to the photoelectron. This can happen if the photon has a characteristic energy (proportional to its frequency) higher than the binding energy of the electron. This process consists in a total conversion of the photon electromagnetic energy into the electron kinetic energy. Also, vacancy created by the emission of the photoelectron is filled by a more external electron, with a lower energy. Therefore, the energy difference is emitted in the form of a photon and this process is called scintillation.

- **Compton scattering**: a γ-photon interacts with an electron weakly bound to the atom of the material, but in this case only a part of the photon's energy is used to emit the electron (here called Compton electron). The remaining energy appears as a scattered photon (called Compton photon) which propagates in a direction different from the incident photon's one. A photon can undergo Compton scattering several times and also terminate its path by a photoelectric effect event.

- **Pair production**: it refers to a γ-photon creating an electron-positron pair near a nucleus. This mechanism can caused only by photons with an energy above the threshold of 1022 keV, corresponding to the energy of the two

generated particles. Excess energy is converted into kinetic energy of the new particles. Then, the produced positron annihilates with an atomic electron.

2.3 Gamma camera

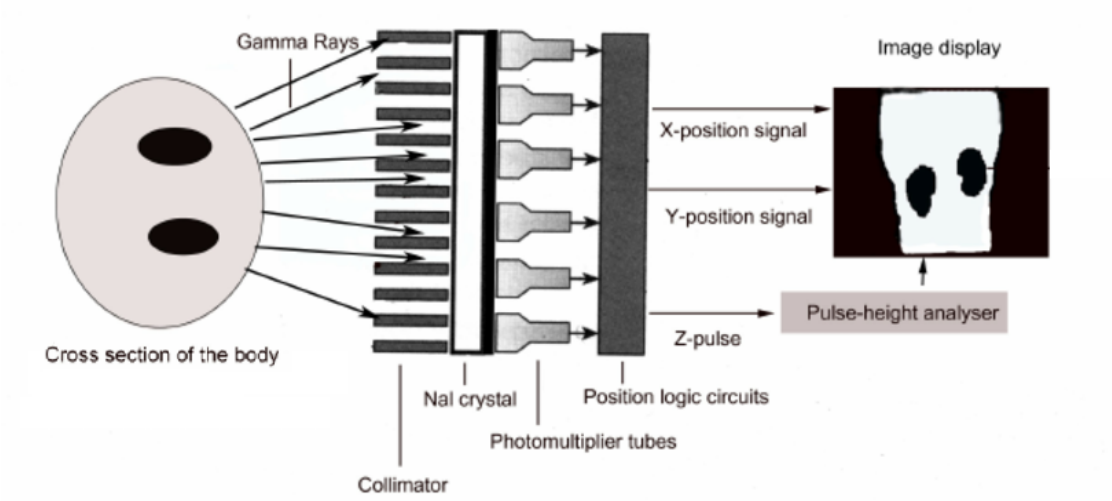

Figure 2.3.1: Basic components of a gamma camera. The schematics include a collimator, a scintillation crystal, a phomultiplier tubes array, analogue electronics for position encoding, a pulse height analyzer and a monitor for image display. The patient's black areas represent the source of activity. Image adapted [26].

A gamma camera, also called Anger camera because it was developed by Hal Anger in 1957, is the basis of the traditional SPECT and PET scanners and also modern cameras still rely on the original Anger's design. This detector system, as shown in figure 2.3.1, consists of a collimator, a scintillation crystal (called scintillator), an array of photomultiplier tubes (PMTs), an analogue electronics for position encoding and a pulse height analyzer (PHA).

2.3.1 Collimator

The first piece of hardware met by the γ-rays is the collimator. As with all forms of electromagnetic radiation, photons are emitted isotropically so, simply using a detector, it would be impossible to determine the position from which the photon started. The collimator, usually a slab of lead with several tens of thousands of holes covering the scintillator surface, only allows the γ-rays from inside the field

of view of the camera to reach the crystal. The lead walls between the holes, called septa, absorb most photons and only the ones aligned with the collimator will interact with the crystal. The geometry of the collimator ensures that the position of the photon is well determined.
As shown in figure 2.3.2, from an area where the radiopharmaceutical is concentrated, the γ-photons emitted by the radionuclides can follow different paths:

a) a particularly dense tissue totally absorbs photon's energy, preventing it from reaching the detector;

b) a photon moves along a direction parallel to the collimator and it can reach the scintillator;

c) a photon is aligned with the collimator but it is deflected by a Compton scattering event and it is absorbed by the collimator due to its new direction;

d) a not-aligned photon is scattered and then it moves in a direction parallel to the collimator, so that it can interact with the crystal;

e) a not-aligned photon, which is not scattered, is absorbed by the collimator.

A heavy price is paid for using the technique of collimation because the vast majority of emitted photons (tipically well over 99.95%) is wasted. Thus collimation, although essential to image formation, severely limits the sensitivity of the device (i.e. the probability of detecting a photon incident upon the detector, commonly quantified as the number of detected counts per unit time per unit source activity for a specified energy window).
The design of the collimator depends on the γ-ray energy and the trade-off between photon count sensitivity and spatial resolution. Indeed, an increase of the collimator hole size and a decrease of the hole length cause a greater sensitivity but also a loss of spatial resolution.
Another drawback introduced by the collimation is the influence of the distance between the photon source and the gamma camera on the spatial resolution. Figure 2.3.3 shows that if the radioactive source is located near the camera, the collimator stops an higher percentage of photons; indeed, a steeper projected radiation profile is obtained, because the collimator acts as a more selective spatial filter. Therefore, positioning the patient as close as possible to the gamma-camera during a nuclear medicine examination, a better spatial resolution is achieved.

There are different kinds of collimators depending on their field of view. They can be parallel-hole, converging, diverging and pinhole collimators (figure 2.3.4). Parallel-hole collimators are the most commonly used in nuclear medicine as it gives a one-to-one projected image. Factors affecting their performances are shown

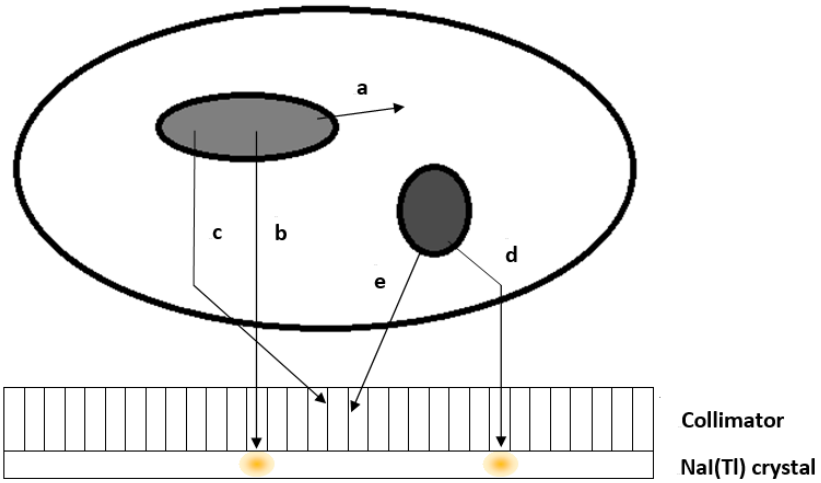

Figure 2.3.2: Different possible paths of γ-photons from a radioactive area (grey ellipses) to the collimator. Scintillation (small yellow ellipses) only occurs when the photon reaches the NaI crystal. a) Photon energy is absorbed by a dense tissue. b) Photon reaches the scintillator since its direction is parallel to the collimator. c) A Compton scattering event deflects the path of a photon aligned with the collimator, so the photon can not meet the scintillator. d) A not-aligned photon is scattered and it can interact with the crystal because its new direction is parallel to the collimator. e) The collimator absorbs a not-aligned photon.

in table 2.3.1. Pinhole and converging collimators magnify the image, whilst diverging collimators scale it down.

Increased parameter	Resolution	Sensitivity
Number of holes	No change	Increases
Hole diameter	Worsens	Increases
Hole length	Improves	Decreases
Septal thickness	No changes	Decreases
Source-to-collimator distance	Worsens	No change

Table 2.3.1: Factors affecting the performance of a parallel-hole collimator. [47]

The parallel-hole collimators can also be classified according to their sensitivity and resolution: collimators with narrow holes are called high resolution collimators

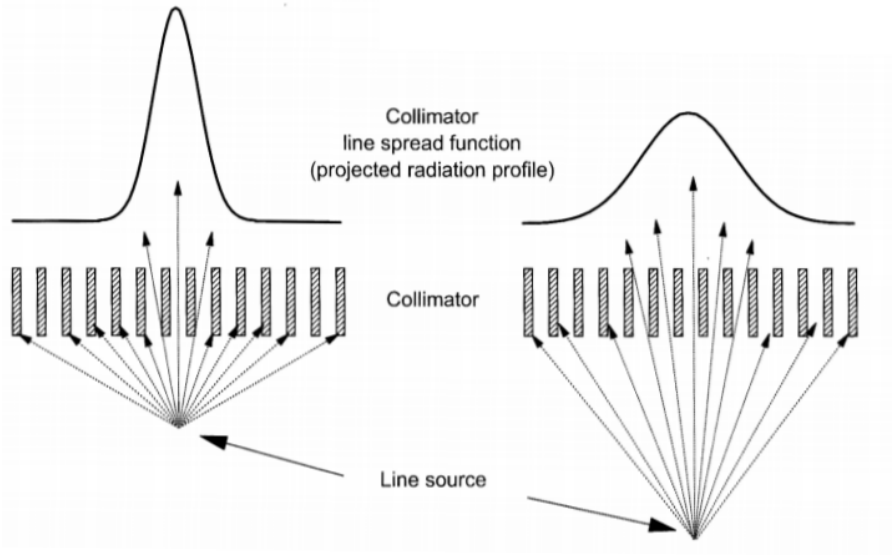

Figure 2.3.3: Line spread function (LSF) of a parallel-hole collimator as a function of source-to-collimator distance. The full width at half maximum (FWHM) of the LSF increases linearly with distance from the source to the collimator [9].

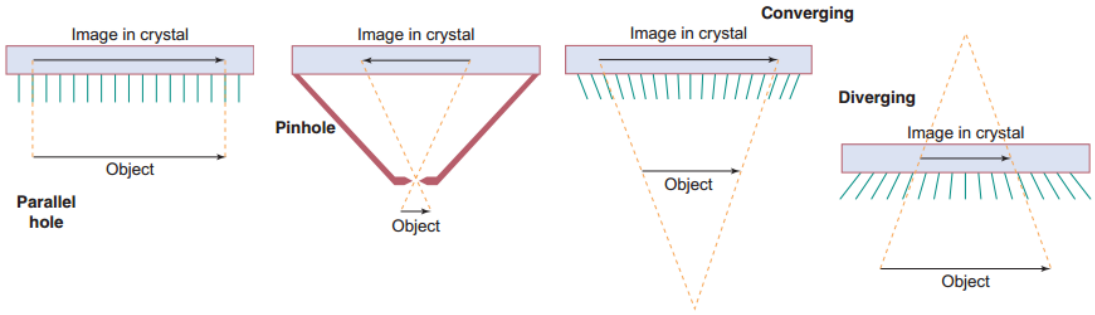

Figure 2.3.4: Types of collimator with different fields of view [10].

and ones with holes of larger size high-sensitivity collimators. Some examples are low-energy high-resolution (LEHR), low-energy general purpose (LEGP), medium-energy general purpose (MEGP), high-energy general purpose (HEGP) and low-energy all-purpose (LEAP) collimators. The choice of a collimator depends on the requests of the diagnostic test to be performed.

2.3.2 Scintillation crystal and photomultiplier tubes

Selecting the gamma rays, the collimator forms a projected image of the gamma distribution on the surface of the scintillation crystal, made of sodium iodide (NaI) doped with thallium (Tl). When the gamma rays interact with the crystal, thousands of photons with wavelength of visible light are emitted, as a consequence of the photoelectric effect. Scintillator is usually supported by a glass window, a plate which prevents deterioration due to humidity and provides mechanical support to the salt crystal.

The scintillation events produce light pulses, whose yield is proportional to the energy absorbed by the scintillator from the incident photon. The visible light photons are then optically guided through an array of photomultiplier tubes (PMTs) system. A PMT consists of a glass tube in which high vacuum is created. Figure 2.3.5 shows that the first PMT's portion met by photons in the visible light spectrum is the photocathode, a metal plate which converts the photons in a photoelectron flow. A series of plates, called dynodes, with an increasing potential, attracts electrons and accelerates them, leading to the production of a growing number of electrons (called secondary electrons). At the end of this process, all the electrons reach the anode, which presents the most positive potential. The multiplication of the electrons allows to amplify the initial information given by the photons, obtaining an electric signal which is sufficiently large to be used by conventional electronic circuits.

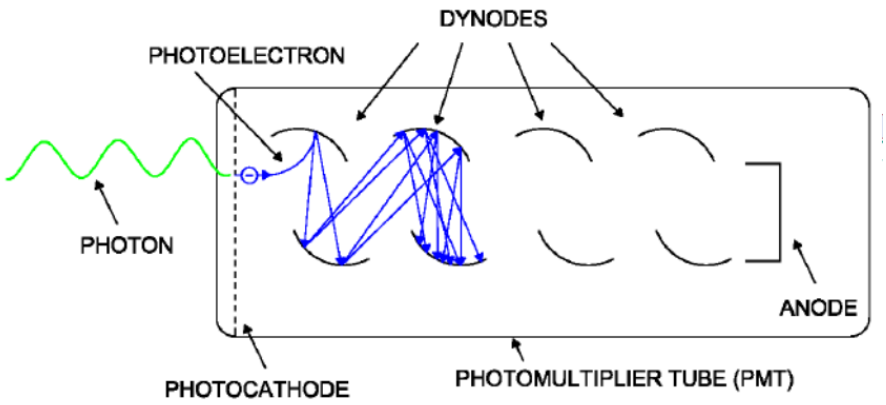

Figure 2.3.5: A photomultiplier tube scheme with secondary electron emissions [4].

2.3.3 Position encoding and pulse height analyzer

In order to produce an image, the position where detected photons came from must be identified. This is determined using the pulses that occur at the anodes of the PMT array. The output of the PMTs is mapped by a network of electric resistors, weighted according to the spatial position of the PMTs in the x-axis and y-axis of the coordinate system of the array. There are four position signals, labeled X^+, X^-, Y^+ and Y^-, and one energy signal Z that indicates the energy of the incident photon or pulse height. This helps to identify the position of an event by applying a simple formula for each coordinate, based on the relative amount of current received by each resistor. The position signal has to be normalized by dividing it by the energy signal (equations 2.3.1 and 2.3.2).

$$X = \frac{X^+ - X^-}{Z} \tag{2.3.1}$$

$$Y = \frac{Y^+ - Y^-}{Z} \tag{2.3.2}$$

The next step is the pulse height analyzer (PHA) that checks the amplitude of the pulses, i.e. the signal Z, which is proportional to the gamma ray's energy. The amplitude of this output signal would always be the same if γ-photons always were absorbed with their total emission energy. This does not happen because some photons undergo Compton scattering along their path and lose part of their energy. Since scattered-photons change their direction, it is impossible to locate where they come from. In order to have a final image with a good spatial resolution, all the registered events which do not correspond to the absorption by photoelectric effect of gamma photons with the total emission energy are not counted. A typical energy spectrum measured using a technetium-99m source is shown in figure 2.3.6.
An energy discrimination, performed by PHA, is important for imaging purposes because it provides a mean to reject the gamma-rays which have lost their positional information. This is accomplished by defining an energy window which includes the photopeak energy in the pulse height spectrum. For example γ-photons emitted by technetium-99m present a typical energy of 140 keV. If the signal Z amplitude falls within the energy window, the event is accepted. Usually the lower and upper-level thresholds of this window are defined as a percentage of the photopeak energy in the pulse height spectrum. Furthermore, more than just one window can be used, if the radioisotope is characterized by more than one gamma-ray emission.
In an ideal situation, the theoretical energy spectrum reaching the crystal should be a line spectrum with the energy of the photopeak corresponding to γ-photons emitted by the radioactive source. Actually the width of the photopeak is broader and wider (figure 2.3.6) mainly due to statistical variations:

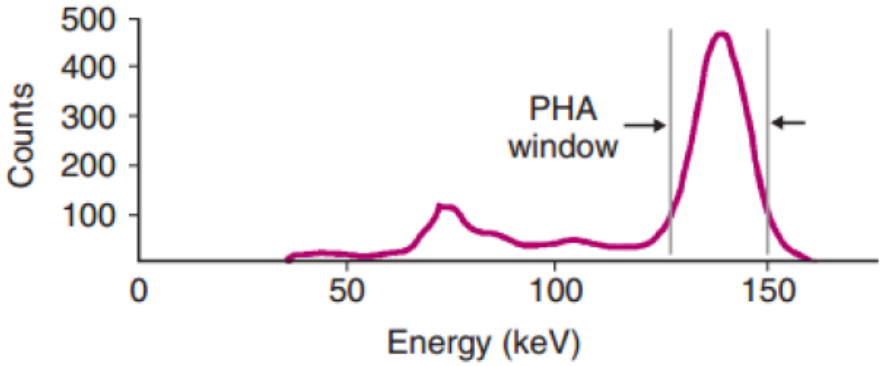

Figure 2.3.6: Energy spectrum from a gamma camera measured using a point source of ^{99m}Tc in air. A typical energy window (±7.5% of the ^{99m}Tc photopeak energy, i.e. 140 keV) is shown superimposed on the spectrum [12].

- In the scintillator γ-photons with the same energy do not produce light photons with the same features.
- The light photons produced do not generate the same photoelectrons in the PMT photocathode.
- The number of secondary electrons produced in each dynode is different for each incident photon.

2.4 Single Photon Emission Computed Tomography (SPECT)

2.4.1 Acquisition

SPECT data acquisition aims to collect a sufficient set of 2D projection data provided by the gamma camera in order to reconstruct a 3D tomographic image of the tracer activity distribution. In order to achieve this goal, the patient needs to be positioned in the centre of the camera's FOV, so that the system can rotate around the patient, acquiring 2D images from multiple angles.
As regards SPECT acquisition mode, there are two different procedures. In *step-and-shoot acquisition mode* the gantry rotates with a certain angular step, and only in each step photons are collected. The disadvantage of this process is that it takes time to move the detector between positions, thus resulting in dead time with no recorded counts. An alternative method is the *continuous acquisition mode*: data are acquired as the detectors continuously rotate around the patient with a

constant speed. In this way dead time is deleted and more counts are recorded, but spatial resolution decreases because of the detector motion during the acquisition. For most SPECT procedures projection data are acquired over a full 360° arc. The exception usually is SPECT-MPI which involves a 180° acquisition: since projection views which are opposite to the heart detect significantly less myocardial activity due to the attenuation through the patient's thorax, a 180° acquisition can improve resolution and contrast, but it causes some distortion problems [20].
The standard output matrix size of a SPECT system is 64x64 or 128x18 pixels, resulting in pixel sizes ranging from 3 to 8 mm.
A SPECT detection system can have different configurations, regarding the number of gamma cameras that are incorporated: one, two, three or four detector heads or multiple small-FOV scintillation detectors (figure 2.4.1). In the case of a two camera system, cameras may be positioned orthogonal or opposite to each other. The increased number of detector heads provides a greater system sensitivity, because the number of detected γ-photons increases; as a result, the acquisition time is reduced.

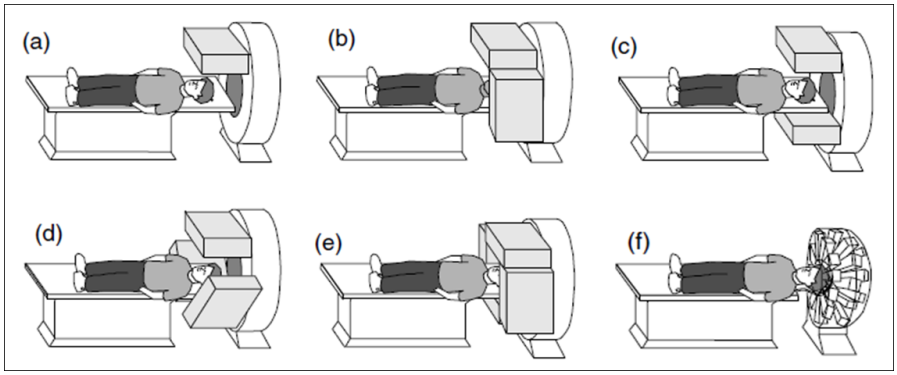

Figure 2.4.1: SPECT system configurations. Schematics are shown for: a) single head, b) orthogonal heads, c) opposed heads, d) three heads, e) four heads and f) multiple small-FOV detectors [60].

2.4.2 Radionuclides in SPECT

Radioactive compounds participate in an organism's physiological processes in the same way as non radioactive materials. Consequently, radionuclides can be used to track the distribution of specific substances in the body, thanks to their emission of gamma-ray. The combination of a biological, non-radioactive substance with a radioactive material is called radiopharmaceutical or radiotracer and it can be designed to play the role of marker for a variety of compounds in different metabolic pathways.

The radionuclides suitable for SPECT imaging should have the following properties:

- The radionuclide has to be a γ-photons emitter and to decay by electron capture or isomeric transition (see the definitions in 2.2.2).
- The half-life of the radioisotope has to be long enough to examine metabolic processes but also short enough to minimize the radiation dose.
- The gamma emitter needs to have enough energy to pass through the patient's tissues and reach the detector. However, the γ-ray energy should be low enough so that it can be absorbed easily by the detector: the upper limit of γ-photons energy is about 300 keV and it decreases to 200 keV with the low-energy collimators.
- The chemistry of the radioisotope should allow it to label a range of biologically active substances so that it concentrates in the tissues of the organ of interest.
- The radionuclide should be easily available and have a reasonable cost.

The most important radionuclide in SPECT is technetium-99m, which presents all the characteristics listed above. This nuclear isomer of technetium can bind chemically to many biological active molecules making it suitable for many medical exams. It is produced on site using a molybdenum-99 generator. The table 2.4.1 shows the properties of different radionuclides used in SPECT imaging.

Radionuclide	**Half-life (h)**	**Gamma energy (keV)**	**Mode of Generation**	**Decay mode**
^{99m}Tc	6.02	140	^{99}Mo generator	Isomeric transition
^{123}I	13	159	Cyclotron	Electron Capture
^{111}In	67.2	172, 247	Cyclotron	Electron Capture
^{201}Tl	73	135, 167	Cyclotron	Electron Capture
^{67}Ga	78.1	95, 185, 300	Cyclotron	Electron Capture

Table 2.4.1: Properties of commonly used SPECT radioisotopes [8].

2.4.3 Reconstruction

A gamma camera is only able to capture a planar image, which consists of a 2D projection of the 3D radionuclide emission distribution. Therefore, this representation lacks depth information and different 3D structures are overlapped and indistinguishable. Indeed, photons emitted at different depths, but along the same direction, are detected by the same detector's portion, as shown in figure 2.4.2. Otherwise stated, an infinite number of tracer distribution can yield the same pro-

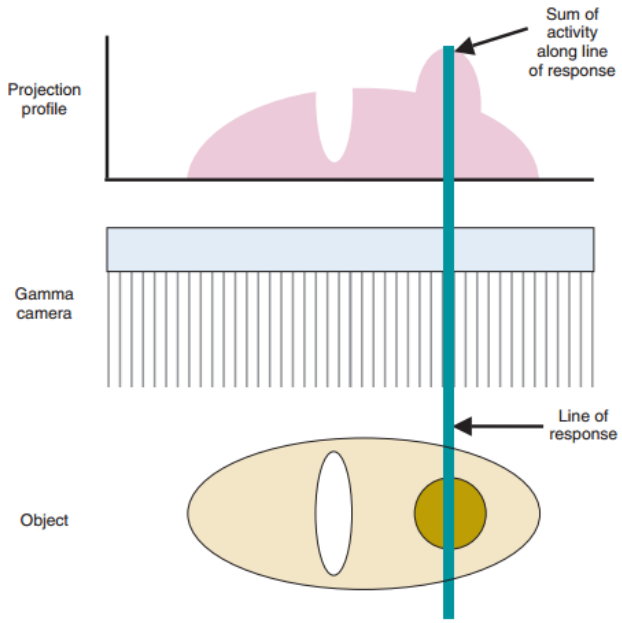

Figure 2.4.2: Projection profile of an acquisition by an idealized gamma camera [12].

jection. This problem is solved by using Emission Computed Tomography (ECT) technique, which allows to reconstruct a 3D spatial distribution by acquiring 2D projections at different angles of view around the object of study. This process is represented by figure 2.4.3: for drawing simplicity, here the rotation of the gamma camera provides a set of 1D projection profiles for a 2D radioactive object. The number of possible solutions (related to the distribution of the radiotracer) reduces as the number of angular positions of the detector increases. Hence ECT provides important diagnostic information since it is capable of providing more accurate quantification of activity at specific locations within the body. It is useful to introduce a new coordinate system (r, s) which is jointed to the gamma camera detector. This new system is rotated by an angle ϕ from the unrotated coordinate system (x, y) but their origins are coincident. The (r, s) axes are, respectively, perpendicular and parallel to the projection array and the new coordinates can be calculated with the equations 2.4.1 and 2.4.2.

$$r = x \cdot \cos\phi + y \cdot \sin\phi \tag{2.4.1}$$

$$s = y \cdot \cos\phi - x \cdot \sin\phi \tag{2.4.2}$$

In the figure 2.4.4 $p(r, \phi)$ represents the number of γ-photons detected at a location r along the detector, with the detector head in an angular position ϕ. At the

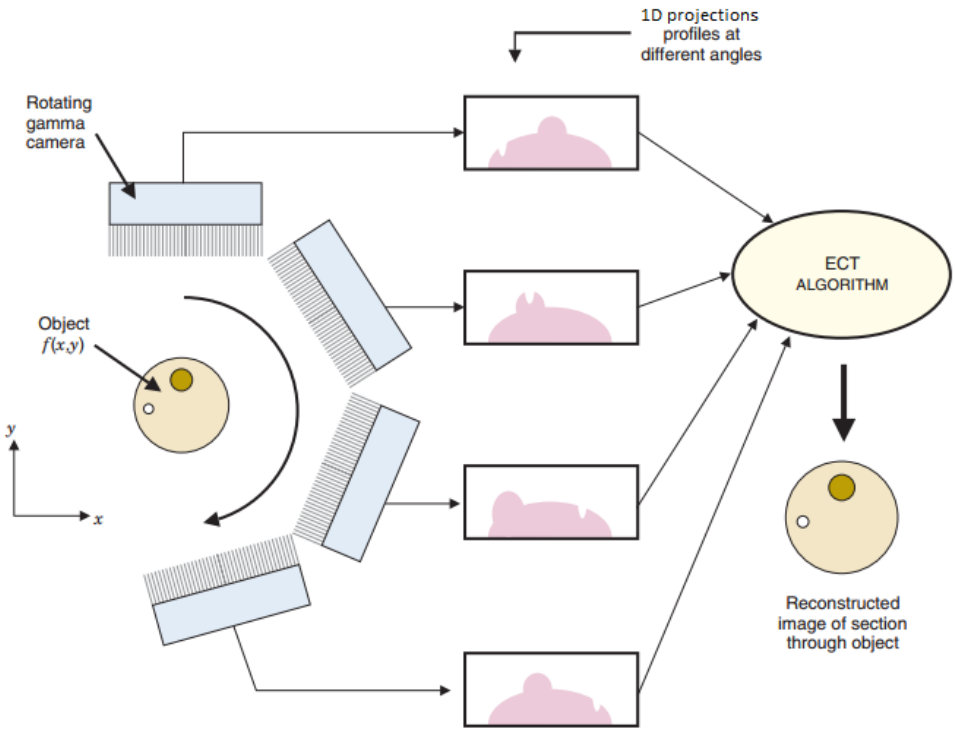

Figure 2.4.3: Different acquisitions around the object provides a set of 1D projection profiles for a 2D object. Then they are used to calculate an estimation of the 2D distribution in the object [12].

same time, $f(x, y)$ corresponds to the estimated number of photons emitted in the position (x, y). The matrix $p(r, \phi)$ data are commonly displayed in the form of a single plot called sinogram: its horiziontal axis indicates the projection bin and its vertical axis refers to the projection angle. Figure 2.4.5 shows a sinogram for a single point-source. Each row of the sinogram matrix represents an intensity display across a single projection from a specific angular position. Moving from the top to the bottom, the graph refers to successive projection angles. The resulting plot has a sine wavelike shape. Each wave corresponds to a (x, y) location whose distance from the centre of rotation determines the wave amplitude and whose angular location defines the wave phase. This representation allows for easier data processing, image reconstruction and correction techniques. These measured projection data are used by reconstruction algorithms to generate a tomographic image. The distribution of the detected counts (g) can be defined by the equation

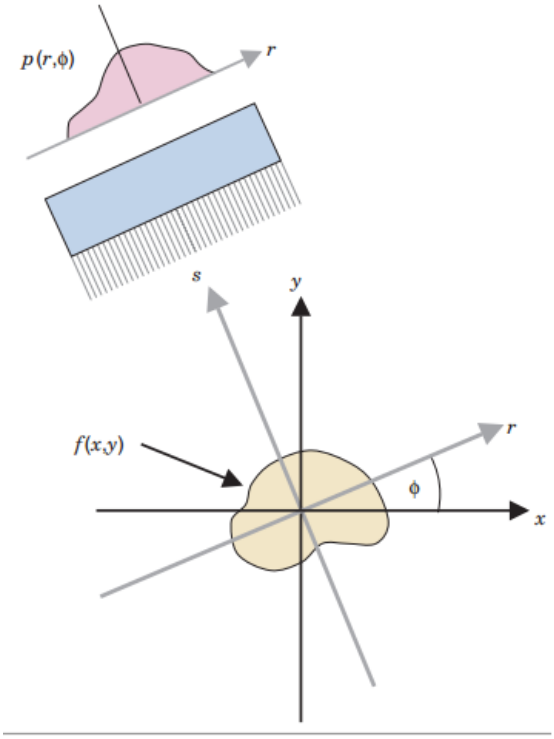

Figure 2.4.4: Geometric considerations for a tomographic acquisition. The (r, s) coordinate system is rotated by projection angle ϕ with respect to the (x, y) coordinate system [12].

2.4.3, in which f represents the distribution of the emitted counts in the FOV of the camera and A means the projection operator.

$$g = A \cdot f \tag{2.4.3}$$

In the reconstruction process, the system of equations described in the equation 2.4.3 must be solved to find f, given the measured data g. Two main approaches can be used to solve this system of equations, *analytical* and *iterative* reconstruction algorithms. Analytical methods typically consider the reconstruction process as an inverse problem and they try to find the exact mathematical solution to estimate the radionuclide distribution f. Thus, solutions can be computed very quickly and efficiently. However, the resulting images may contain some artefacts because attenuation and noise are not suitably accounted for. On the other hand, iterative reconstruction methods rely on the selection of the best estimation of the real image: an algorithm repetitively attempts to obtain this solution through successive approximations. Usually this is accomplished by statistical methods and

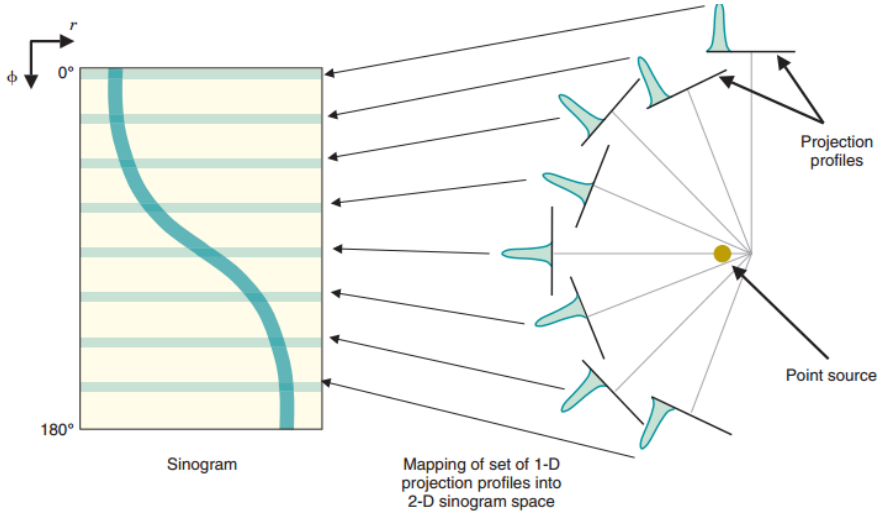

Figure 2.4.5: Wavelike pattern of a sinogram for a single point-source. Each row of the plot corresponds to a projection profile acquired with a precise angular position [12].

probabilistic models. The advantage of iterative algorithms lies in the possibility of modelling different degrading effects but they require more computational costs.

2.5 SPECT Myocardial Perfusion Imaging

SPECT myocardial perfusion imaging (MPI) is a non-invasive nuclear procedure which has emerged not only as a diagnostic technique but also as a robust prognostic tool: it is able to provide data about myocardial perfusion, ventricular function and viability, performing a single test [44]. MPI is the stress imaging procedure that is most widely used in the management of patients with CAD (see the definition in 2.1.4) [48]. The sensitivity of stress SPECT MPI for detecting angiographically-defined CAD is consistently above 70%, but in the better-designed studies, it can reach the range of 85-90% [1].
In this type of imaging, after the images are acquired, they are reoriented into the LV frame of reference, instead of the body's referential. Three axis are defined, which refer to three different views perpendicular to each other: the short axis (SA), the vertical long axis (VLA), and the horizontal long axis (HLA) (figure 2.5.1). The long axis of the heart is considered to be the axis that aligns the base of the heart and the apex, whilst the short axis is the plane perpendicular to the long axis. SA images give a cross sectional view of the ventricles or of the atria, HLA images cut the heart moving from the posterior wall to the anterior wall, and VLA images cut the heart from the septal wall to the lateral wall [11].

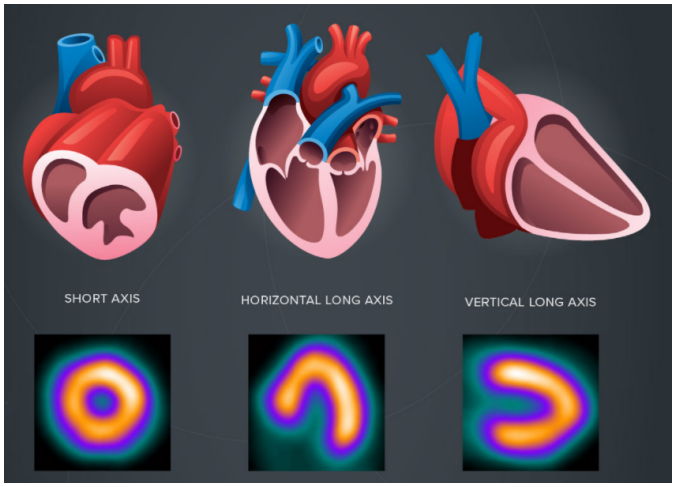

Figure 2.5.1: Standard views for a SPECT MPI study. SA, HLA and VLA are the three axis of the LV frame of reference. Image adapted [54].

In an SPECT MPI study two sets of images are acquired, one after a stress test and another in a rest state [22]. The comparison between stress and rest images allows for the coronary flow assessment: stress images with a perfusion defect in a region which appears normal on rest images (i.e. a reversible defect) suggest a myocardial ischemia (figure 2.5.2 A); a perfusion defect which is present both on stress images and on rest images (i.e. a fixed defect) is suggestive of either an attenuation artifact or an area of myocardial infarction (figure 2.5.2 B) [13].

2.5.1 Stress modalities for MPI

Stress tests are needed to investigate the coronary flow reserve, which is defined as the maximum increase in blood flow that coronary arteries can supply to satisfy metabolic demand [7]. SPECT MPI allows to detect the cardiac sites where this parameter is altered at rest and after a stress test. Indeed, if some coronary flow alterations are present, the produced images will show an heterogeneous radiotracer distribution [29]. Significant coronary lesions appear as areas of decreased myocardial tracer uptake [25]. Different stress modalities can be applied in nuclear cardiology:

- Physical exercise: this is the most physiological test for detecting a myocardial ischemia. The patient is asked to perform a physical effort on a treadmill or a stationary bike. Through biochemical mechanisms exercise produces coronary vasodilation to face the increased oxygen demand. When patients are able to exercise adequately, this physical test is preferable over all the

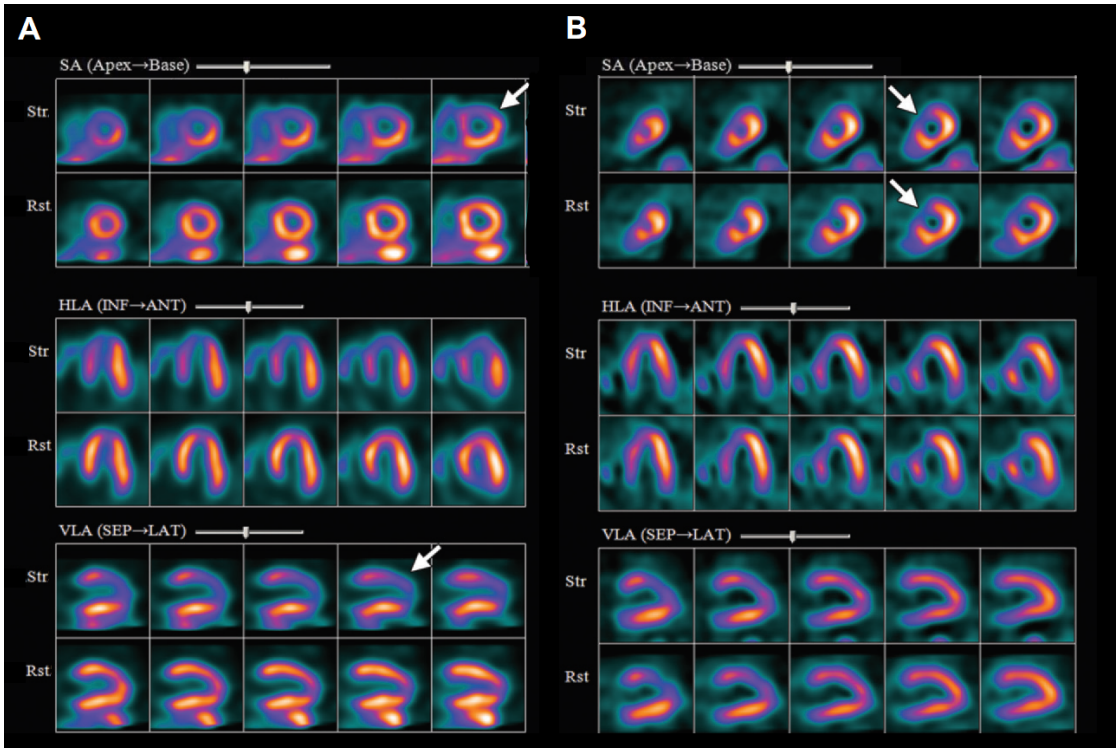

Figure 2.5.2: Examples of cardiac perfusion defect in a SPECT MPI study. A) A large reversible cardiac perfusion defect is located on the anterior, septal, and apical walls (arrows). B) A large fixed anteroseptal perfusion defect is indicated by the arrows. This finding may indicate a myocardial infarction. Str: stress. Rst: rest. SA: short axis. HLA (INF → ANT): horizontal long axis (inferior to anterior). VLA (SEP → LAT): vertical long axis (septum to lateral wall). Image adapted [13].

other stress modalities. Indeed, it provides more information such as total exercise duration and development of symptoms (e.g. chest pain) [24].

- Pharmacologic stimulation: this modality is the alternative to physical exercise. Different pharmacologic stress agents are available and they simulate the exercise-induced response in different ways. The vasodilators, such as adenosine and dipyridamole, induce vasodilation, while dobutamine induces an increase in heart rate and contractility [44]. When adenosine is injected intravenously, it causes vasodilatation by direct activation of vascular A2 receptors. Dipyridamole also induces vasodilation with an increase of extracellular adenosine, but this is done indirectly: dipyridamole inhibits an enzyme named adenosine deaminase, which degrades endogenously produced adenosine, and stops the reuptake of adenosine by cells [51]. On the contrary,

dobutamine is not a vasodilator but a beta adrenergic agonist drug which promotes coronary hyperaemia through mechanisms similar to exercise [18]. Vasodilators are reserved for patients unable to exercise or with specific conditions, such as left bundle branch block, cardiac pacemakers and alterations in resting ECG. For these subjects an exercise-induced heart rate increase could produce alterations in ECG and/or in myocardial perfusion which may be misinterpreted as ischemia [34]. In most countries, vasodilators are preferred to dobutamine when they are available. Dobutamine stress modality is recommended for patients with reactive airway disease (severe chronic obstructive pulmonary disease or asthma), who are unable to exercise and for whom vasodilators are contraindicated, as adenosine and dipyridamole may induce bronchospasm [24].

2.5.2 Radiopharmaceuticals and imaging protocols

In SPECT MPI the three widely available radiopharmaceuticals used are thallous chloride (^{201}TlCl), technetium-99m (^{99m}Tc)-sestamibi and ^{99m}Tc-tetrofosmin. A considerably higher radiation dose is associated to imaging perfomed with thallium-201 because it presents a much longer physical half-life (73 h) than technetium-99m (6 h), exposing the patient to radiations for a longer time after the examination [14]. Thallium-201 may be preferred when viability assessment is the purpose of the study or if extracardiac uptake of technetium-99m altered cardiac images in a previous study. Nevertheless, a technetium-99m based radiotracer should be chosen for most patients [24]. Therefore, the protocols described below are performed with technetium-99m based radiopharmaceuticals.

When sestamibi and tetrofosmin are used, separate injections are performed to assess stress and resting perfusion. With 6 h physical half-life of technetium-99m, stress and rest injections should ideally be performed on separate days, in order to enable the decay of the activity from the first injection activity (otherwise a shine through of counts from the first to the second injection would occur). If both injections are performed in a single day, the second injection should provide at least 3-4 times as many counts as the the first injection to minimize the shine through issue. In this case, it is therefore necessary to administer at least 3 times greater activity for the second injection [24]. A two day protocol enables the radiation dose to be minimized, since it requires no more radioactivity for the second injection than for the first one. Using the same administered activity each day, two day studies also facilitate comparison between stress and rest images. Single day protocol can be preferred in some cases: it entails an advantage for the patient, as they do not need to return to the nuclear laboratory on the second day if the first images display some abnormalities.

In a technetium-99m imaging protocol, stress imaging is usually performed first. If the stress images are evaluated by a physician as completely normal (i.e. normal perfusion, normal function, normal LV size, no regional wall motion abnormalities and no increased RV tracer uptake), no rest imaging is performed. Stress-only imaging was found to reduce radiation dose by 64% [37]. Therefore, stress-first imaging should be preferred when there is a reasonable probability that the results do not present abnormalities. In a single day protocol, resting study may be performed first if the patient presents a known previous infarction. Indeed, rest images could be useful to customize the next component of the study, choosing between stress imaging or viability assessment [24].

The amount of technetium-99m administered should reflect patient weight and habitus. Generally larger patients need more activity than smaller patients to achieve good image quality. For example, thin patients without excessive breast tissue should receive activities at the low end of the recommended range for a given protocol, whilst study with obese patients benefit from the administration of the highest possible amount of activity. If weight based dosing is used within a laboratory, a significant correlation between patient weight and technetium activity should be observed [24].

2.5.3 Gated SPECT MPI

SPECT MPI can be guided by the acquisition of an ECG, which enables to relate the collected images to a precise phase of the cardiac cycle. A number of time bins or frames is defined to divide the interval between two R-waves of the ECG; 8 or 16 frames are usually acquired [41]. When the acquisition is completed, the images referred to the same time bin are collected in the same dataset, which represents the radiotracer distribution during that time frame. This process enables the physician to analyse the heart during contraction and expansion from diastole to systole. Gated studies provide important data, such as post-stress and rest LVEF, LVEDV (cf. the definitions in 2.1.2), wall motion, myocardial thickening, shortening and contractility [44]. In patients without a regular heart rhythm (e.g. patients with atrial fibrillation), gated SPECT volumes and ejection fraction may not be reliable. For this reason, before starting the acquisition, it is recommended to check for a correct ECG signal. The quality control page of the gated images usually displays a beat histogram (as shown in figure 2.6.5). A widened peak or multiple peaks would indicate variable heart rate, frequent arrhythmias or improper gating, so that quantitative results about the ventricular function may be inaccurate [24]. Nevertheless, using a regular ECG signal, gated SPECT MPI has shown an high prognostic value and sensitivity for critical stenosis [23].

2.6 D-SPECT

2.6.1 Solid-state CZT technology

In a traditional gamma camera, a γ-photon hits a sodium iodide (NaI) scintillation crystal, which transforms the photon energy into a flash of light; a PMT then transforms the light photon into an electric charge, completing a two-step process. With a solid-state detector, a γ-ray strikes a different type of crystal, such as cadmium zinc telluride (CZT), which is a semiconductor that converts the photon directly to a digital electronic signal, a one-step process.
With NaI detector, to pinpoint the origin of each event, a complex algorithm compares the relative signal amplitude from all the PMTs. Because of this analog position sensing, these systems present poor energy resolution and contrast compared to solid-state detectors. Already in 1998 the solid-state systems were characterized by greater portability, with a weight of only 135 kg, whilst traditional gamma camera system weighed 1350 to 2250 kg [27].
In 2004 Wagenaar developed pixelated CZT detectors units, which allows it to be used for medical imaging applications [56]. While other solid-state detector materials, such as germanium, requires liquid nitrogen cooling to ensure proper SNR, a CZT detector can operate in direct conversion mode at room temperature, allowing for more compact and flexible designs [15].

2.6.2 D-SPECT system

A conventional SPECT system is able to collect only 0.02% of the photons emitted during a cardiac imaging examination, because almost all photons are absorbed by the collimator [16]. To improve this low sensitivity, new cardiac-dedicated SPECT system have been developed, such as the D-SPECT [17].
Introduced for the first time at the 2005 RSNA meeting in Chicago by Spectrum Dynamics Medical, D-SPECT system introduces a novel photon-collection and scanning geometry, providing a good sensitivity combined with a fast acquisition time.
The D-SPECT camera consists of 9 pixelated CZT detector columns, arranged in a curved configuration that encloses the left side of the patient's chest (figure 2.6.1). Figure 2.6.2 shows that each detector column is composed by 4 detector modules, which are 16x16 CZT elements with a square geometry (2.46 x 2.46 mm) and 5 mm of thickness [16].
The camera is equipped with tungsten parallel-hole collimators that are shorter (21.7 mm) and have larger square holes (2.26 mm) compared to standard lead parallel-hole LEHR collimators, which are 45 mm long and whose square holes measure 1.6 mm. Furthermore, the stopping power of tungsten is greater than

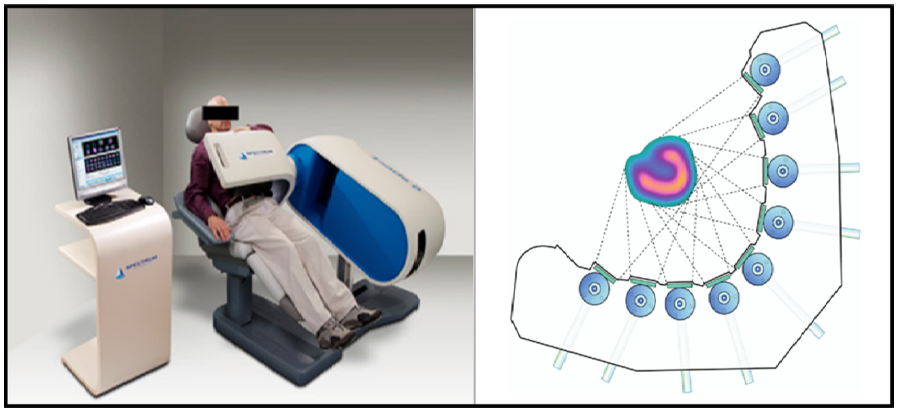

Figure 2.6.1: D-SPECT system. On the left, positioning of the patient and the camera are shown. On the right, figure shows the configuration of the 9 detectors around the heart region [16].

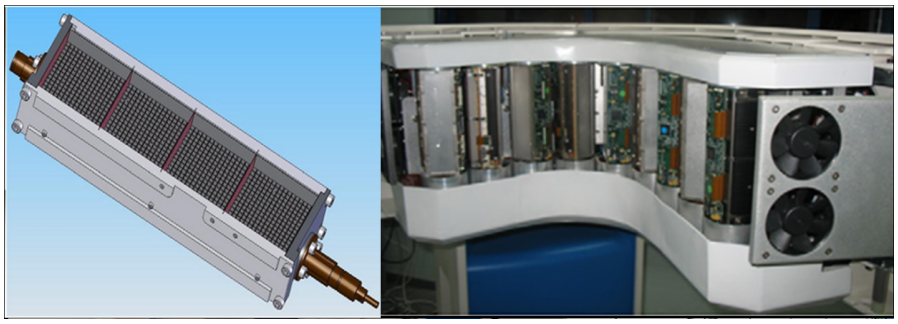

Figure 2.6.2: D-SPECT detection system. On the left, one detector formed by 4 square CZT modules is shown. On the right, figure shows the whole camera and its 9 detectors positioned in a curved configuration [16].

that of lead [16], allowing for the use of thinner collimator septa, which provides an increased useful detector area.

The D-SPECT is equipped with an effective acquisition system: the 9 detector columns swivel up to 110° around their long axis and each detector is able to rotate independently with a programmable angular orientation [2].

Before starting the acquisition, the patient is placed in a semi-upright position with the left arm above the detector, or in a supine position with the left arm up (figure 2.6.3). In both cases, the gantry is positioned parallel to the patient's chest, as close as possible to it (the reason is explained in 2.3.1). During the acquisition, physiological markers as the R wave of the ECG are recorded if a gated imaging is required. A pre-scan of 30-60 s is performed prior to the acquisition to verify that the patient has been positioned correctly: this scan covers the whole FOV

(sweep mode) and a preliminary image of the activity distribution is obtained to check the subject's heart is in the FOV; if the heart is in the wrong position, the patient is re-positioned. After obtaining a pre-scan with a good patient placement, a region of interest (ROI) that includes the heart is defined by the operator. This ROI-positioning on the left ventricle (LV) allows the D-SPECT system to focus the sampling on the heart of the patient, providing a so-called region-centric acquisition. As shown in figure 2.6.4, during the actual acquisition, each detector will spend more time collecting data from this specific ROI compared to the sampling of the other regions in the FOV, maximizing the number of acquired counts from this region [17]. Data are still collected from outside the pre-defined ROI in order to avoid truncation effects.

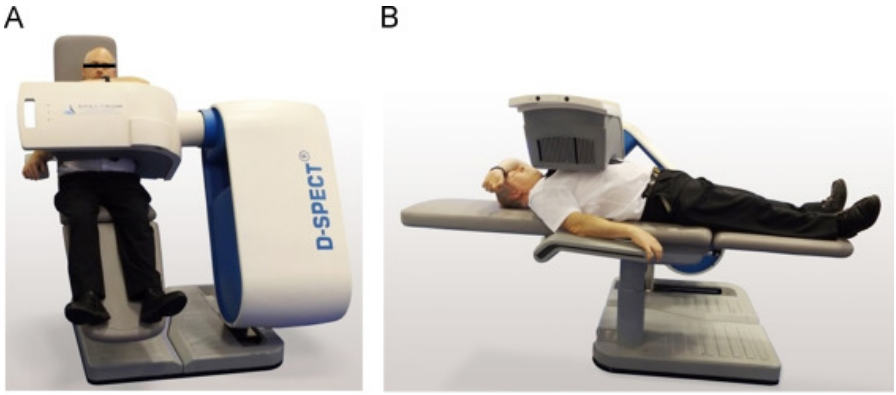

Figure 2.6.3: Two possible configuration during a D-SPECT examination: semi-upright (A) or supine (B) position [6].

When the acquisition is finished, sinogram (see the definition in 2.4.3) is displayed to check the image quality. Furthermore, the counts from all detectors in each position are summed and the total is displayed. Two sweeps of the detectors are normally obtained with detectors slightly rotated to complete 180° acquisition, creating a panogram and enabling motion detection (figure 2.6.5).

A built-in inclinometer indicates the angle of the chair and of the detector head during each scan, allowing replication of images in exactly the same position. This is needed to avoid mis-alignment between stress and rest datasets.

To conclude, the D-SPECT camera shows 8 to 10 times improvement in sensitivity compared to conventional systems, due to the combined wide-angle collimator and fast region-centric acquisition, as well as improved reconstructed resolution and superior energy resolution [15]. Therefore, D-SPECT allows to obtain good quality images with shorter scanning times or reduced radiation exposure by lowering the dose of the radiotracer.

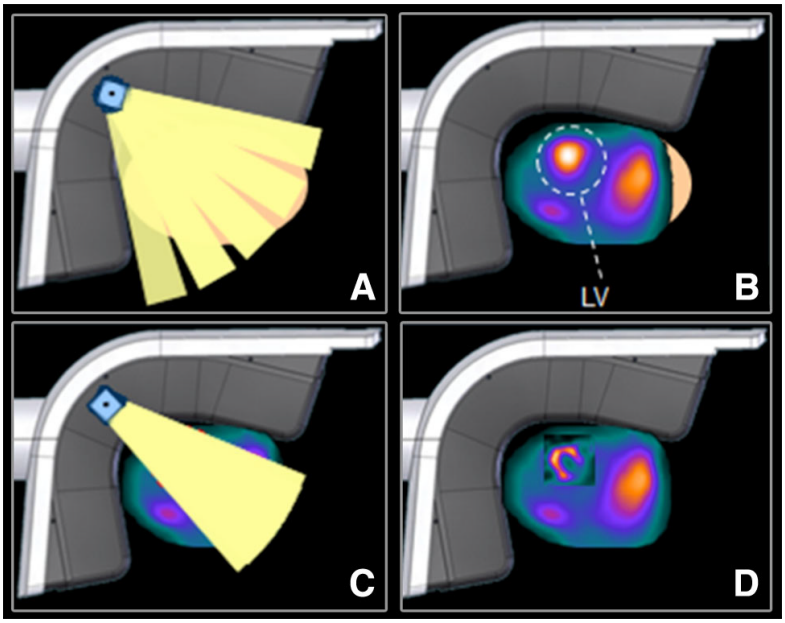

Figure 2.6.4: Pre-scan and focused scan acquisition. A 30 s pre-scan of the whole FOV is performed (A) to determine a region of interest that includes the heart (B). A focused scan is performed, centered on the heart (C) with illustration of reconstructed data (D) [2].

2.6.3 Pitfalls and artifacts

Many factors can contribute to degrade SPECT image quality, resulting in reconstructed images which do not represent the real radiotracer distribution. The most frequent causes of imaging artifacts and pitfalls of D-SPECT system are listed below (source: *"Data QC and Image Quality Guide"* of the *D-SPECT Cardiac Imaging System* by Spectrum Dynamics Medical).

- **Electrical and hardware issues**
  - **Absent detector**. In this case a disruption in the electronic signal affects one of the detector modules. This may be due to either a hardware component failure or a power supply interruption to the specific module. If this issue arises, a blacked-out area will appear in the QC scan and a jagged broken line will cut through the sinogram (figure 2.6.6 A). Myocardial perfusion datasets can suffer from this problem if the location of the absent module overlaps the heart areas.
  - **Noisy module**. If a detector module presents electronic noise, the obtained images show a lack of homogeneity. A noisy module can appear as a zone with decreased uptake during the acquisition and as an area

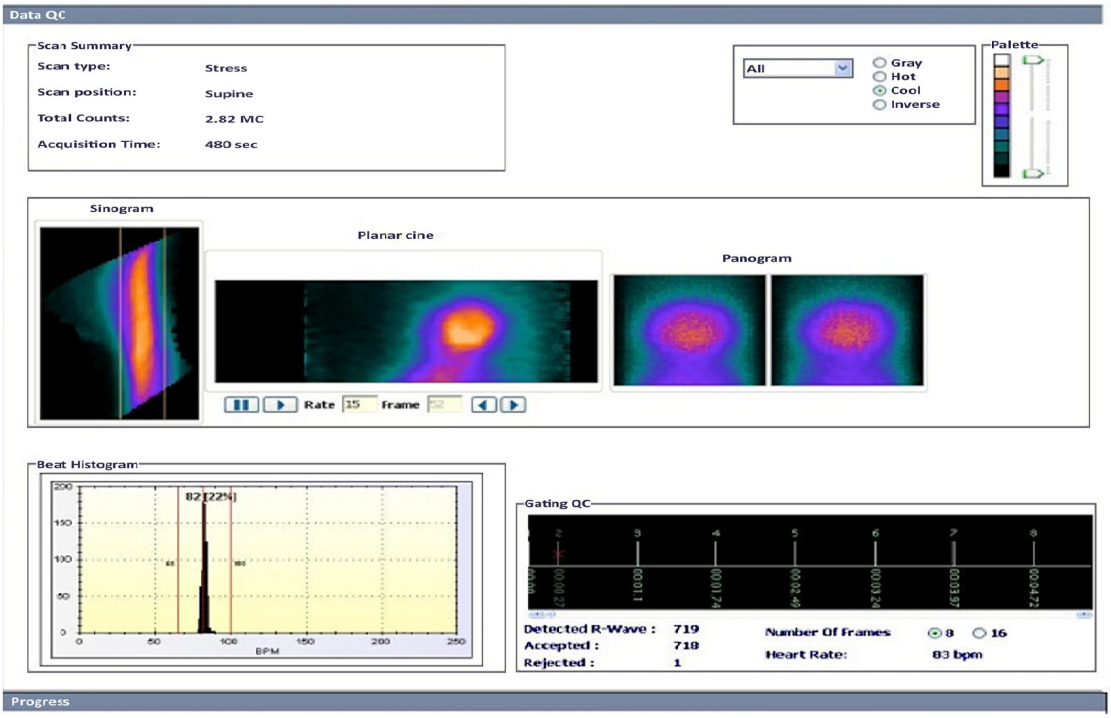

Figure 2.6.5: Post-scan QC window. At the *top* sinogram (*left*), raw cine data (*center*) and panogram sweeps (*right*) are displayed. At the *bottom* gating QC is shown with indication of accepted and rejected beats [2].

of higher activity on the QC panogram and planar cine (figure 2.6.6 B). The influence of this issue on the myocardial perfusion data depends on the position of the affected detector.

- **Patient-related artifacts**
  - **Attenuation artifact**. This is one of the most prevalent sources of artifacts on MPI and may reduce the imaging accuracy. As explained in 2.3.3, not all the γ-photons emitted by the radiopharmaceutical are collected by the detectors, even if their path is parallel to the collimator. These photons interact with the patient's tissues mostly via Compton scattering, losing part of their energy and changing their direction. Photon attenuation refers to interactions where the incident photon is completely absorbed or deflected [59]. Attenuated photons do not contribute to the image reconstruction because their initial position is incalculable after their deflection. A non-uniform image artifacts is obtained due to a decrease of the available counts [30]. In cardiac studies, D-SPECT system usually preserves image quality also in patients with an high BMI,

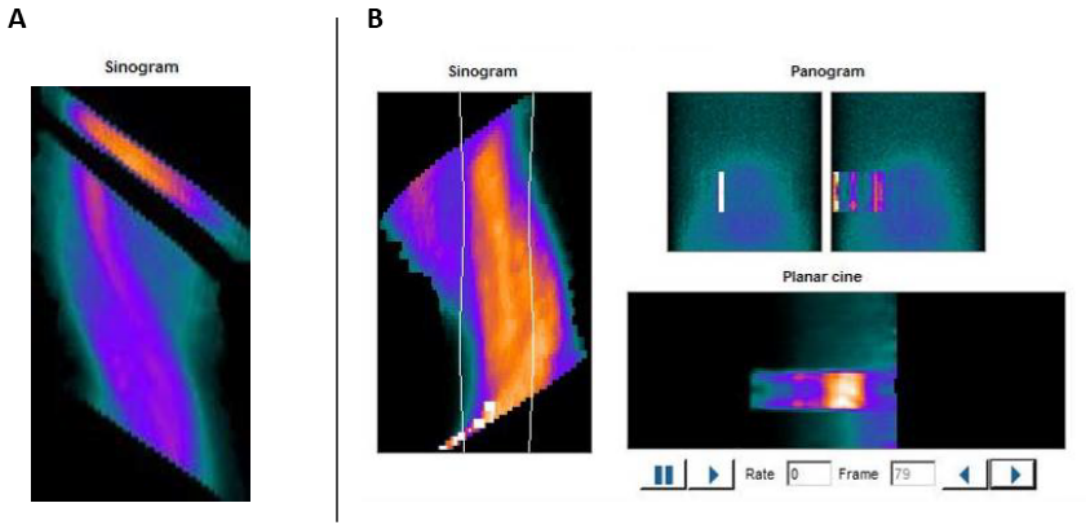

Figure 2.6.6: Electrical and hardware problems in D-SPECT system. An absent detector issue creates a jagged broken line in the sinogram (A). If a noisy module is present, an area of increased intensity can appear on the panogram and raw QC data (B) [33].

but some specific cases should be considered properly: breast attenuation may occur in women with large breasts while in obese men attenuation is mainly due to the diaphragm. Figure 2.6.7 shows that supine and upright configuration may be used in order to discern between soft tissue attenuation artifacts and actual perfusion defects [5]. For example, in case of breast attenuation artifact, it is preferable to lay the patient down in a supine position, while upright configuration is better to limit diaphragmatic attenuation.

– **Motion artifact**. One of the most recurrent sources of image degradation on SPECT MPI is related to patient motion. Motion artifacts can be caused by gross motion or coughing with motion, whilst breathing is usually not a source of this type of artifact [2]. Sinogram and panogram in data-QC highlight horizontal or vertical motion (figure 2.6.8). If a severe and frequent motion occurs, it is reccomended to repeat the scanning, ensuring the patient is in a comfortable position.

– **Extra-cardiac activity**. The radiopharmaceutical can concentrate within the patient in tissues and organs other than the heart. The activity from the areas adjacent to the heart may affect the myocardial perfusion assessment. Liver and gut uptake are the main sources of

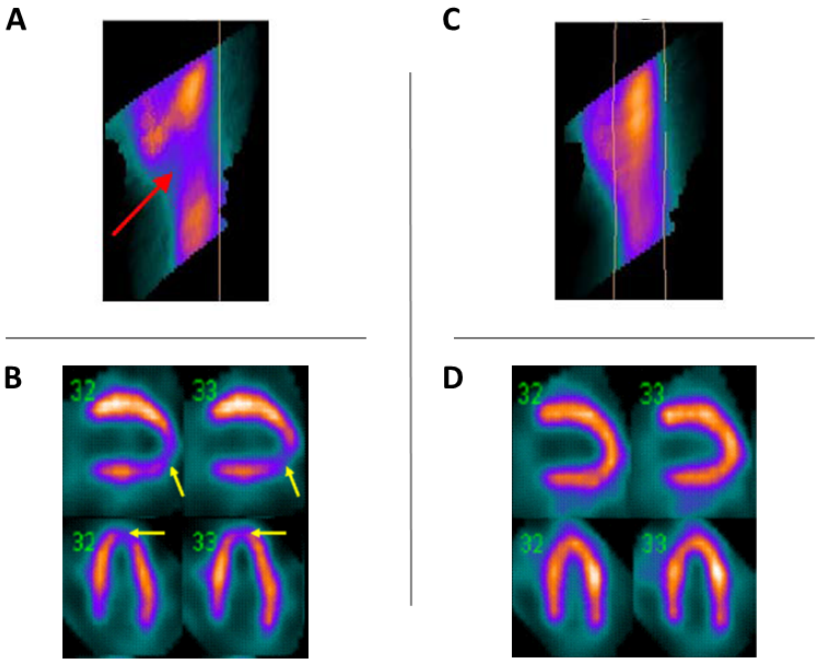

Figure 2.6.7: Example of breast attenuation artifact. A sinogram is obtained using an up-right configuration (A): the cold area in the middle of the sinogram is generated by left breast attenuation. This may cause an inferior-apical defect on the reconstructed images (B). To investigate the defect, the patient is re-scanned in a supine position and the artifact disappears from the sinogram (C) and from the reconstructed images (D) [33].

this type of artifact, producing an alteration in the activity distribution recorded in the inferior heart wall. Extra-cardiac activity can add or remove counts to the heart area, resulting in an apparent increased or decreased inferior wall uptake. Also in this case, scanning both in upright and supine position can help in carrying out a correct perfusion evaluation, recognizing possible extra-cardiac artifacts (figure 2.6.9). If there is a high uptake in the areas surrounding the heart, it may be necessary to perform the scan again after a certain amount of time; furthermore, in order to speed up the washout of gut uptake, it is suggested to make the patient drink cold water or soda water [2].

- **Operator-induced artifacts**
  - **Incorrect ROI selection**. Analyzing the images in the 3 views produced by a short pre-scan, the operator has to define a ROI centered on the LV in order to determine the correct detector scan pattern during the actual

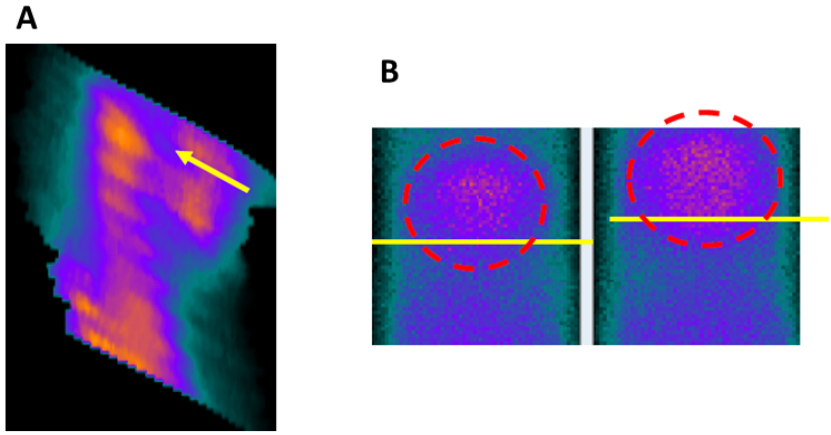

Figure 2.6.8: Example of motion artifact. Sinogram (A) and panogram (B) show patient motion during the acquisition. By looking at the panogram, a clear patient motion can be seen between the two sweeps [33].

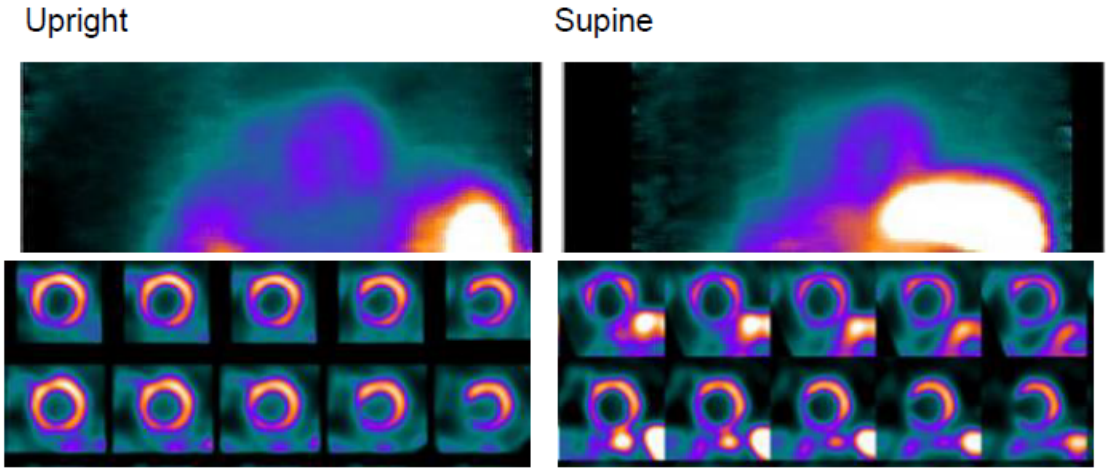

Figure 2.6.9: Example of extra-cardiac activity artifact. On the left, pre-scan front view image (*top*) and some reconstructed SA images (*bottom*) have been acquired in an upright position; on the right, the corresponding images recorded in a supine posture are shown. In this case the upright configuration demonstrates a better image quality, due to anatomic position of the spleen and the gut [33].

acquisition. In presence of high extra-cardiac activity or attenuation artifact near the LV, choosing the correct ROI location and size can become a difficult task. If the selected ROI is not on the right position

or is too narrow, a corrupted image quality and artifacts will appear in reconstructed images (figure 2.6.10).

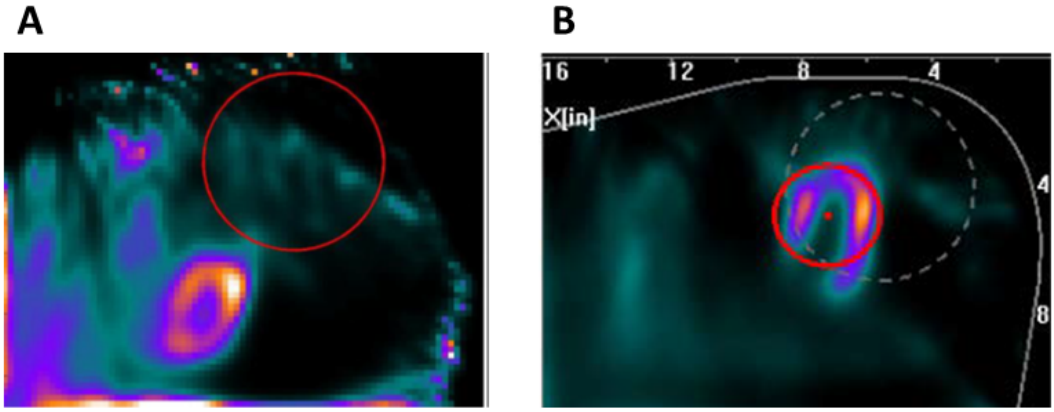

Figure 2.6.10: Examples of incorrect ROI selection. On the pre-scan images a wrong ROI position (A) and a too narrow ROI (B) have been chosen [33].

- **Low count statistics**. In order to improve image quality is important to collect a sufficient number of photons from the LV, otherwise low definition images are obtained (figure 2.6.11 A). With D-SPECT system, the scan can be performed acquiring a pre-defined number of counts from the LV. It has been suggested that 1 M LV counts produce an adequate imaging, which allow for a quantitative analysis [42].
- **Wrong detector head and patient positioning**. During the acquisition, it is recommended to keep the patient's chest as close as possible to the detector head to achieve optimal image quality (as explained in 2.3.1). Some tools are provided by D-SPECT system to assist the operator in choosing the best detector head and patient positions, e.g. the already mentioned inclinometers for the detector head and the patient chair. Another help consists of a gray dashed circular ROI which is displayed in the top view image obtained after the pre-scan (figure 2.6.11 B). This circle defines an area that provides good and relatively uniform resolution. Therefore, ideally the heart representation should occur within this region to get better image quality, but this request is difficult to satisfy when the patients present some characteristics, such as a high BMI or restricted mobility. In these cases, the heart should be placed as close as possible to this gray dashed ROI within the limits of the patient's anatomy.

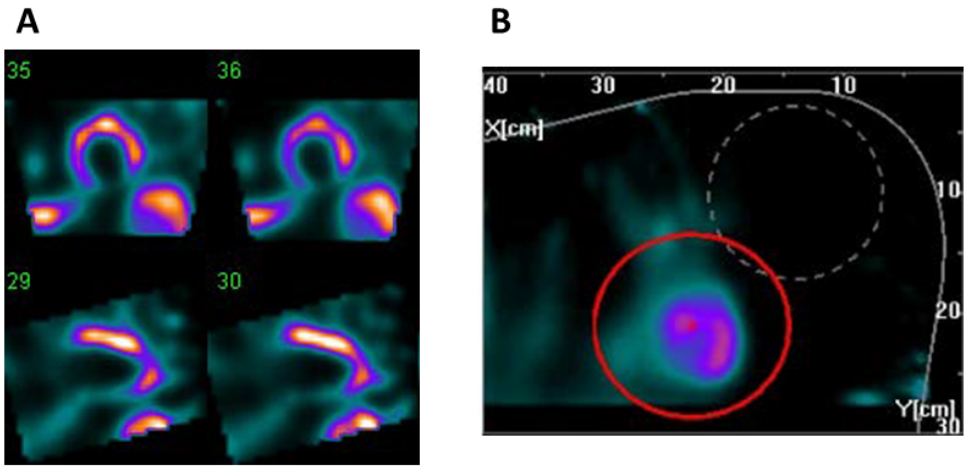

Figure 2.6.11: Examples of low count images and wrong positioning pre-scan. The reconstructed images show relatively low counts (278k) in the LV (A). Pre-scan top view image displays the heart far from the gray dashed ROI, which indicates the area for obtaining the best resolution (B) [33].

Chapter 3

Materials and methods

3.1 Data collection

The images and data used for this thesis were acquired during diagnostic tests performed at the Nuclear Medicine Department of the San Giovanni Battista University Hospital (also known as Molinette Hospital) of Turin (Italy). The SPECT MPI studies were performed with a D-SPECT system, born for cardiac imaging (cf. 2.6.2) and ^{99m}Tc-tetrofosmin served as radiopharmaceutical.
In order to collect all the necessary data, a Graphical User Interface (GUI) was developed using MATLAB App Designer. The information acquired during this phase was used as a reference for training the artificial intelligence algorithms developed in this thesis. After each pre-scan, the GUI showed three images of detected activity distribution, representing the front view, the side view, and the top view (figure 3.1.1). After each acquisition, the operator performed the following three tasks:

- choosing the position and size of the ROI (red ellipse on figure 3.1.1) on which to focus the definitive acquisition;
- indicating, if necessary, possible corrections to improve the centering on the LV; the possible corrections are listed in the table 3.1.1 and some of them are illustrated in figure 3.1.2;
- assigning an image quality rating (from 1 to 10) for the acquired pre-scan and, after the definitive scan acquisition, an image quality rating also for this focused scan.

For each pre-scan, the collected data include:

- three RGB images representing the three pre-scan views of the activity distribution;

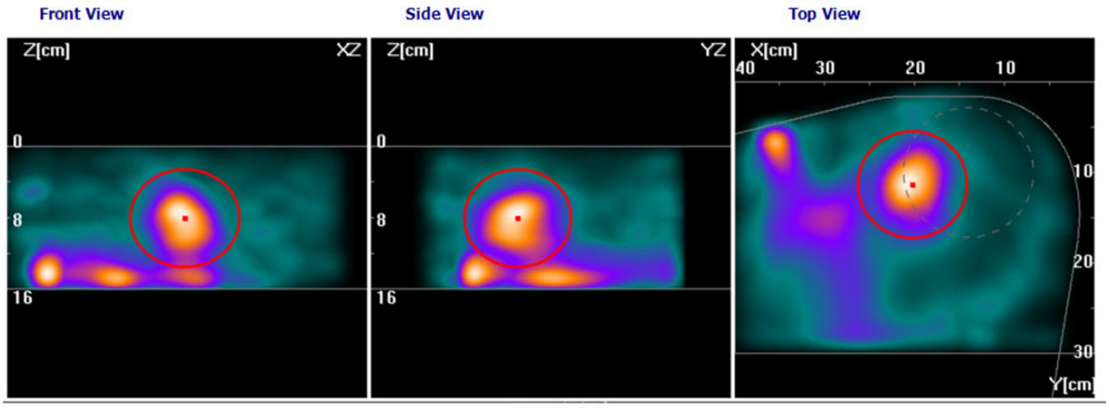

Figure 3.1.1: Example of the three views showed after each pre-scan. The red ellipse is centered on the LV in order to focus the definitive scan.

Semi-upright position	**Supine position**
1) Position the detector head close to the left side of the patient's body	1) Position the detector head close to the left side of the patient's body
2) Raise the chair	2) Move the detector head towards the patient's feet
3) Lower the chair	3) Move the detector head towards the patient's head
4) Position the detector head as close as possible to the patient's chest	4) Raise the table to position the detector head as close as possible to the patient's chest
5) Make the patient drink cold water	5) Make the patient drink cold water
6) Modify the detector head inclination	– – – – – – – – – – – –

Table 3.1.1: Possible corrections to improve the heart centering of the pre-scan in a semi-upright or supine configuration.

- patient information, such as sex, age, height, and weight;
- data relating to the performed cardiac study, such as collected counts, injected activity, time of injection, semi-upright/supine configuration, and rest/stress condition.

The data collection involved 158 different patients (105 males and 53 females). Patient features are described in the table 3.1.2 and in the figures 3.1.3 and 3.1.4.

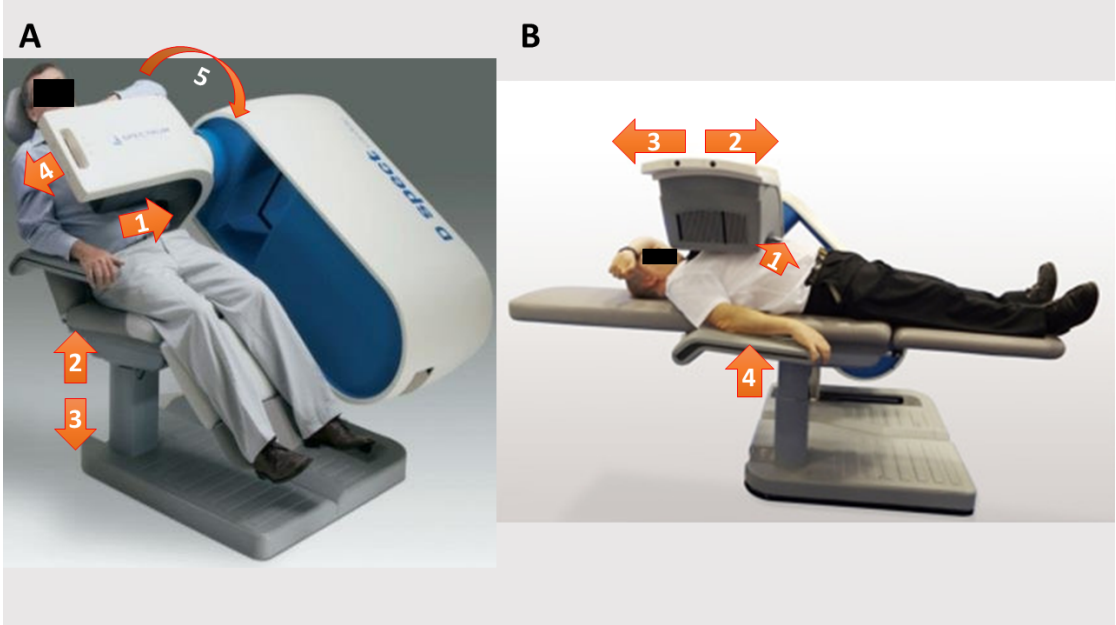

Figure 3.1.2: Possible corrections of the patient-detector configuration to improve heart centering during a D-SPECT examination. A) Semi-upright position: 1. Position the detector head close to the left side of the patient's body. 2. Raise the chair. 3. Lower the chair. 4. Position the detector head as close as possible to the patient's chest. 5. Modify the detector head inclination. B) Supine position: 1. Position the detector head close to the left side of the patient's body. 2. Move the detector head towards the patient's feet. 3. Move the detector head towards the patient's head. 4. Raise the table to position the detector head as close as possible to the patient's chest. Image adapted [49] [6].

Features	**Mean ± Standard deviation**
Age	71 ± 10
Height	168.27 ± 8.27 cm
Weight	76.54 ± 12.86 kg

Table 3.1.2: Details of the collected patient information.

Data from 711 scans were collected, including 490 scans (69%) performed in a semi-upright position and 221 in a supine position (31%). Furthermore, 460 scans (65%) were acquired after a stress test while 251 (35%) in a rest state. In figure 3.1.5 it is possible to observe a correlation between injected activity and patient

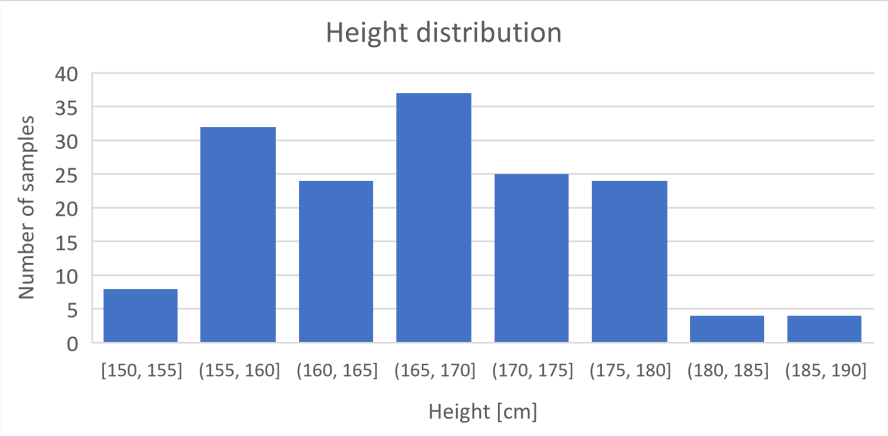

Figure 3.1.3: Distribution of patient heights.

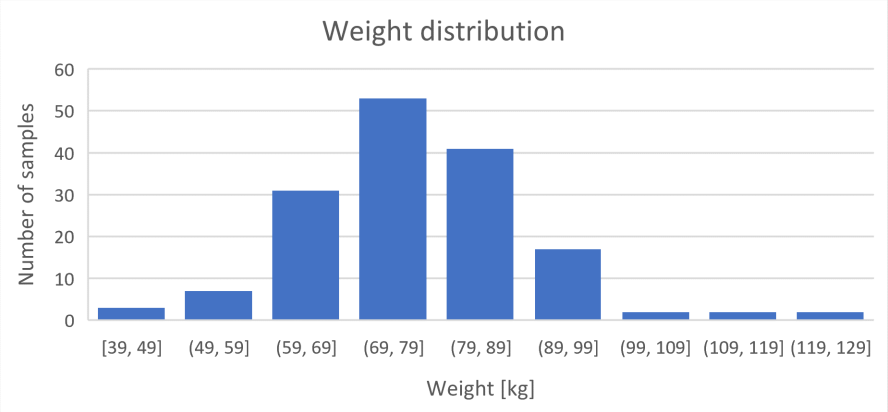

Figure 3.1.4: Distribution of patient weights.

weight, as expected when studies with weight based dosing are performed (cf. 2.5.2).

3.2 Construction of AI algorithms

The developed algorithms have two main goals:

- detect the position of the heart in the pre-scan images;
- check if the adopted configuration needs some of the corrections listed in the table 3.1.1.

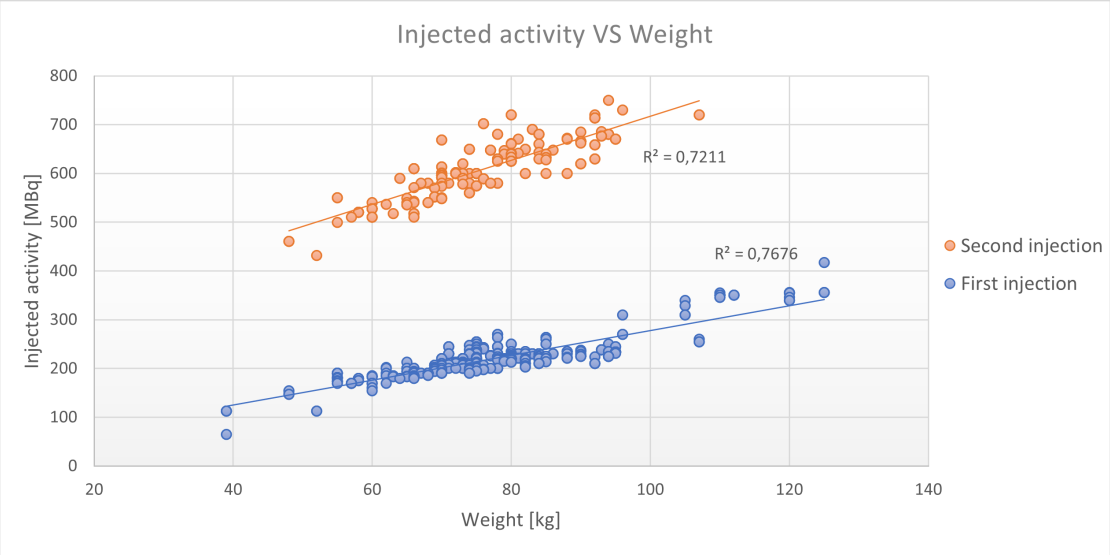

Figure 3.1.5: Scatter plot of injected activity versus patient weight. Second injection administered in the same day requires an higher dose to minimize shine through issues. Trend lines show a correlation between the two variables, as expected for weight based dosing studies.

For both purposes, the algorithms were trained using the indications provided by the operators during the data collection. All the algorithms were implemented using MATLAB programming language.
Before performing the feature extraction from the pre-scan images, the latter were subjected to the following pre-processing steps:

- Removal of the red ROI and other white or gray curves present in the images. The center location of the ellipse and its semi-axis length were saved for the next purposes.
- Pixel intensity for the removed areas were selected by interpolating the neighboring pixels intensities with a cubic spline.
- A median filter (square kernel of side 10) was applied to remove white dashes displayed by some images.

An example of pre-processing application is shown in figure 3.2.1.
Before starting the algorithm construction, the collected data was split in two different dataset, a construction set and a validation set. The latter was not used during the algorithm construction phase, but only during the validation process. 111 patients (about the 70% of the total) were selected randomly and their data

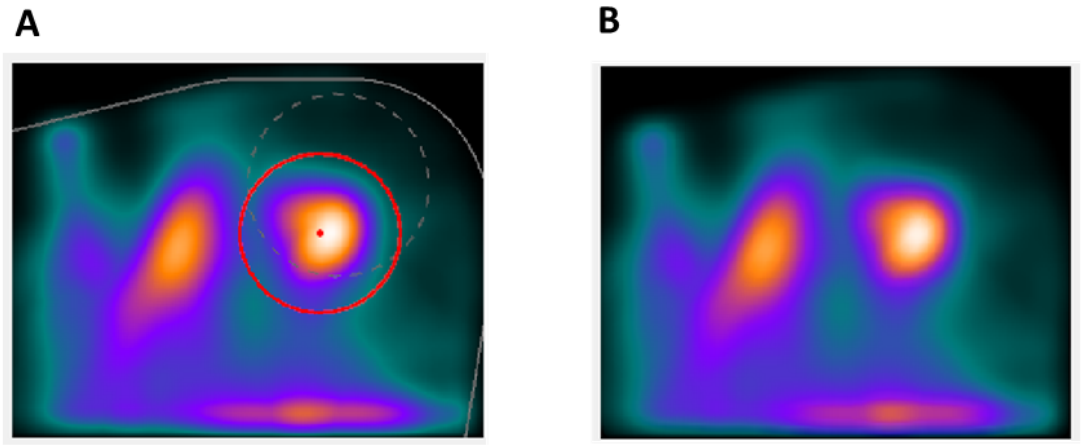

Figure 3.2.1: Example of pre-processing application. The initial image presents a red ROI and some curves and dashes (A), whilst they are absent in the pre-processed image (B).

made up the construction set, whilst the data related to the remaining 47 patients formed the validation set.

3.2.1 Classifier for heart position detection

In order to assess whether the patient positioning is correct, it is first necessary to detect the heart position in the pre-scan images. This task can become tricky, for example if the radiotracer is distributed in some areas other than the heart, and it can be facilitated by using a classifier, an algorithm that assigns an element in a specific class of membership by gaining information from its attributes, also known as features [38].

Feature extraction

The radiotracer used for D-SPECT examinations can accumulate not only in the heart tissues but also in other organs, such as gut and liver. For this reason, the acquired images can present different high intensity areas, among which it is necessary to identify the one relating to the heart. Therefore, features were extracted from each pre-scan image by following these steps:

- As the areas with higher concentration of radiopharmaceutical are colored in red, pixels with high intensity in the red layer need to be emphasized.

A grayscale image was obtained by combining the three layer of the pre-processed RGB image: the weights selected for the red layer, the blue layer and the green layer are respectively 0.8, 0.1 and 0.1.

- The grayscale image was low pass filtered, averaging the values of a 5x5 kernel. This step is important to remove any spourious peaks due to the background noise.
- Regional maxima were detected in the obtained image. They were defined as a connected component of pixels with a constant intensity value, surrounded by pixels with a lower value (Matlab function: imregionalmax). Only the peaks with an intensity greater than 50% of the highest maximum were considered.
- In some cases the heart region reports blue and not red pixels, so that the peak relative to the heart would be difficult to identify by this algorithm (figure 3.2.2). Therefore, if fewer than 5 peaks were selected in the previous step, other regional maxima were identified in a new combination of the three RGB image layers (weights 0.8, 0.1 and 0.1 for blue, green and red layers, respectively). Also in this case only the peaks with intensity greater than 50% of the highest intensity were selected up to a maximum of 5 new peaks.
- Starting from each identified peak, a segmentation of the region to which this maximum belongs was identified using the following steps:
  - For each pixel of the grayscale filtered image, the absolute value of the difference between the intensity of that pixel in the grayscale image and the intensity of the considered peak was calculated. A matrix with the same size of the image was created, entering for each element a value inversely related to the difference previously calculated. In this way, large values were attributed to pixels with an intensity close to the peak value (Matlab function: graydiffweight).
  - This matrix was used as input of a segmentation algorithm based on the Fast Marching Method (the peak under consideration serves as a seed for the algorithm and the segmentation threshold is 0.001). An example of this algorithm application is showed in figure 3.2.3.
- All the obtained segmentations were used to extract the following features: centroid coordinates, area, circularity, eccentricity, and orientation (i.e. the angle between the direction of maximum extension of the region and the horizontal axis).

Three different datasets were created, one for each image of the three pre-scan views, containing the features of the peaks detected in the relative images. In these datasets each peak is related to the following 8 features:

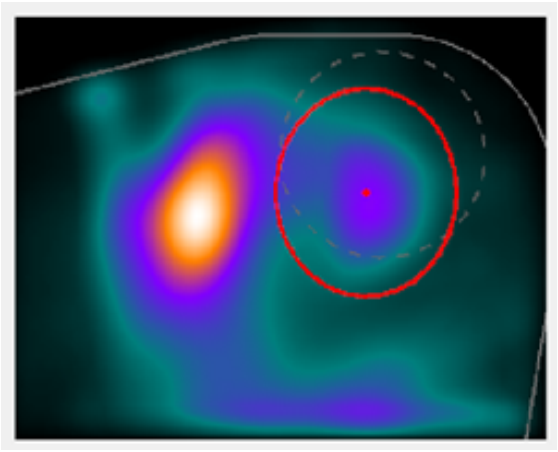

Figure 3.2.2: Example of region related to the heart with blue pixels.

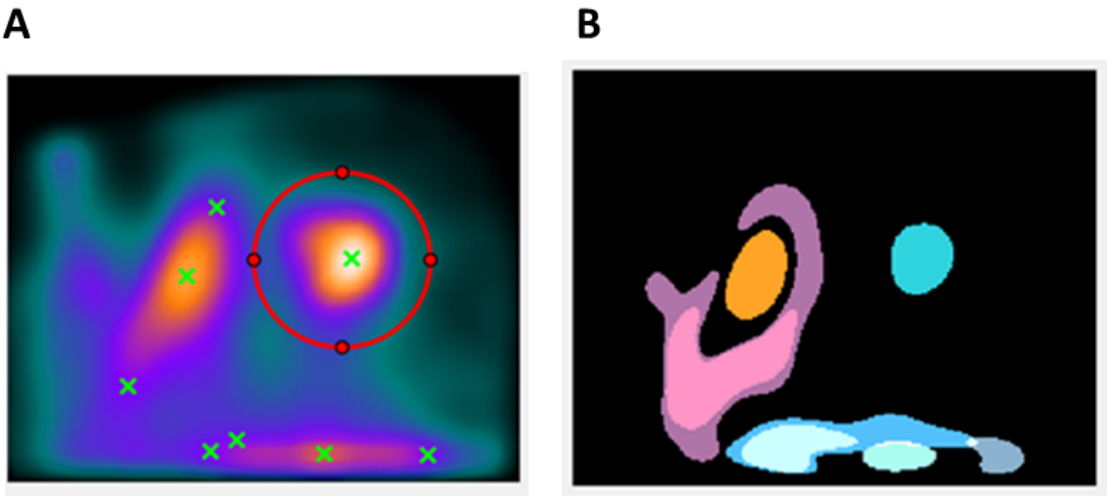

Figure 3.2.3: Example of segmentation algorithm application. The regional peaks (green crosses) are detected on the pre-processed RGB image (A). The obtained segmentations of the areas corresponding to the identified peaks are indicated with different random colors.

- intensity and position (x-value and y-value) of the peak;
- euclidean distance between the peak and the centroid of the segmented area related to the peak;
- area, circularity, eccentricity and orientation of the segmented region.

These features were used as inputs for the classification between the class of the peaks related to the heart and the class of the maxima not related to the heart, which will be called class 1 and class 0, respectively. The peaks belonging to class 1 were identified as the closest to the red ROI center, provided by the operator during the data collection. The three datasets were normalized with the min-max scaling technique (saving maximum and minimum values) and used to develop three different classifier, one for each view in the pre-scan.

Training Set Construction

The construction of the training set for each classifier was performed considering the same number of elements for both classes, in order to obtain a balanced training set. In particular, the amount of elements to select among those in the construction set was set approximately equal to 50% of the elements belonging to the less represented class (in this case, class 1). Unselected samples in the construction set formed the test set.
The selection of the elements to insert in the training set was made through three different methods: random sampling, dendrogram, and Self-Organizing Map (SOM). The latter two are unsupervised machine learning technique which allowed for clustering the elements of both classes. For each cluster of each class, an amount of elements proportional to the cluster size was selected.
For the dendrogram technique, the maximum distance method was always used, but three tests were performed, each with a different distance metric: euclidean, cityblock, and chebychev. In order to choose the correct number of clusters, a natural cut was used for the dendrograms.
Two tests were performed with the SOM technique, one using a 4x4 SOM and another with a 5x5 SOM. Dendrograms with the maximum distance method and euclidean distance metric was constructed for clustering the neurons of the SOMs.
The best test for both clustering techniques was chosen considering two variables: the maximum intra-cluster variability and the minimum inter-cluster distance. A good test should present a low maximum intra-cluster variability and a high minimum inter-cluster distance.
In this way, for each classifier three different training and test set couples were created, using a random sampling, dendrogram, and SOM.

Tuning of the classifier parameters

In order to solve the concerned classification problem, a Support Vector Machine (SVM) classifier was employed. This is a supervised learning model which searches for the hyper-surface that best separates two classes, but it can be chosen also for a multi-class problem, using a combination of binary classifier [38].

Different parameters of a SVM model can be optimized. In this study, different values were assigned to the kernel scale and the box constraint level, in order to find the combination of these parameters that best solve the classification problem. Specifically, both parameters were set to the following values: 0.001, 0.01, 0.1, 1, 10, 100, 1000.
The classification error was calculated on both the training set and the test set using all the possible combinations of the two parameters. Only one parameters pair was chosen for each training and test set couples of each classifier.

Selection of the training and test set pair

After selecting the best combination of parameters, one training and test set couple was selected for each of the three classifiers (one for each pre-scan view). This choice was based on the classification results obtained on training, test and validation sets.
Once the best model was identified for the three classifiers, this was applied for detecting the heart position in the corresponding view of the pre-scan. Specifically, the three constructed classifier were employed in this way:

- for each pre-scan image, peaks and relative segmentated areas were detected, following the procedure already used for the feature extraction;
- after obtaining the features of the detected peaks, they were provided as inputs to the constructed classifier, in order to assess which of the identified maxima was that related to the heart;
- for each image, one and only one peak should be related to the heart; SVM models can return a classification score which was used to assess the only heart peak.

3.2.2 Classifiers for possible centering corrections

Once detected the regional maximum which is related to the heart for each image of the pre-scan, features linked to this peak were extracted, in order to check if any corrections were needed to improve the acquisition centering
Considering the information provided by the operators during the data collection, the acquired pre-scans were split in 8 different categories for the ones obtained in a semi-upright position and 7 categories for the scans in a supine configuration. Indeed, two new categories were added to the possible corrections reported in the table 3.1.1. These new categories refer to the acquisitions without any reported corrections. One category was formed by the pre-scans with an image quality rating greater than or equal to 6 (this was called "OK" category), and the other was composed by the acquisitions with an image quality rating less than 6 (this

was named "OK but low quality"). This distinction was made to ensure a good quality for the images in the "OK" class.
The amount of the collected pre-scans for each category and in both upright and supine position is showed in table 3.2.1.

	Pre-scans numbers		**Category name**	
Class	**Upright**	**Supine**	**Upright**	**Supine**
1	14	13	Position the detector head close to the left side of the patient's body	Position the detector head close to the left side of the patient's body
2	134	51	Raise the chair	Move the detector head towards the patient's feet
3	74	34	Lower the chair	Move the detector head towards the patient's head
4	16	9	Position the detector head as close as possible to the patient's chest	Raise the table to position the detector head as close as possible to the patient's chest
5	89	49	Make the patient drink cold water	Make the patient drink cold water
6	1	– – – –	Modify the detector head inclination	– – – – – – – – – – – –
7	190	89	OK	OK
8	10	3	OK but low quality	OK but low quality

Table 3.2.1: Number of the collected pre-scans for each category. The name of the category is reported and the amount of pre-scans is indicated for both upright and supine configuration.

The classes 1, 4, 6, and 8 showed a low number of elements compared to the other categories. The work of this thesis was focused on the classification of the elements belonging to the classes 2, 3, 5, and 7, in order to avoid the construction of classifiers strongly unbalanced between the classes.
Some pre-scans were labeled with more than one category: 38 upright acquisitions and 23 supine acquisitions. Therefore, the classification problem does not require a single class to be assigned, but more than one correction may be required for the

same pre-scan. Therefore, the classification problems was split in two sub-problems described below.

Classifier for classes 2, 3, 7

The first analyzed question involved the classes 2, 3, and 7 previously described: for the upright configuration, the goal was to check whether the chair was in the right position or whether it was necessary to raise or lower it; for the supine configuration, the issue concerned the assessment of the detector head position, which could be moved towards the patient's feet or towards the patient's head.
On average, the first two images of the pre-scan (front and side views) showed the activity region related to the heart at different y-axis values among these three classes: for both upright and supine configurations, images belonging to class 2 presented the heart region in a lower position, while the acquisitions in class 3 reported an upper heart location; images in class 7, which did not need any corrections, showed the heart region at an intermediate height compared to the other two classes (figure 3.2.4).
For this reason, this classification problem was solved using the previously extracted peak features (peak coordinates and the information associated with the segmented area), but considering only the peaks related to the heart region (detected by the classifiers already constructed). 16 features were therefore attributed to each pre-scan, 8 from the front view and 8 from the side view. This data were normalized using the min-max scaling technique (saving the maxima and minima value).
The construction of the training set was performed considering the same number of elements (70% of the elements belonging to the less represented class) for all the classes. The selection of the elements to insert in the training set was made using the dendrogram technique. The maximum distance method was always used and three tests were performed, each with a different distance metric: euclidean, cityblock, and chebychev. In order to choose the correct number of clusters, a natural cut was used for the dendrograms. The best test was chosen considering the maximum intra-cluster variability and the minimum inter-cluster distance.
For this classifier a feature selection was performed. For this procedure a ranking method was adopted, using a random forest classifier. Random forest is an ensemble learning method, suitable for both classification and regression tasks. This method builds multiple decision trees and merges them together to get a more accurate and stable prediction. The ensemble classifier applies two sources of randomness: the bagging method, which consists in training different trees on different subsets of the original dataset and aggregating the outputs of learners; the selection of a random subset of the predictors for each split in a tree (the decision at that node is based only on these selected predictors). Therefore, the main

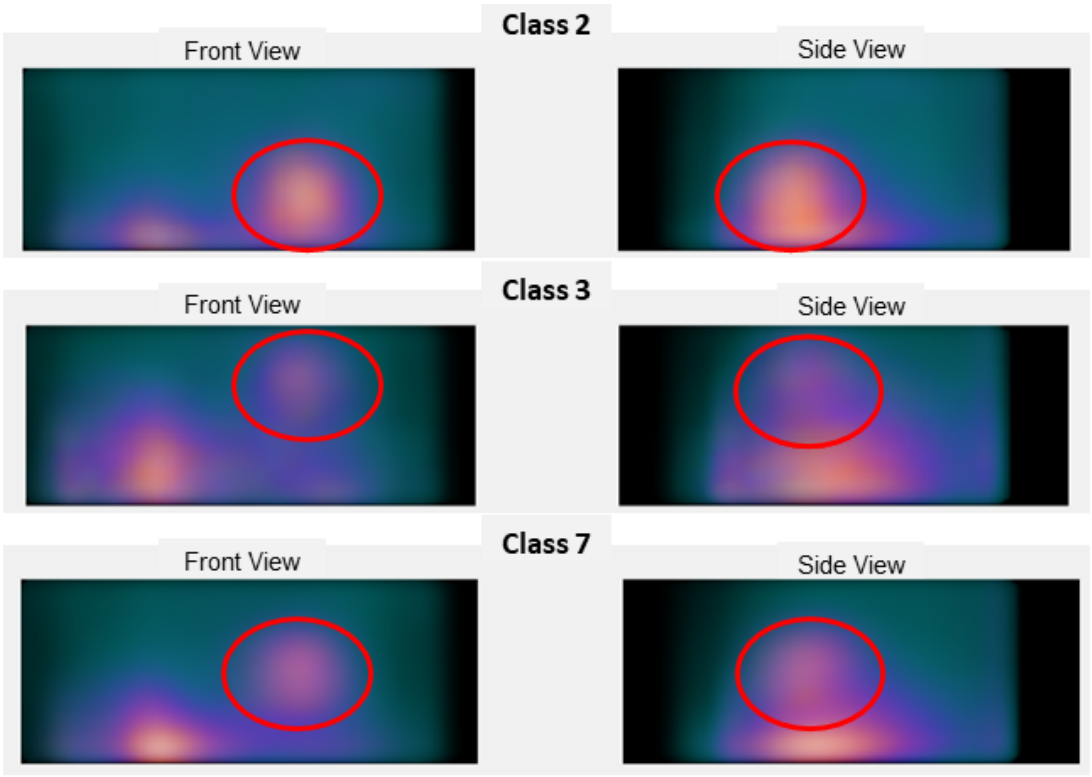

Figure 3.2.4: Mean of front and side view images of the pre-scans belonging to class 2, 3, and 7. The red ellipses indicate the activity region related to the heart.

parameters of a random forest classifier are the number of trees and the number of predictors to select at each node. The observations, that each decision tree does not use for its training, are called out-of-bag (OOB) samples. The accuracy of the model on the training set can be estimated using the OOB error, that is the classification error obtained by predicting each observation using the trees for which that element was OOB. Furthermore, random forest uses a metric (e.g. Gini index) for selecting the splitting criterion at each node and this measure can be utilized to highlight the importance of each variable.
The feature selection procedure was based on the following steps:

- In order to find the best parameter combination for the random forest, different values of number of trees and number of variables to sample were assigned. Specifically, 20, 60, 100, 140, 180 trees were utilized and the number of variables to sample was set to 2, 4, 6, 8, 10. The best parameter pair was selected considering the OOB error on the training set and the classification error on the test set.

- The optimized classifier provided a variable importance estimation based on the Gini index. In order to perform the feature selection, the classification error of the model on the test set was calculated adding the features one by one, from the most important to the least important. The error trend as a function of the number of selected variables was used to choose how many features were needed to get sufficient performance.

Two SVM models were trained, one using all features and the other with only the selected variables. Both models were optimized by assigning different values of kernel scale and box constraint level. Specifically, both parameters were set to the following values: 0.001, 0.01, 0.1, 1, 10, 100, 1000. The classification error was calculated on both the training set and the test set using all the possible combinations of the two SVM parameters. Considering the obtained error values, the best parameters pair was selected for both models.
In order to identify the best classifier between the one with only the selected features and the one trained with all features, classification performances of the optimized SVM classifiers were calculated on training set, test set and validation set.

Classifier for classes 5 and 7

The second sub-problem concerned the distinction between acquisitions which present the need to "make the patient drink cold water" (class 5) and those that do not require any corrections (class 7). It is suggested to make the patient drink cold water if a high extra-cardiac activity is recorded, since this procedure can speed up the washout of gut uptake (cf. 2.6.3). Indeed, images belonging to class 5 on average presented a lower distinction between the region related to the heart and the other high intensity areas, especially in the front view and the top view. This can be seen in figure 3.2.5, which shows the mean of the three images of the pre-scan for class 5 and class 7.
In order to highlight this difference between the two classes, new segmented areas were obtained for the regions related to the heart: fast marching method was used with a segmentation threshold higher than the one previously adopted (0.05 instead of 0.001). In this way, segmentations with a larger number of pixels were obtained, including also the surrounding area which presented important characteristics for the distinction between the two classes. An example of region related to the heart segmented with the two thresholds is shown in figure 3.2.6.
Pixels of the pre-scan images (converted into grayscale images) which were included in the new segmentations were used to extract 22 statistical variables:

- mean, standard deviation, skewness, kurtosis;

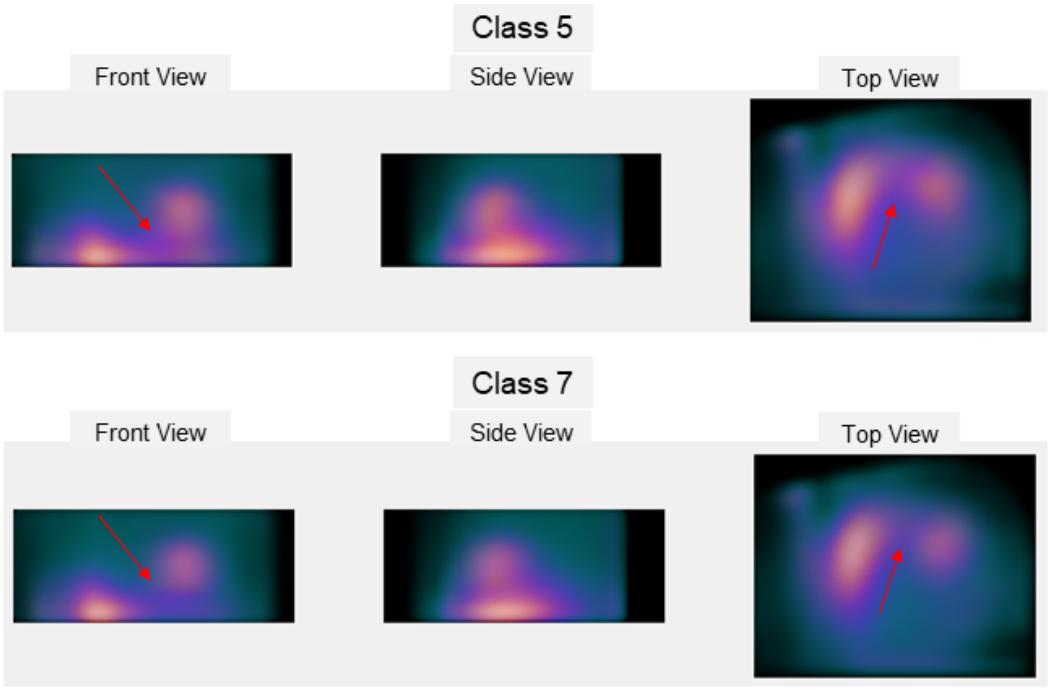

Figure 3.2.5: Mean of three views of the pre-scans belonging to class 5 and 7. The red arrows indicate the activity distribution differences between the two classes.

- texture variables (Gray-Level Co-occurence Matrix (GLCM)): energy, contrast, correlation, variance, inverse difference moment, sum average, sum variance, sum entropy, entropy, difference variance, difference entropy, information measure of correlation, homogeneity, autocorrelation, dissimilarity, cluster shade, cluster prominence, maximum probability.

These features were extracted for the three images of each pre-scan, but only those obtained from the front view and the top view were used, as these two images showed a greater difference between the two classes.

The training set for this classifier was constructed using the previously mentioned procedure: the same number of elements (70% of the elements belonging to the less represented class) was used for both classes and this selection was performed with the dendrogram technique. The maximum distance method was always used and three tests were performed, each with a different distance metric: euclidean, cityblock, and chebychev. In order to choose the correct number of clusters, a natural cut was used for the dendrograms. The best test was chosen considering the maximum intra-cluster variability and the minimum inter-cluster distance.

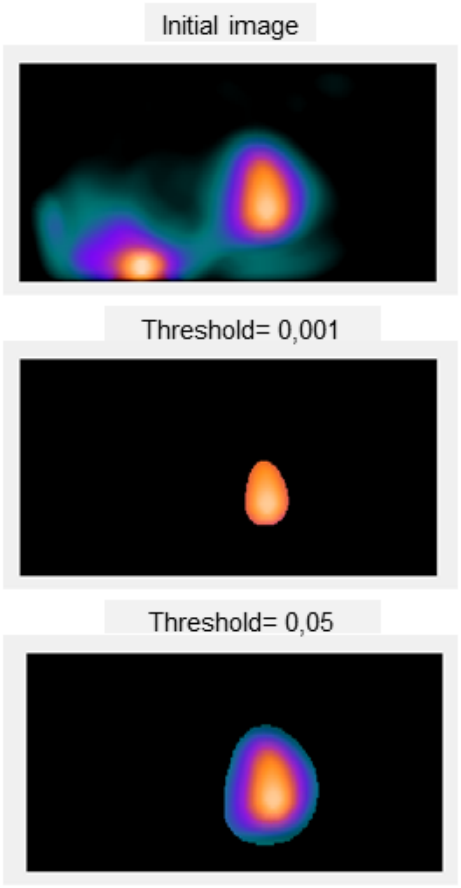

Figure 3.2.6: Example of segmentation of the region related to the heart with two different threshold.

Even for this classifier a feature selection was performed, in order to reduce the great amount of features (44 for each pre-scan). The selection procedure was performed in the same way as for the classifier 2vs3vs7.
Two SVM models were trained, one using all features and the other with only the selected variables. Both models were optimized by assigning different values of kernel scale and box constraint level. The classification error was calculated on both the training set and the test set using all the possible combinations of the two SVM parameters. Considering the obtained error values, the best parameters pair was selected for both models.
In order to identify the best classifier between the one with only the selected features and the one trained with all features, classification performances of the optimized SVM classifiers were calculated on training set, test set and validation set.

Chapter 4

Results

4.1 Classifier for heart position detection

Since each pre-scan is formed by three images (one for each view), three classifier were constructed: classifier 1 for the front view, classifier 2 for the side view and classifier 3 fort the top view. Three training and test set couples were selected for each classifier. The three training sets of each classifier were created using random sampling, dendrogram and SOM techniques.
The dendrograms obtained for the three classifier are shown in figures 4.1.1, 4.1.2, 4.1.3. Maximum intra-cluster variability (max-intra-var) and minimum inter-cluster distance (min-inter-dist) of each test (with different distance metrics) for the three classifier are reported in tables 4.1.1, 4.1.2, 4.1.3.

Classifier 1 - Dendrogram					
Class 0			**Class 1**		
Metric	**Max-intra-var**	**Min-inter-dist**	**Metric**	**Max-intra-var**	**Min-inter-dist**
euclidean	0.5268	0.3965	euclidean	0.4003	0.5308
cityblock	0.5339	0.4316	cityblock	0.4347	0.3664
chebychev	0.5534	0.3427	chebychev	0.3841	0.3434

Table 4.1.1: Max-intra-var and min-inter-dist values of the clusters formed by dendrograms for classifier 1. Max-intra-var: maximum intra-cluster variability. Min-inter-dist: minimum inter-cluster distance.

For the classifier 1, cityblock metric was preferred for class 0 and euclidean metric was chosen for class 1 because they showed the highest min-inter-dist whilst their max-intra-var presented an intermediate value compared to the others.

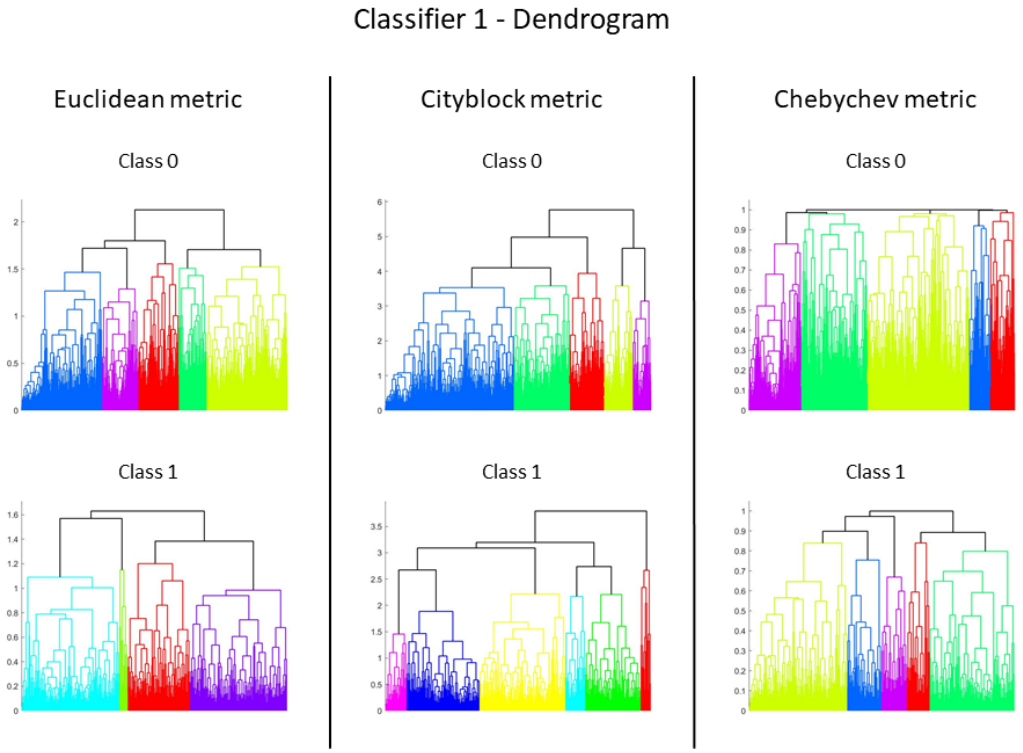

Figure 4.1.1: Dendrograms with three different metrics for classifier 1.

Classifier 2 - Dendrogram					
Class 0			**Class 1**		
Metric	**Max-intra-var**	**Min-inter-dist**	**Metric**	**Max-intra-var**	**Min-inter-dist**
euclidean	0.5578	0.4630	euclidean	0.3542	0.4701
cityblock	0.6017	0.4637	cityblock	0.3473	0.4507
chebychev	0.6317	0.3621	chebychev	0.4375	0.2631

Table 4.1.2: Max-intra-var and min-inter-dist values of the clusters formed by dendrograms for classifier 2. Max-intra-var: maximum intra-cluster variability. Min-inter-dist: minimum inter-cluster distance.

For the classifier 2, euclidean metric was preferred for both class 0 and class 1 as it showed the smallest max-intra-var in class 0 and the highest min-inter-dist in class 1.

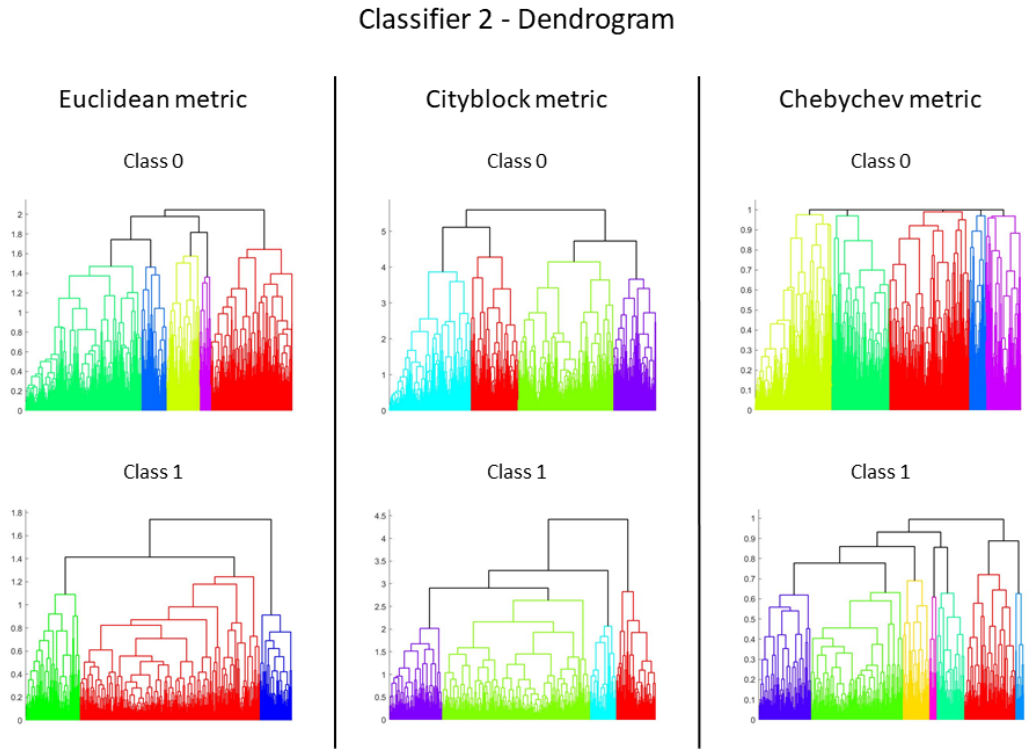

Figure 4.1.2: Dendrograms with three different metrics for classifier 2.

Classifier 3 - Dendrogram					
Class 0			**Class 1**		
Metric	**Max-intra-var**	**Min-inter-dist**	**Metric**	**Max-intra-var**	**Min-inter-dist**
euclidean	0.5227	0.4376	euclidean	0.3202	0.3491
cityblock	0.5287	0.4499	cityblock	0.3936	0.5229
chebychev	0.5831	0.4607	chebychev	0.3703	0.4593

Table 4.1.3: Max-intra-var and min-inter-dist values of the clusters formed by dendrograms for classifier 3. Max-intra-var: maximum intra-cluster variability. Min-inter-dist: minimum inter-cluster distance.

For the classifier 3, cityblock metric was preferred for class 0 since it presented a low max-intra-var and an intermediate value of min-inter-dist, while chebychev

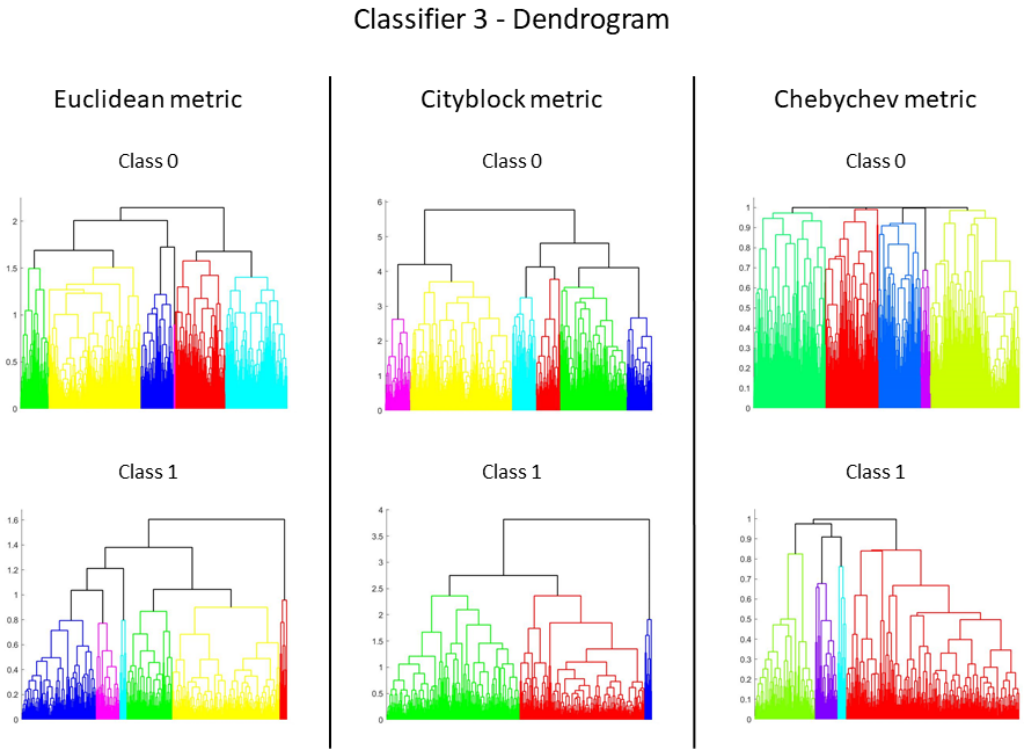

Figure 4.1.3: Dendrograms with three different metrics for classifier 3.

metric was chosen for class 1 because it showed max-intra-var and min-inter-dist with intermediate values compared to the others.
As regards the tests conducted with the SOMs, the neuron clusters obtained for the three classifier are shown in figures 4.1.4, 4.1.5, 4.1.6. Max-intra-var and min-inter-dist values of each test (with different SOM sizes) for the three classifier are reported in tables 4.1.4, 4.1.5, 4.1.6.
For the classifier 1, 5x5 SOM was selected for class 0 because it showed a smaller max-intra-var, while for class 1 the 4x4 SOM presented the lowest max-intra-var.
For the classifier 2, 4x4 SOM was chosen for class 0 as it showed a much higher min-inter-dist, whilst 5x5 SOM showed the highest min-inter-dist for class 1.
Finally, for the classifier 3, 5x5 SOM was preferred for class 0 as it showed a bigger min-inter-dist, whilst 5x5 SOM presented a much smaller max-intra-var for class 1.
For each training and test couple of each classifier, the classification error was calculated using all the possible combinations of kernel scale and box constraint level values (figures 4.1.7, 4.1.8, 4.1.9).

Classifier 1 - SOM					
Class 0			Class 1		
Size	**Max-intra-var**	**Min-inter-dist**	**Size**	**Max-intra-var**	**Min-inter-dist**
4x4	0.5651	0.5209	4x4	0.4141	0.4779
5x5	0.5018	0.5066	5x5	0.4461	0.4998

Table 4.1.4: Max-intra-var and min-inter-dist values of the neuron clusters formed by SOMs for classifier 1. Max-intra-var: maximum intra-cluster variability. Min-inter-dist: minimum inter-cluster distance.

Classifier 2 - SOM					
Class 0			Class 1		
Size	**Max-intra-var**	**Min-inter-dist**	**Size**	**Max-intra-var**	**Min-inter-dist**
4x4	0.5555	0.7569	4x4	0.3349	0.4724
5x5	0.4982	0.4987	5x5	0.3456	0.4875

Table 4.1.5: Max-intra-var and min-inter-dist values of the neuron clusters formed by SOMs for classifier 2. Max-intra-var: maximum intra-cluster variability. Min-inter-dist: minimum inter-cluster distance.

Starting from the classifier 1, for all the training and test set couples, low classification errors were obtained using a kernel scale equal to 0.1 with all the possible values of box constraint level. This value of kernel scale was chosen for all the training and test set couples. Furthermore, considering the classification error on the test set, the best box constraint value was 0.1 for random sampling and SOM, and 0.01 for dendrogram.
As regards the classifier 2, following the same reasoning, the best [kernel scale;box constraint level] combination was [0.1;1] for the random sampling and [0.1,0.1] for dendrogram and SOM.
Also for the classifier 3, a kernel scale equal to 0.1 was preferred because it always showed a small classification error. Considering the results obtained on the test set, the box constraint level was set to 0.1 for all the training and test combinations.
The classification results obtained by the three tuned SVM models (trained on the three different training set) on training set, test set and validation set are represented in figures 4.1.10 and 4.1.11 for the classifier 1, 4.1.12 and 4.1.13 for the classifier 2, and 4.1.14 and 4.1.15 for the classifier 3. The performances of the classifiers are shown by using confusion matrices. Considering class 1 (i.e.

Classifier 3 - SOM					
Class 0			Class 1		
Size	**Max-intra-var**	**Min-inter-dist**	**Size**	**Max-intra-var**	**Min-inter-dist**
4x4	0.5437	0.5748	4x4	0.4687	0.4446
5x5	0.5556	0.6232	5x5	0.3202	0.3958

Table 4.1.6: Max-intra-var and min-inter-dist values of the neuron clusters formed by SOMs for classifier 3. Max-intra-var: maximum intra-cluster variability. Min-inter-dist: minimum inter-cluster distance.

peaks relative to the heart) as the positive class, sensitivity was defined as the ratio between the number of correctly classified elements in class 1 and the total amount of elements really belonging to class 1. Similarly, specificity was defined as the percentage of correctly classified elements for class 0. Sensitivity and specificity were reported in the diagonal, next to each confusion matrix.

As regards the classifier 1, the random sampling showed excellent results on the class 1 but it did not perform on the class 0 as well. Dendrogram and SOM reported a better balance between the classification error of the two classes. Between these two, SOM technique was preferred because it presented a better classification performance on the validation set for both classes.

For the classifier 2, SVM model constructed using the dendrogram technique was selected because it presented a greater ability to generalize: it showed the best results on test set and validation set, even though a worse performance was obtained on training set. SOM technique exceeded dendrogram performances only for the class 1 in validation set; nevertheless, dendrogram showed a better balance between the two classes.

Random sampling was selected as the best option for the classifier 3. Despite dendrogram technique reported the best performances for class 0 on training set and SOM method was the best for class 1 on test set, random sampling results for both classes on validation set were not equaled by the others techniques.

4.2 Classifiers for possible centering corrections

4.2.1 Classifier for classes 2, 3, 7

The dendrograms obtained for the this classifier are shown in figure 4.2.1. Maximum intra-cluster variability (max-intra-var) and minimum inter-cluster distance

(min-inter-dist) of each test (with different distance metrics) are reported in table 4.2.1,

Classifier 2vs3vs7 - Dendrogram		
Class 2		
Metric	**Max-intra-var**	**Min-inter-dist**
euclidean	0.6129	0.8939
cityblock	0.7016	0.9263
chebychev	1.1030	0.5183
Class 3		
Metric	**Max-intra-var**	**Min-inter-dist**
euclidean	0.6333	0.7351
cityblock	0.6385	0.7265
chebychev	0.7053	0.5524
Class 7		
Metric	**Max-intra-var**	**Min-inter-dist**
euclidean	0.5921	0.6302
cityblock	0.8461	0.6537
chebychev	0.6295	0.4854

Table 4.2.1: Max-intra-var and min-inter-dist values of the clusters formed by dendrograms for classifier 2vs3vs7. Max-intra-var: maximum intra-cluster variability. Min-inter-dist: minimum inter-cluster distance.

Euclidean metric was chosen for class 2, since it showed the lowest value of max-intra-var and a quite high value of min-inter-dist. Also for class 3 euclidean metric was selected because it presented the highest min-inter-dist and the smallest max-intra-var. Euclidean metric was preferred for class 7 too, as it reported the lowest max-intra-var and its min-inter-dist was quite high.
Once the training set was constructed, random forest parameters (number of trees and number of variables to sample) were tuned in order to perform the feature selection. For each parameter pair, the OOB error on the training set and classification error on the test set were calculated (figure 4.2.2).
A number of trees equal to 180 showed the lowest classification error on the training set with a number of variables to sample equal to 8. These parameter pair provided a low classification error on test set, so this combination was selected.
The optimized random forest classifier provided an estimation of feature importance, which is reported in figure 4.2.3. The variable numbers refer to the feature

list reported in 3.2.1 and the first eight variables resulted from the front view image while the last eight from the side view image.
The trend of the classification error on test set as a function of the number of selected variables is shown in figure 4.2.4.
From the observation of this graph, it is evident that the lowest error is obtained with a number of selected variables equal to six. So the six most important variables were selected, three of which resulted from the front view image (peak x-value, peak y-value, centroid-to-peak distance) and the remainign three were extracted from the side view image (peak intensity, peak y-value, segmented region area).
Two SVM models were created, one using all features and the other with only the selected variables. The classification error was calculated on training set and test set, using all the possible combinations of kernel scale and box constraint level values, for both models (figure 4.2.5).
For the classifier without feature selection, one of the lowest error on test set was provided by a box constraint level of 0.1 and a kernel scale equal to 0.001. This parameter combination allows for a very low classification error also on the training set, so the mentioned values were chosen. As regards the SVM model with only the selected features, different parameter pairs provided good results on both training set and test set. The one selected for this classifier has both box constraint level and kernel scale equal to 0.01.
Figure 4.2.6 shows the performance achieved by the two SVM models on training set, test set and validation set. The percentages of correctly classified elements in the three classes (calculated as the ratio between correctly classified elements and the total of elements really belonging to that class) were reported in the diagonal, next to each confusion matrix.
Even if the model without feature selection provided better results for the class 7 on test set and validation set, the classifier constructed using all features was selected because it presented more balanced classification errors among the three classes.

4.2.2 Classifier for classes 5 and 7

The dendrograms obtained for this classifier are shown in figure 4.2.7. Maximum intra-cluster variability (max-intra-var) and minimum inter-cluster distance (min-inter-dist) of each test (with different distance metrics) are reported in table 4.2.2,
For class 5, euclidean metric was selected because it reported the lowest max-intra-var value and an intermediate value for min-inter-dist. Cityblock metric was selected for class 7, as it showed the largest value of min-inter-dist and an intermediate value of max-intra-var.

Classifier 5vs7 - Dendrogram		
Class 5		
Metric	**Max-intra-var**	**Min-inter-dist**
euclidean	0.6792	0.8224
cityblock	0.7358	0.8137
chebychev	1.0331	1.5520
Class 7		
Metric	**Max-intra-var**	**Min-inter-dist**
euclidean	0.8150	0.7732
cityblock	0.8516	0.9274
chebychev	1.3671	0.5443

Table 4.2.2: Max-intra-var and min-inter-dist values of the clusters formed by dendrograms for classifier 5vs7. Max-intra-var: maximum intra-cluster variability. Min-inter-dist: minimum inter-cluster distance.

Once the training set was constructed, random forest parameters (number of trees and number of variables to sample) were tuned in order to perform the feature selection. For each parameter pair, the OOB error on the training set and classification error on the test set were calculated (figure 4.2.8).

The lowest error on test set was obtained with 60 trees and 2 variables to sample, but this combination did not provide good performance on training set. The second best result on test set was reached with 100 trees and 4 variables to sample and this parameter pair was chosen since it also showed a low OOB error on training set.

The optimized random forest classifier provided an estimation of feature importance, which is reported in figure 4.2.9. The variable numbers refer to the feature list reported in 3.2.2 and the first 22 variables resulted from the front view image while the last 22 from the top view image.

The trend of the classification error on test set as a function of the number of selected variables is shown in figure 4.2.10.

From the observation of this graph, it is possible to state that the error presented a downward trend until the tenth feature in importance was employed, even if some peaks were recorded before adding this variable. The nine most important variables were selected, six of which were extracted from the front view image (sum entropy, entropy, difference entropy, information measure of correlation, homogeneity, dissimilarity) and the remaining three features resulted from the top view image (standard deviation, correlation, homogeneity).

Two SVM models were created, one using all features and the other with only the selected variables. The classification error was calculated on training set and test set, using all the possible combinations of kernel scale and box constraint level values, for both models (figure 4.2.11).
For the classifier without feature selection, the kernel scale was set to 1 and the box constraint level was set to 10, in order to find a compromise between the results reported on the two sets (training and test set). As regards the SVM model with only the selected features, different parameter pairs provided good results on both training set and test set. The one selected for this classifier has box constraint level and kernel scale equal to 0.01.
Figure 4.2.12 shows the performance achieved by the two SVM models on training set, test set and validation set. The percentages of correctly classified elements in the two classes (calculated as the ratio between correctly classified elements and the total of elements really belonging to that class) were reported in the diagonal, next to each confusion matrix.
The classifier constructed using only the selected features was preferred because it presented a greater ability to generalize: it showed better results for class 7 on validation set, even though a worse performance was obtained for class 5 on training set.

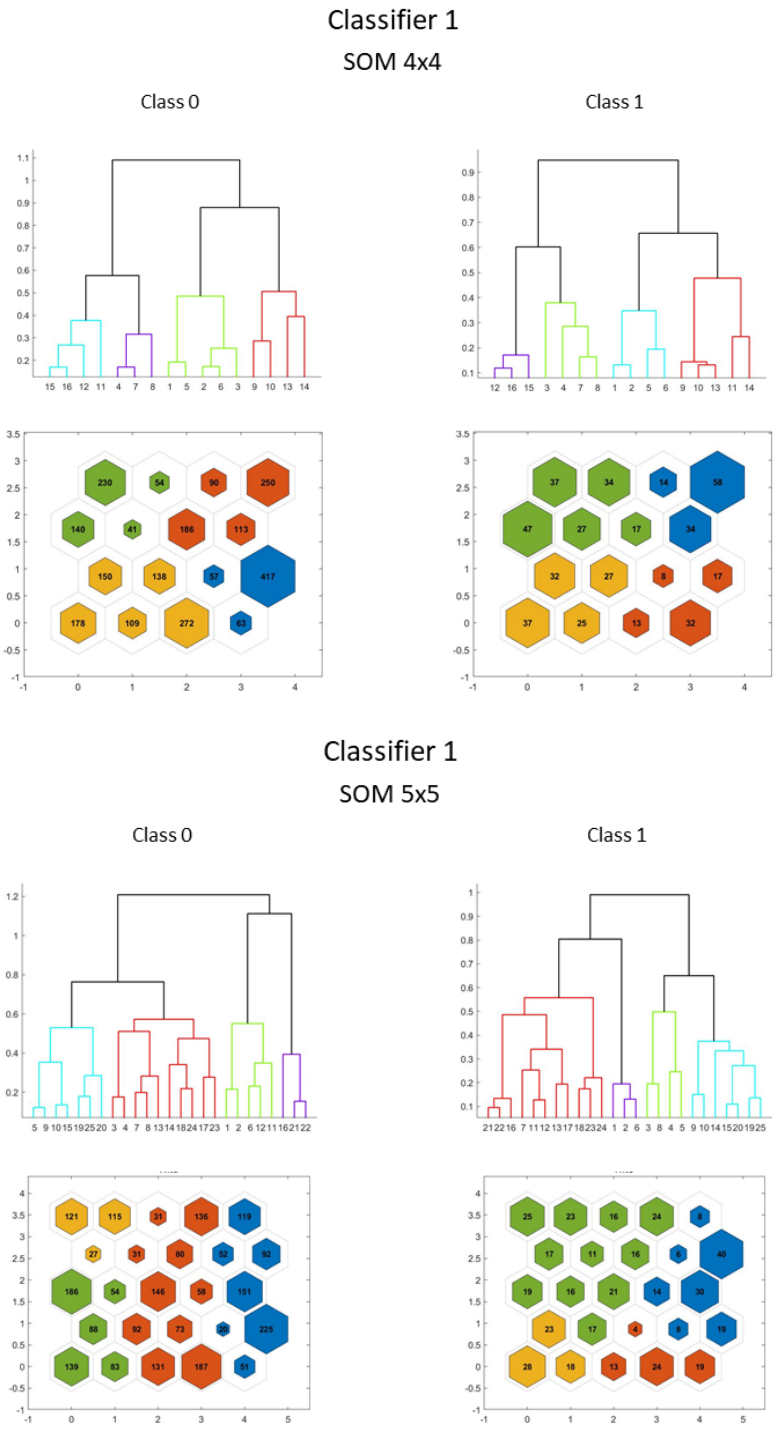

Figure 4.1.4: Dendrograms and clusters of neurons of SOM with two different sizes for classifier 1.

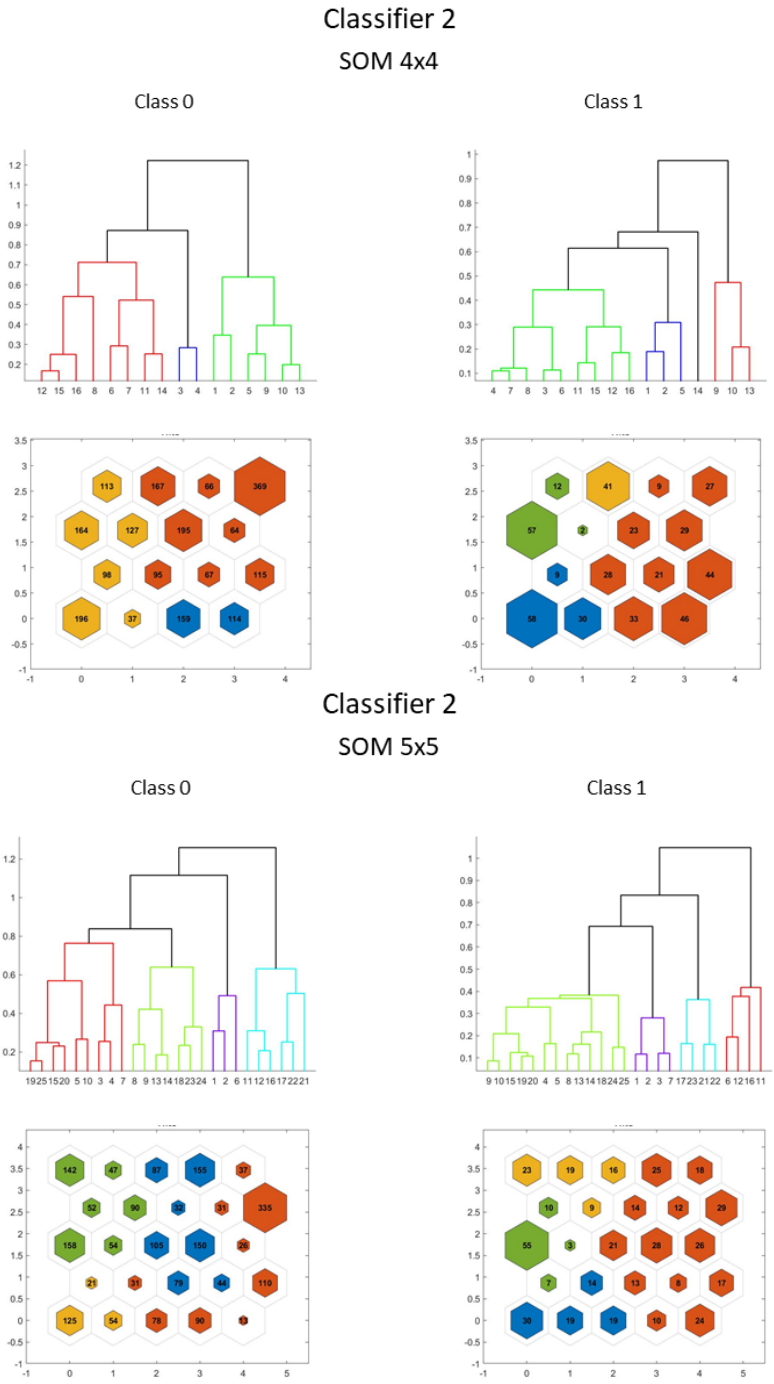

Figure 4.1.5: Dendrograms and clusters of neurons of SOM with two different sizes for classifier 2.

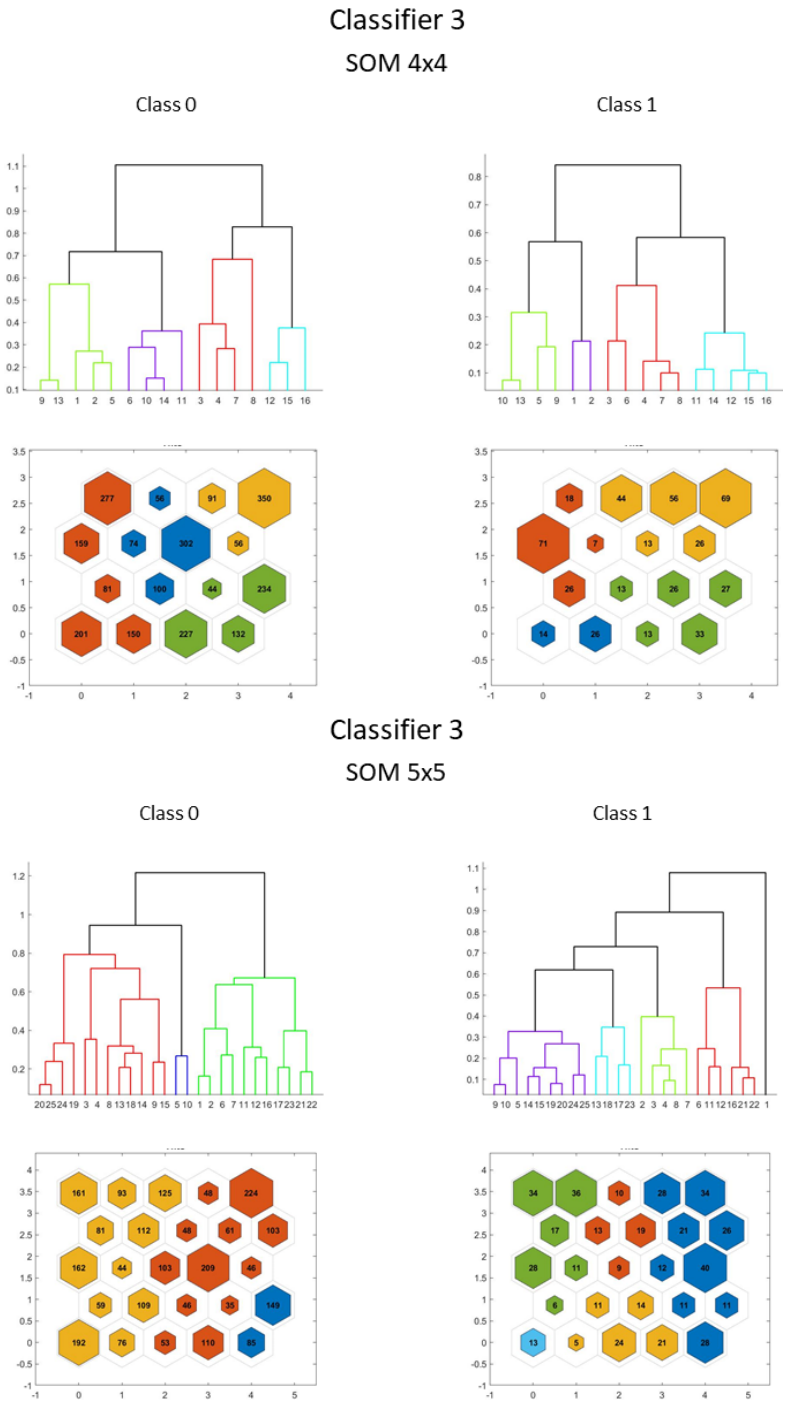

Figure 4.1.6: Dendrograms and clusters of neurons of SOM with two different sizes for classifier 3.

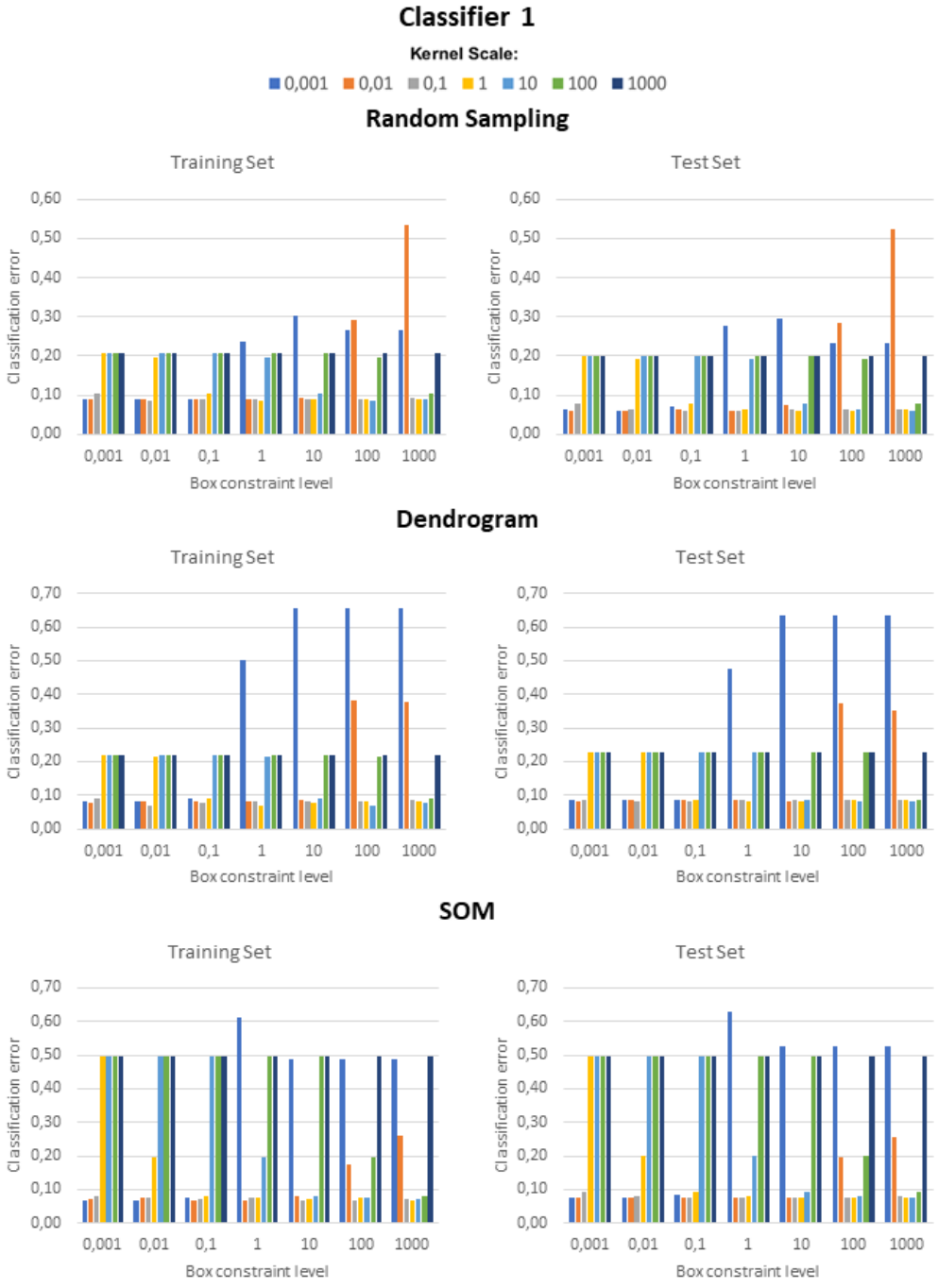

Figure 4.1.7: Classification error plots for the different parameters of the classifier 1. Random sampling, Dendrogram and SOM are the three different methods employed for the training set construction.

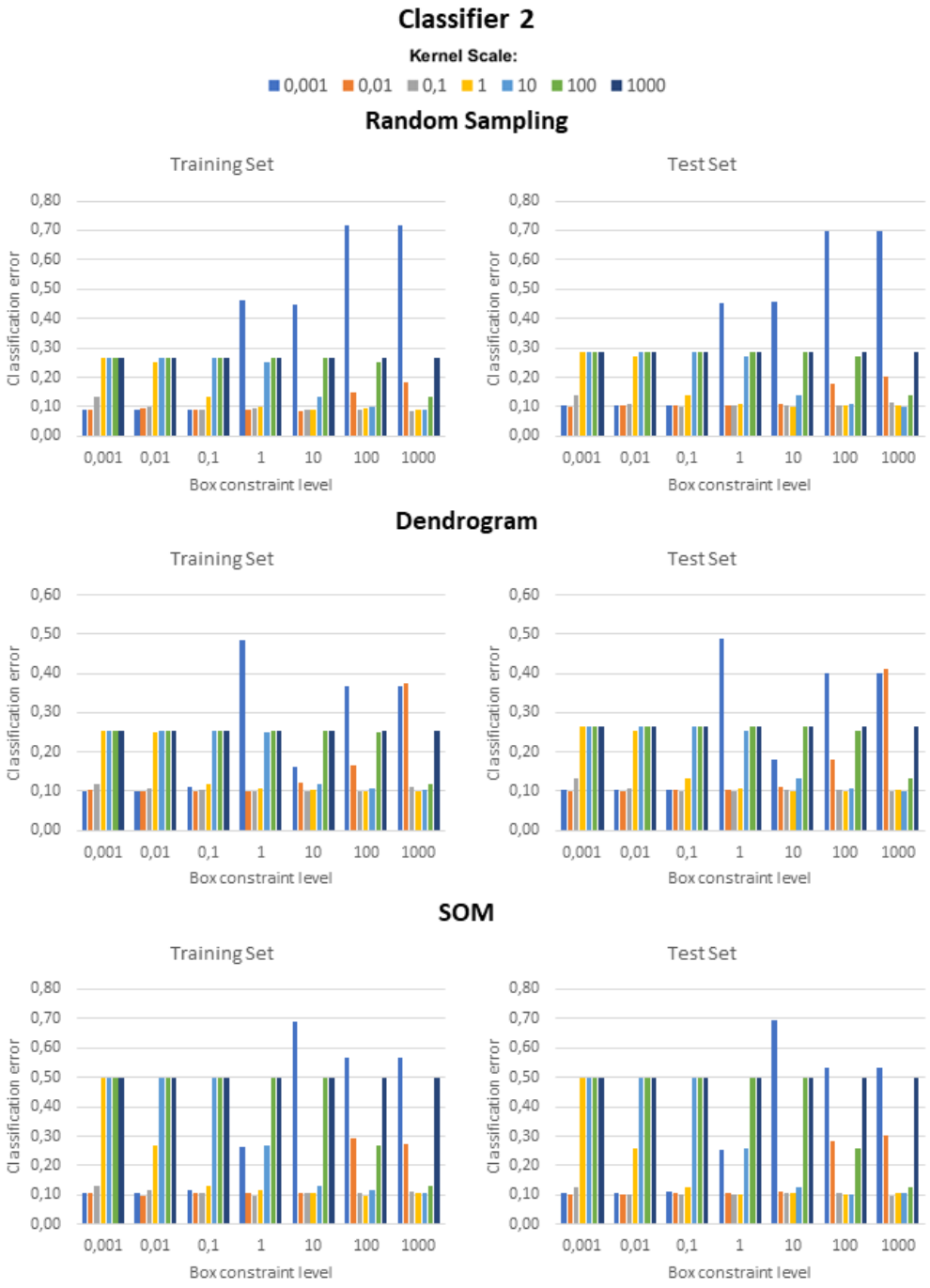

Figure 4.1.8: Classification error plots for the different parameters of the classifier 2. Random sampling, Dendrogram and SOM are the three different methods employed for the training set construction.

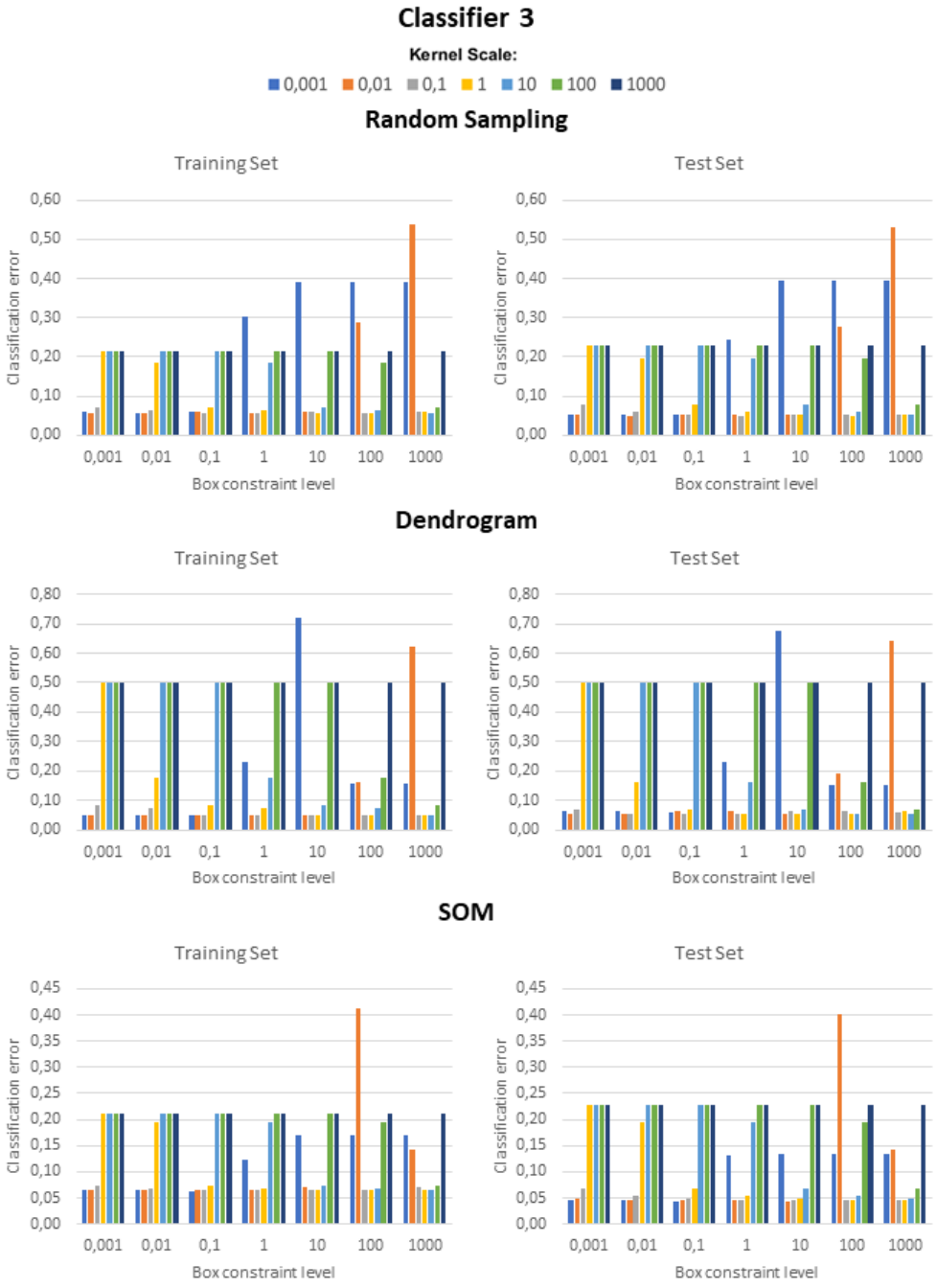

Figure 4.1.9: Classification error plots for the different parameters of the classifier 3. Random sampling, Dendrogram and SOM are the three different methods employed for the training set construction.

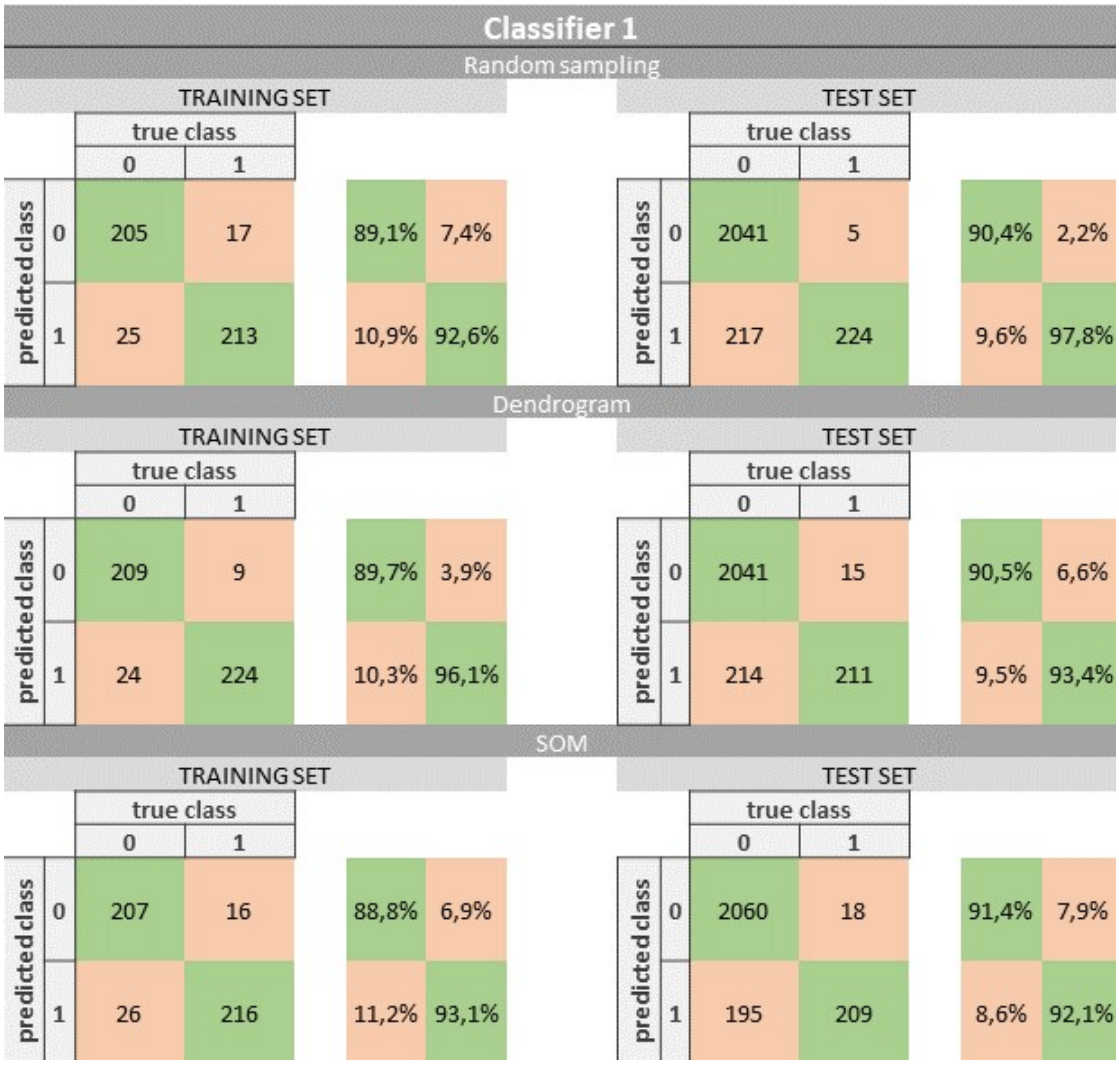

Figure 4.1.10: Confusion matrices of training and test set for classifier 1. The classification performances obtained with the three possible training and test set pairs (random sampling, dendrogram, and SOM) were reported.

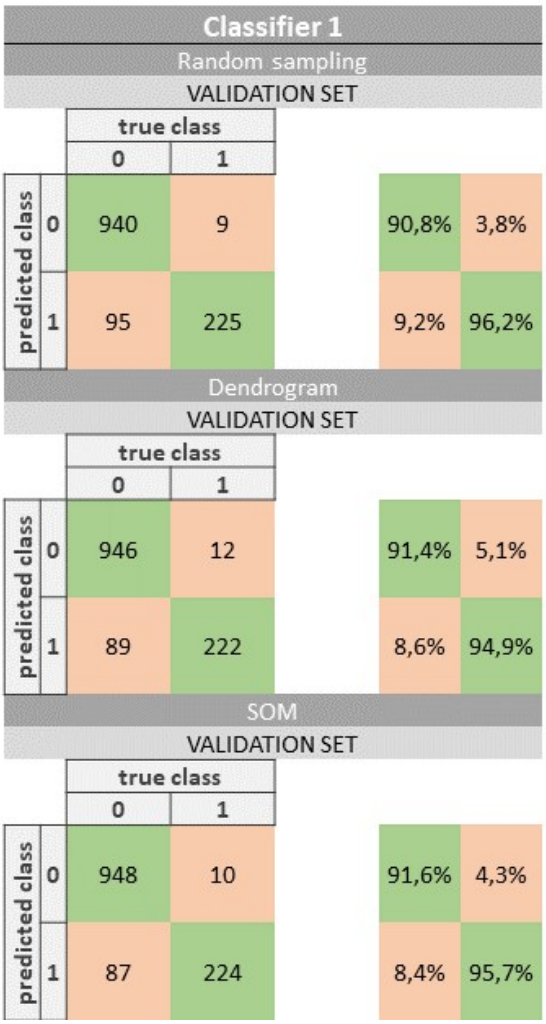

Figure 4.1.11: Confusion matrices of validation set for classifier 1. The classification performances obtained with the three possible training and test set pairs (random sampling, dendrogram, and SOM) were reported.

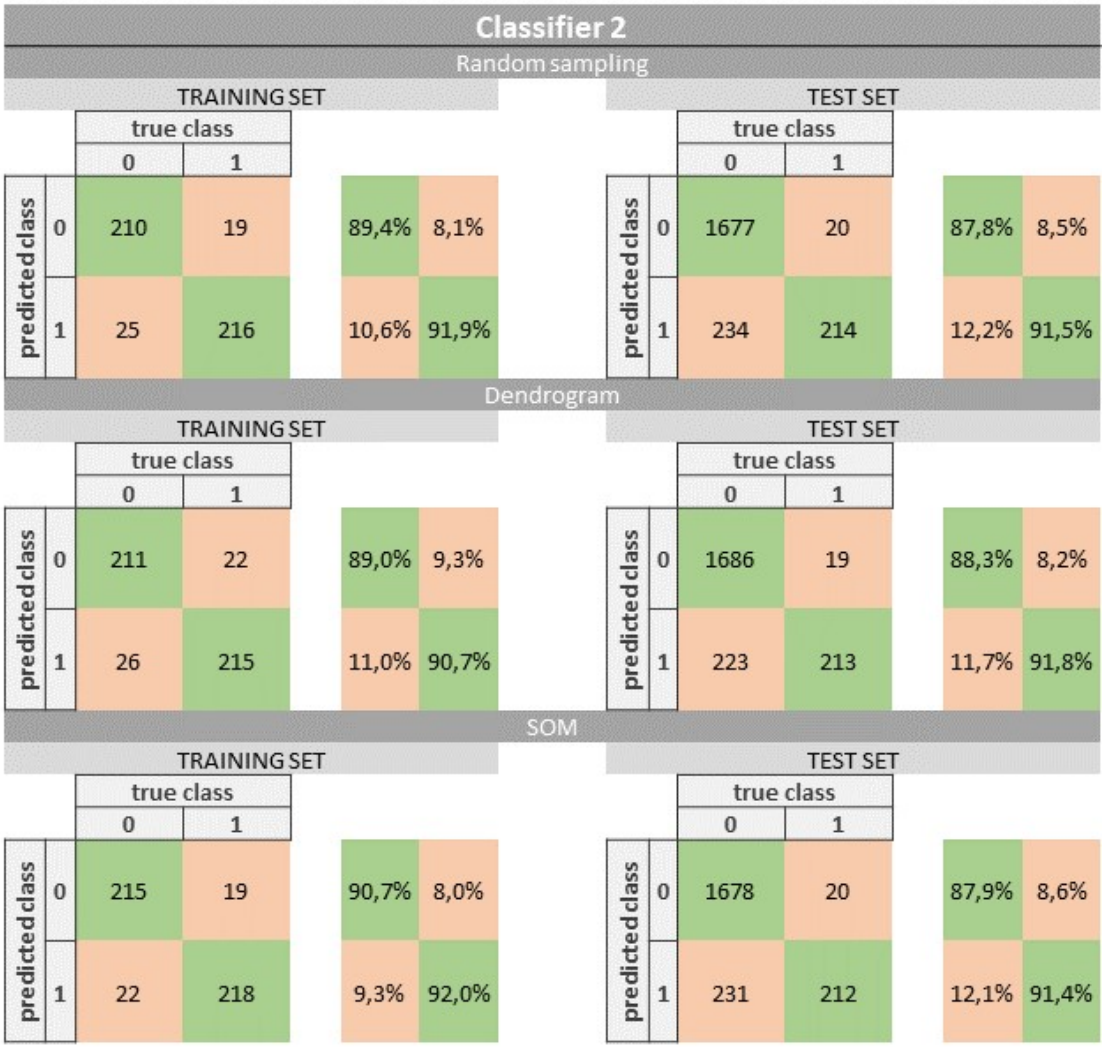

Figure 4.1.12: Confusion matrices of training and test set for classifier 2. The classification performances obtained with the three possible training and test set pairs (random sampling, dendrogram, and SOM) were reported.

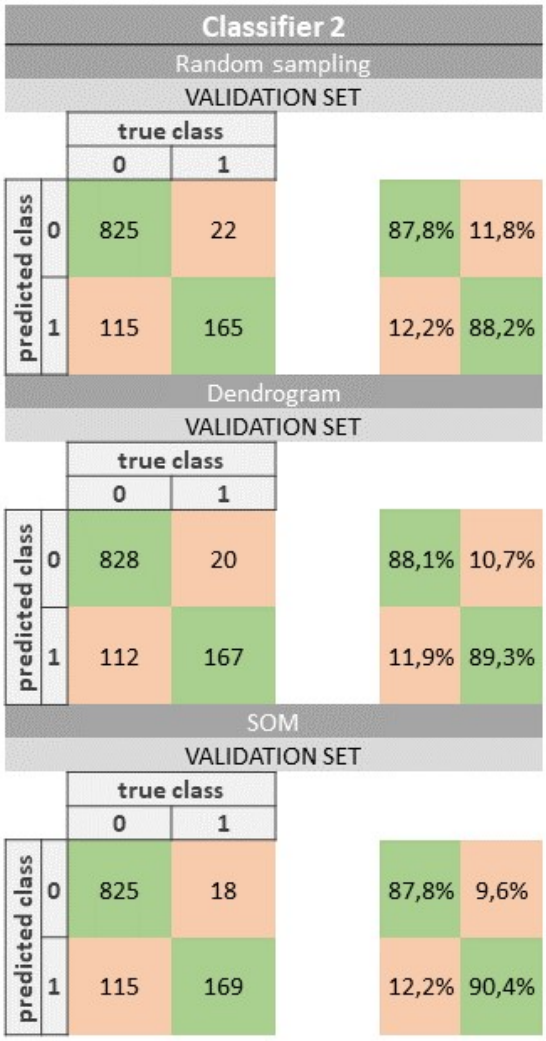

Figure 4.1.13: Confusion matrices of validation set for classifier 2. The classification performances obtained with the three possible training and test set pairs (random sampling, dendrogram, and SOM) were reported.

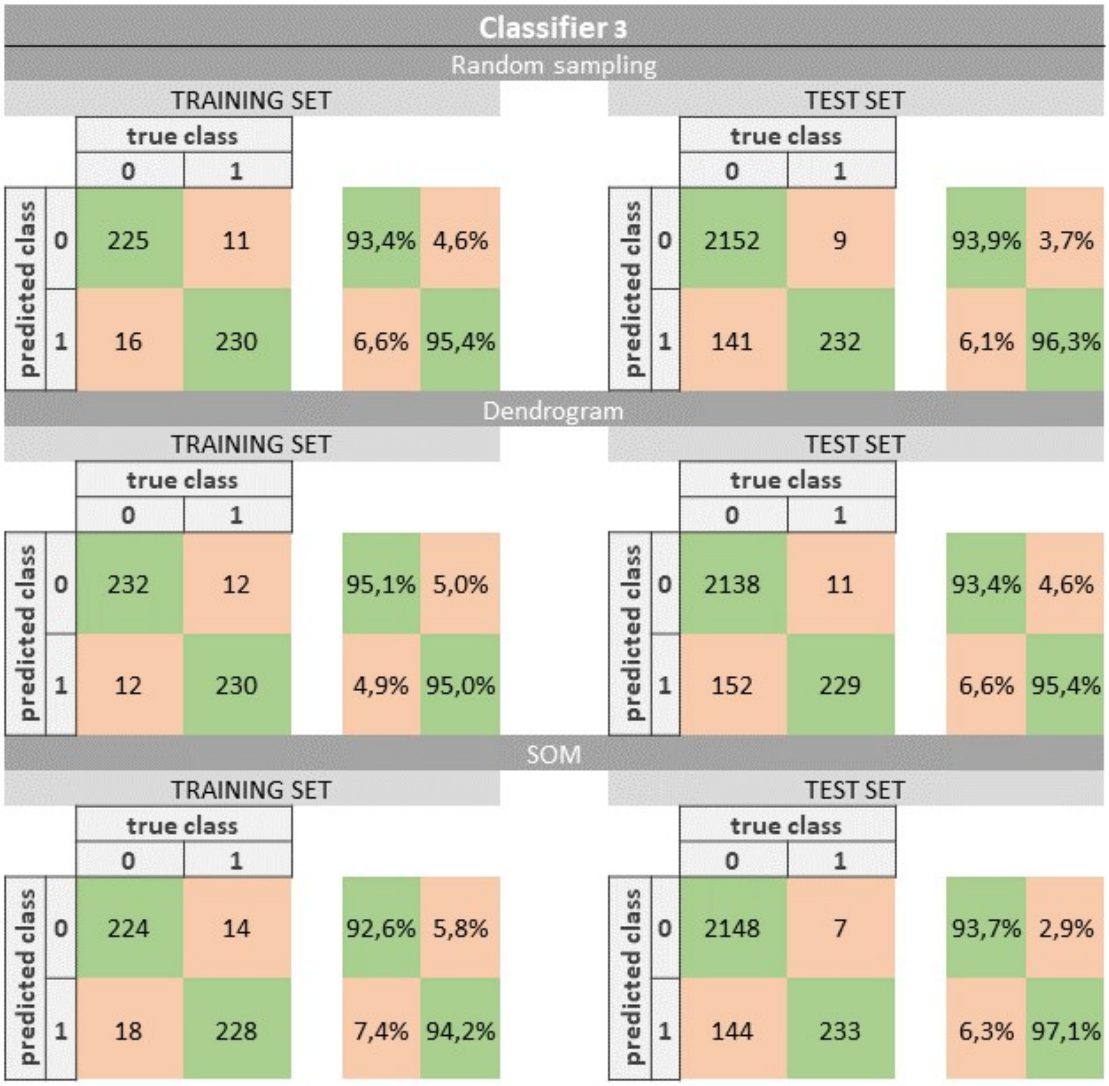

Figure 4.1.14: Confusion matrices of training and test set for classifier 3. The classification performances obtained with the three possible training and test set pairs (random sampling, dendrogram, and SOM) were reported.

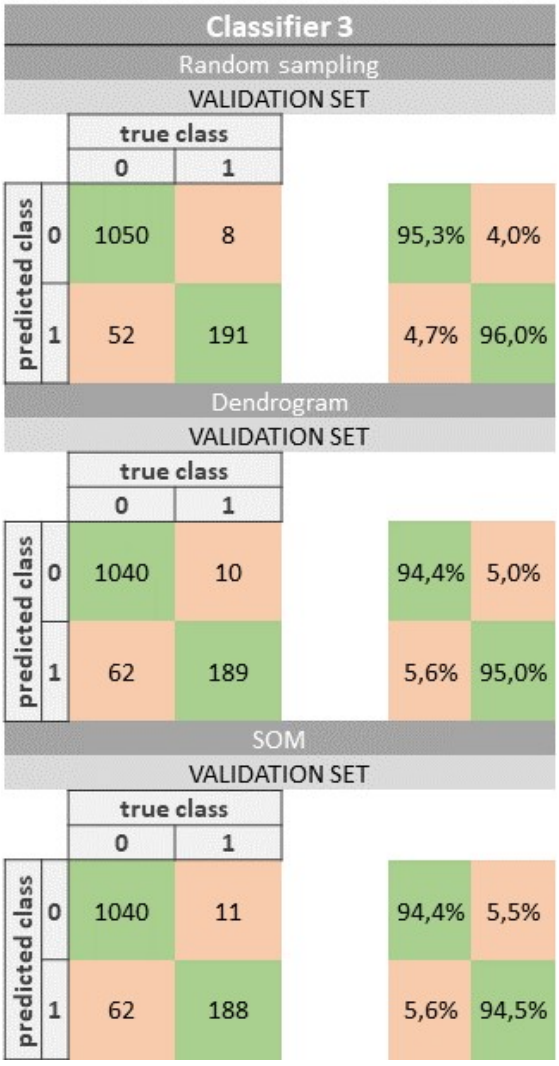

Figure 4.1.15: Confusion matrices of validation set for classifier 3. The classification performances obtained with the three possible training and test set pairs (random sampling, dendrogram, and SOM) were reported.

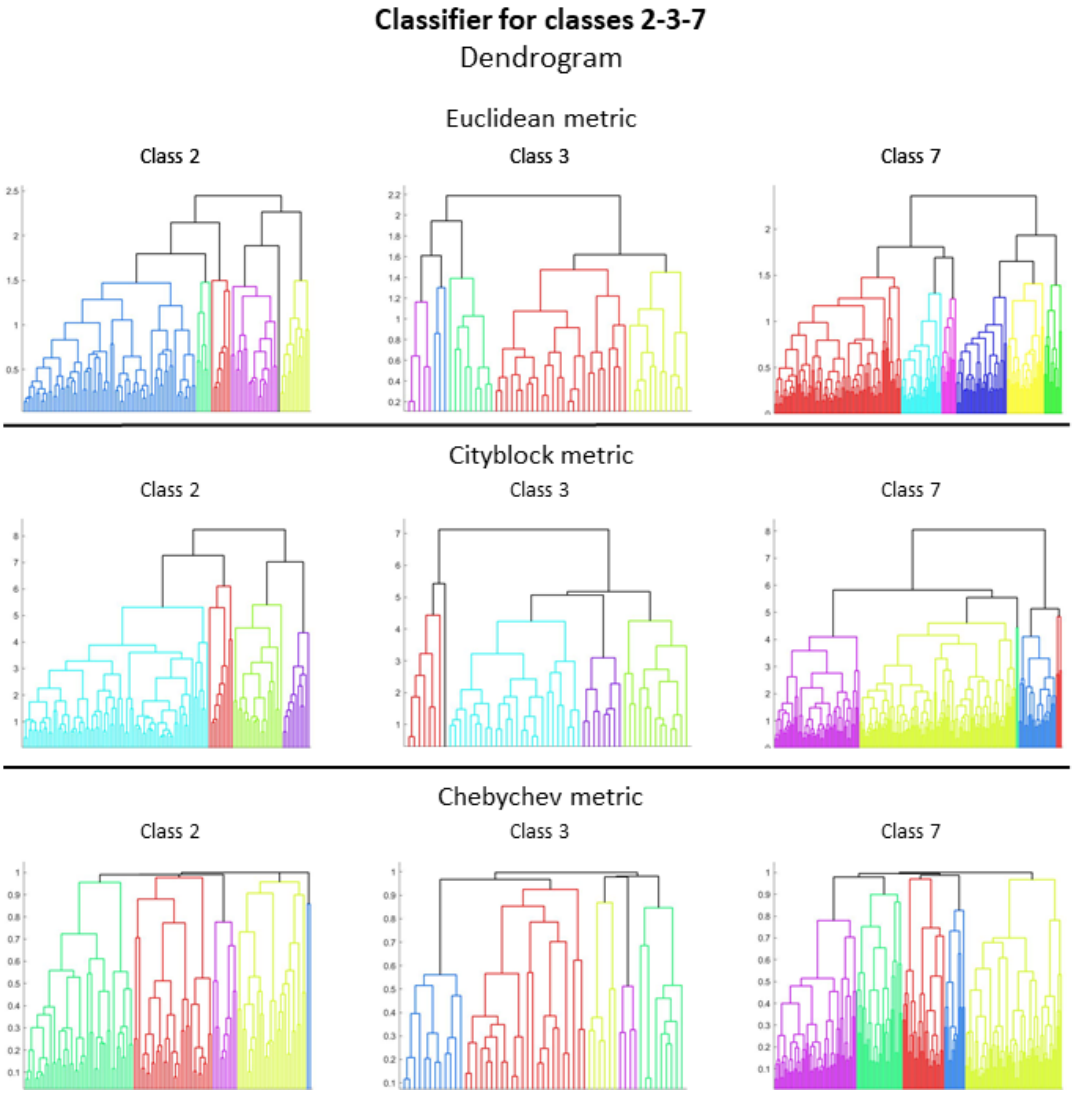

Figure 4.2.1: Dendrograms with three different metrics for classifier 2vs3vs7.

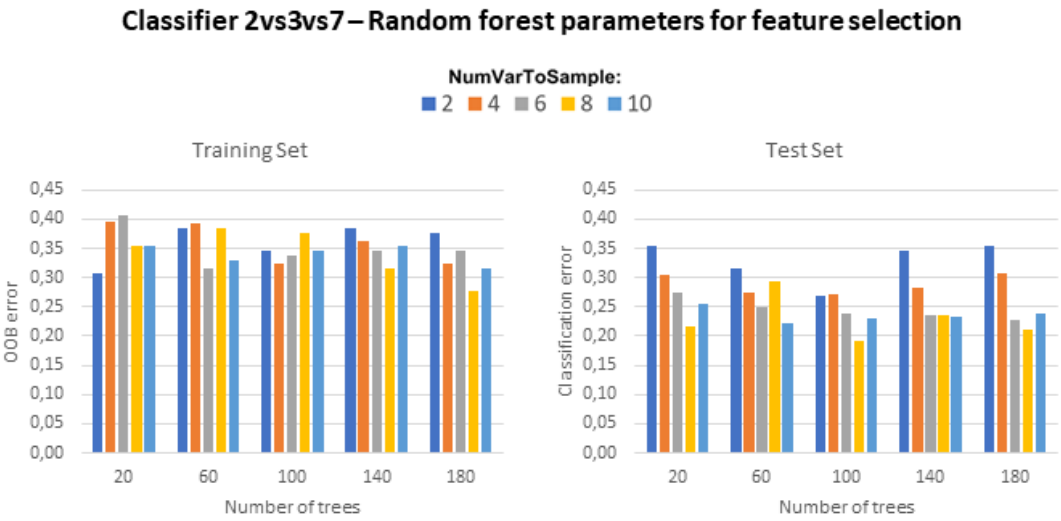

Figure 4.2.2: Classification error plots with different random forest parameter. This classifier was created to select the features for classifier 2vs3vs7. NumVarToSample: number of variables to sample.

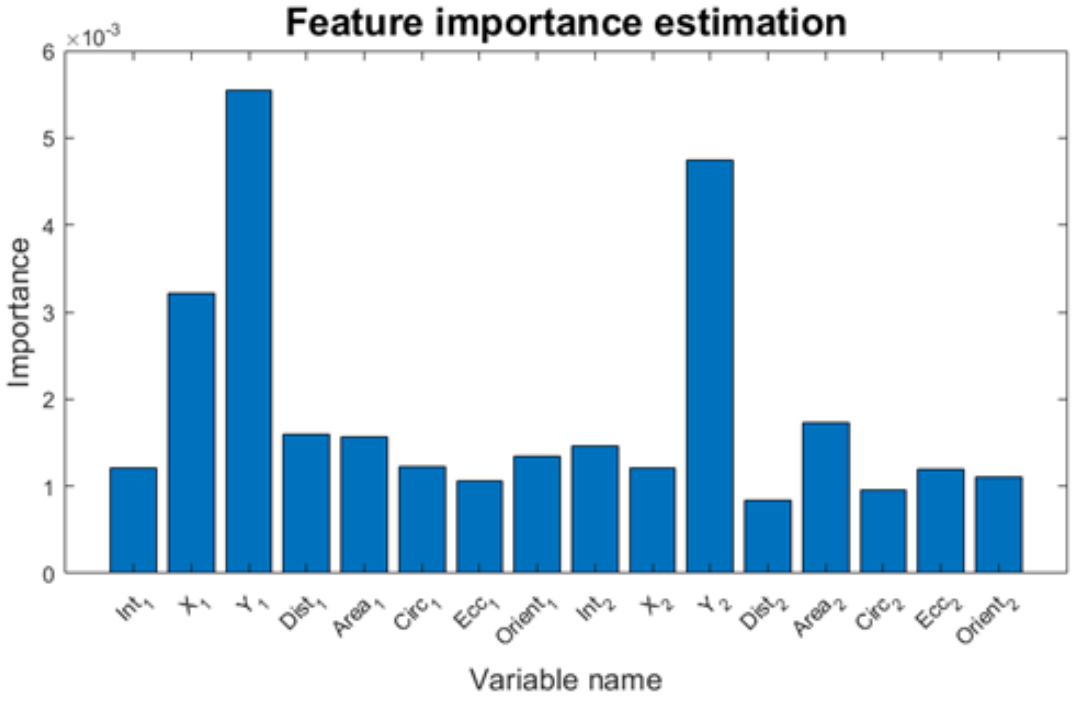

Variable name	Int	X	Y	Dist
Meaning	Peak intensity	Peak x-value	Peak y-value	Peak-to-centroid distance
Variable name	Area	Circ	Ecc	Orient
Meaning	Area of the segmentation	Circularity of the segmentation	Eccentricity of the segmentation	Orientation of the segmentation
1= relative to the front view image; 2=relative to the side view image				

Figure 4.2.3: Feature importance estimation for classifier 2vs3vs7 provided by the optimized random forest classifier.

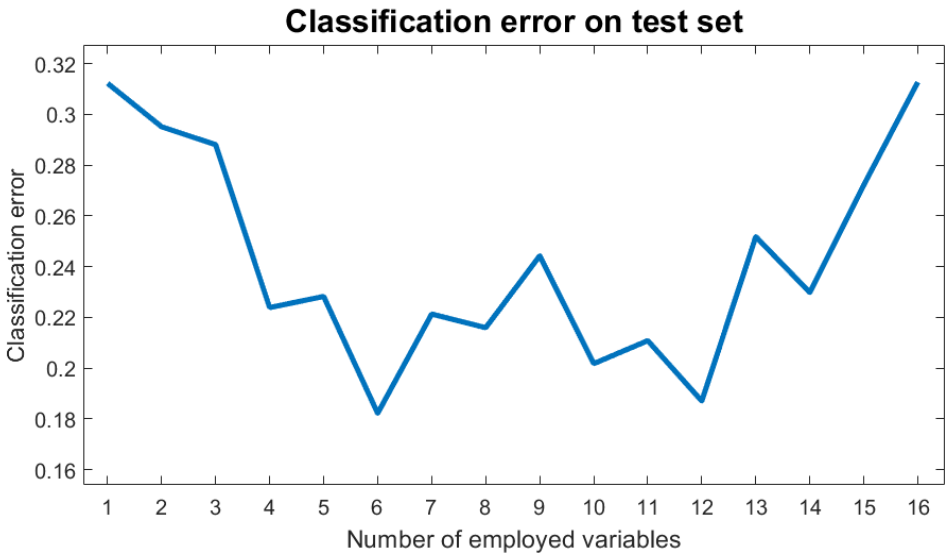

Figure 4.2.4: Classification error trend on test set of the classifier 2vs3vs7, as a function of the number of selected variables.

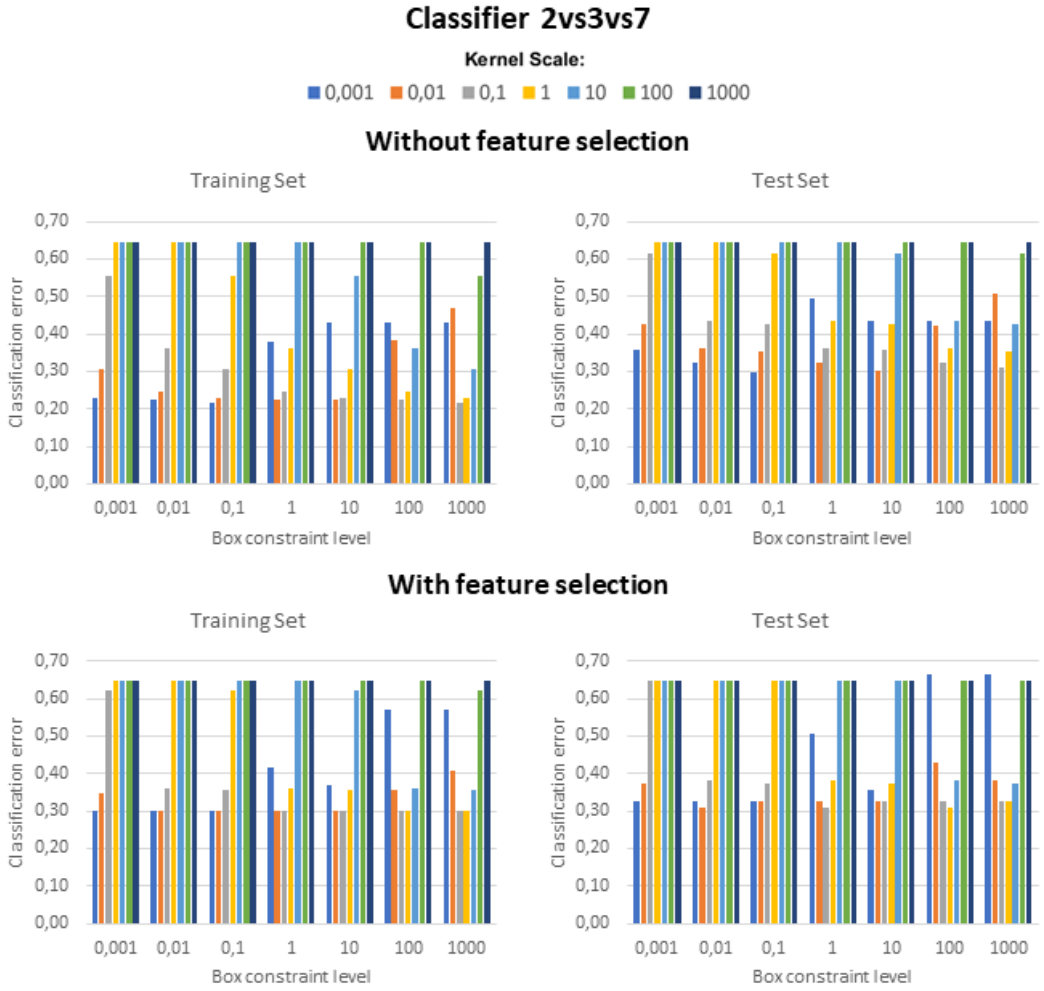

Figure 4.2.5: Classification error plots with different SVM model parameters of the classifier 2vs3vs7. Two SVM models were created, one using all features and the other with only the selected variables.

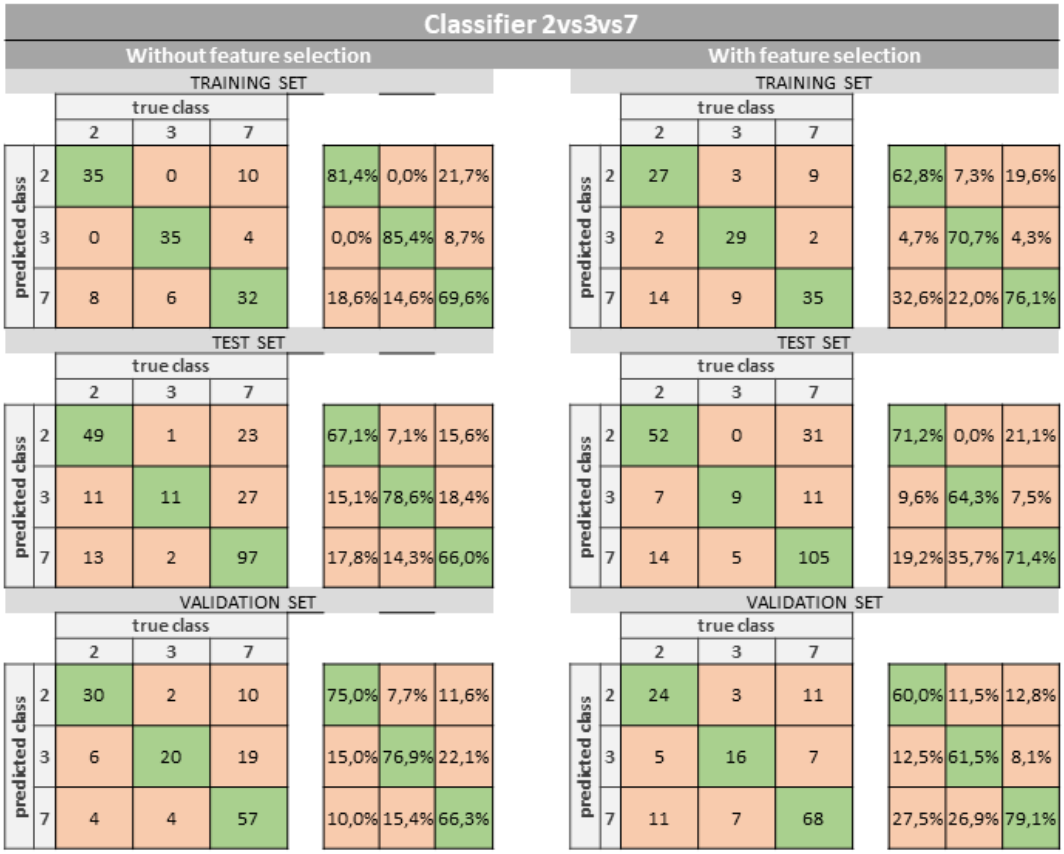

Figure 4.2.6: Classification performances of classifier 2vs3vs7 on training set, test set and validation set. Two SVM models were created, one using all features and the other with only the selected variables.

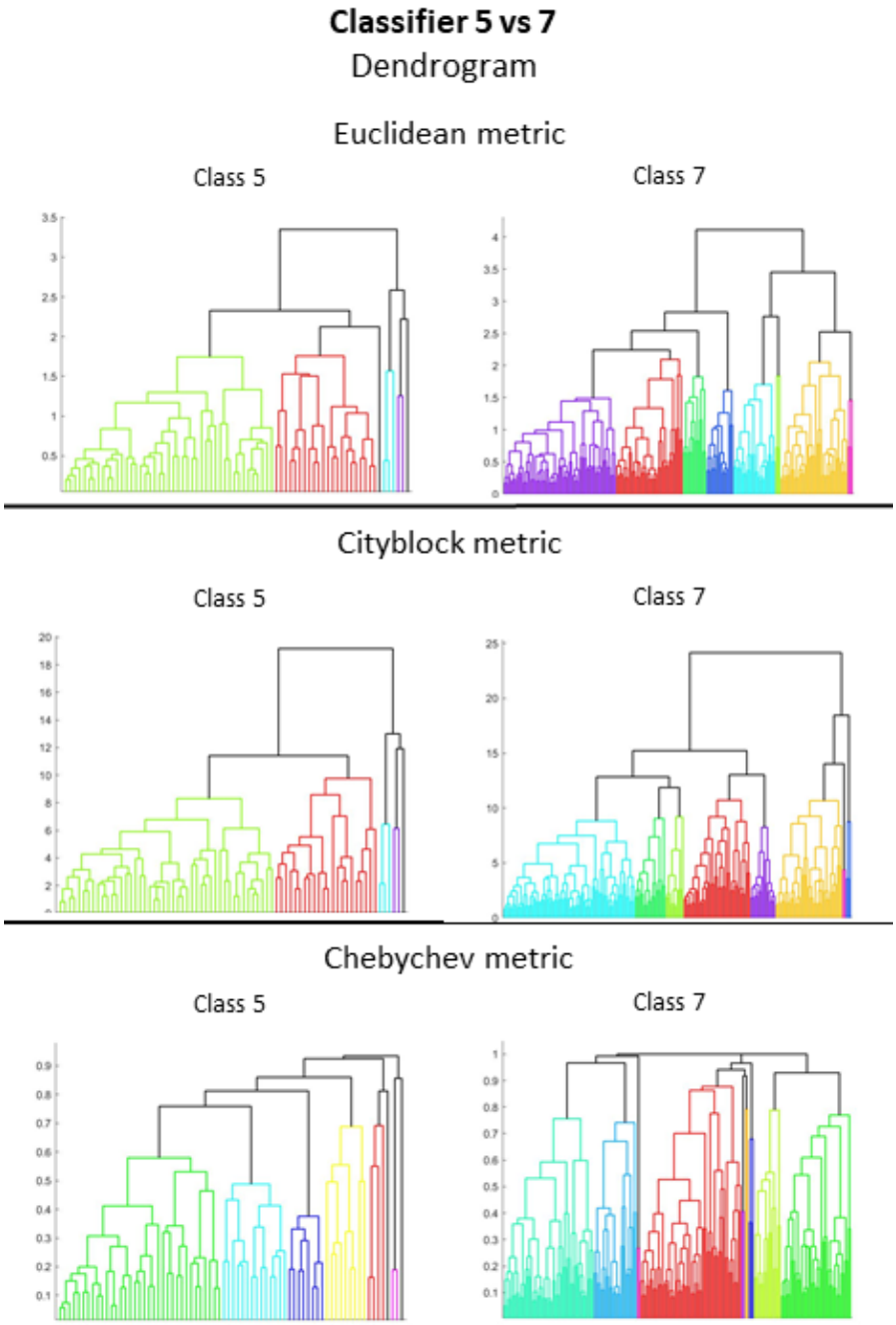

Figure 4.2.7: Dendrograms with three different metrics for classifier 5vs7.

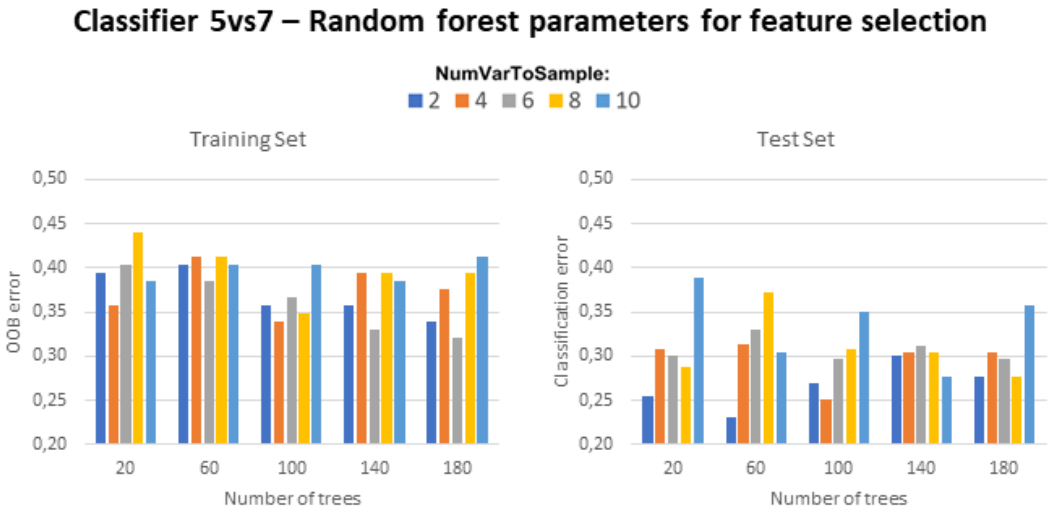

Figure 4.2.8: Classification error plots with different random forest parameter. This classifier was created to select the features for classifier 5vs7. NumVarToSample: number of variables to sample.

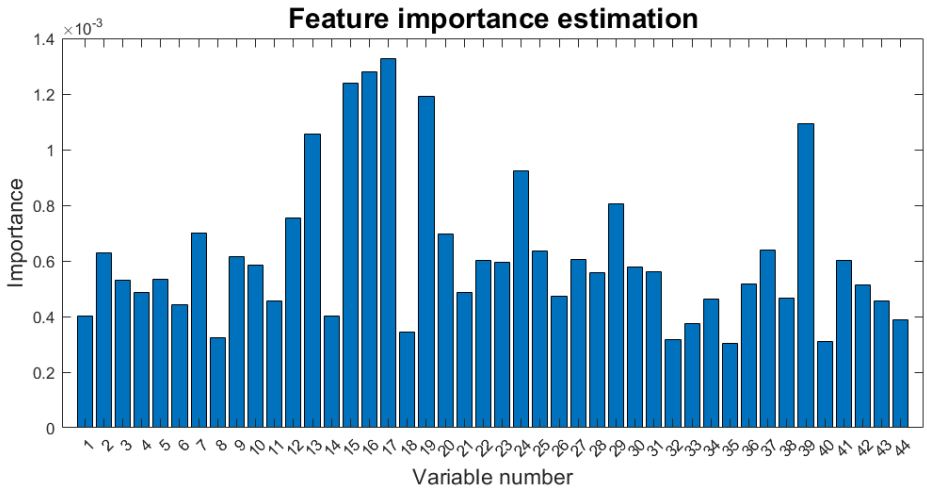

Figure 4.2.9: Feature importance estimation for classifier 5vs7 provided by the optimized random forest classifier.

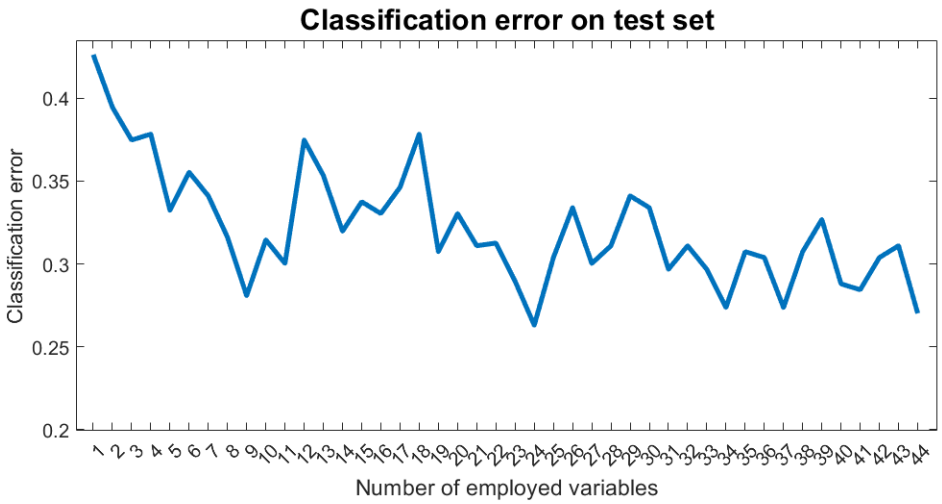

Figure 4.2.10: Classification error trend on test set of the classifier 5vs7, as a function of the number of selected variables.

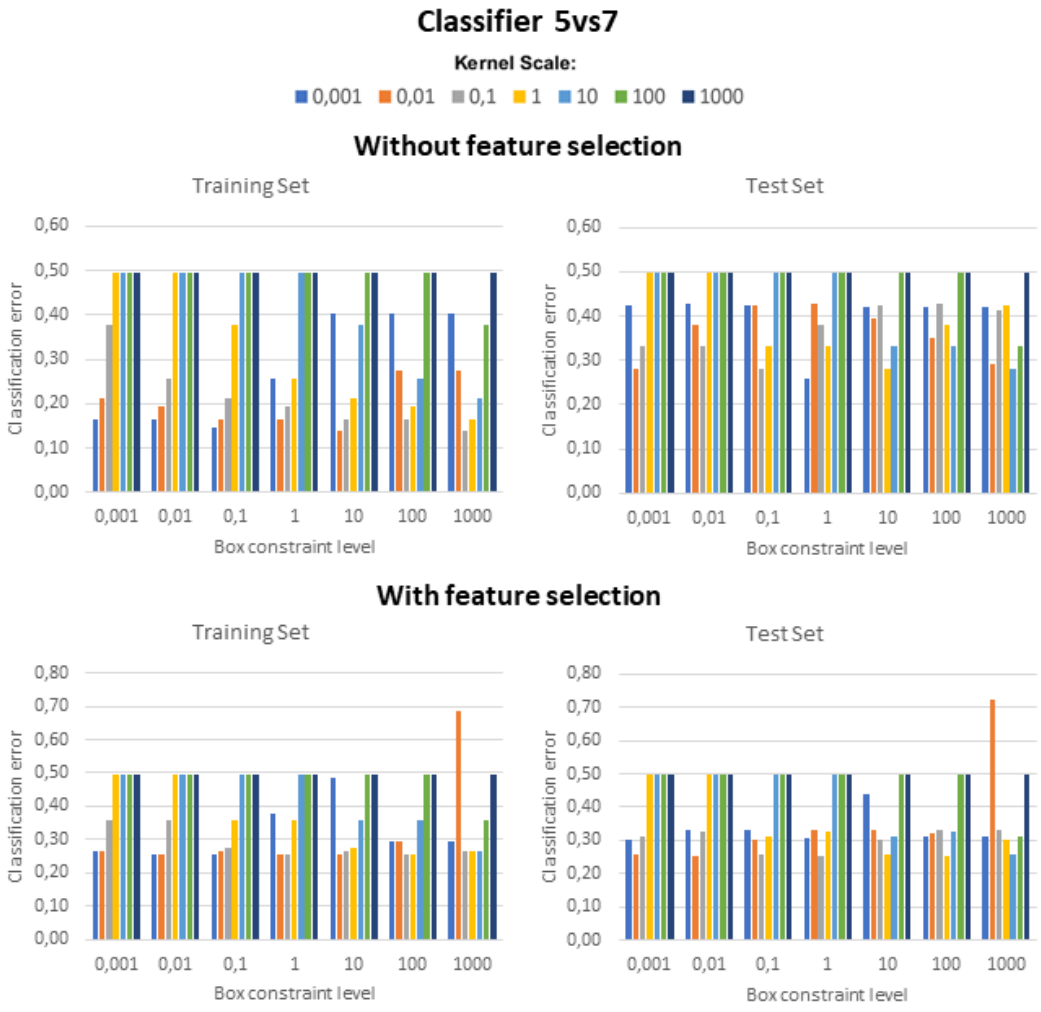

Figure 4.2.11: Classification error plots with different SVM model parameters of the classifier 5vs7. Two SVM models were created, one using all features and the other with only the selected variables.

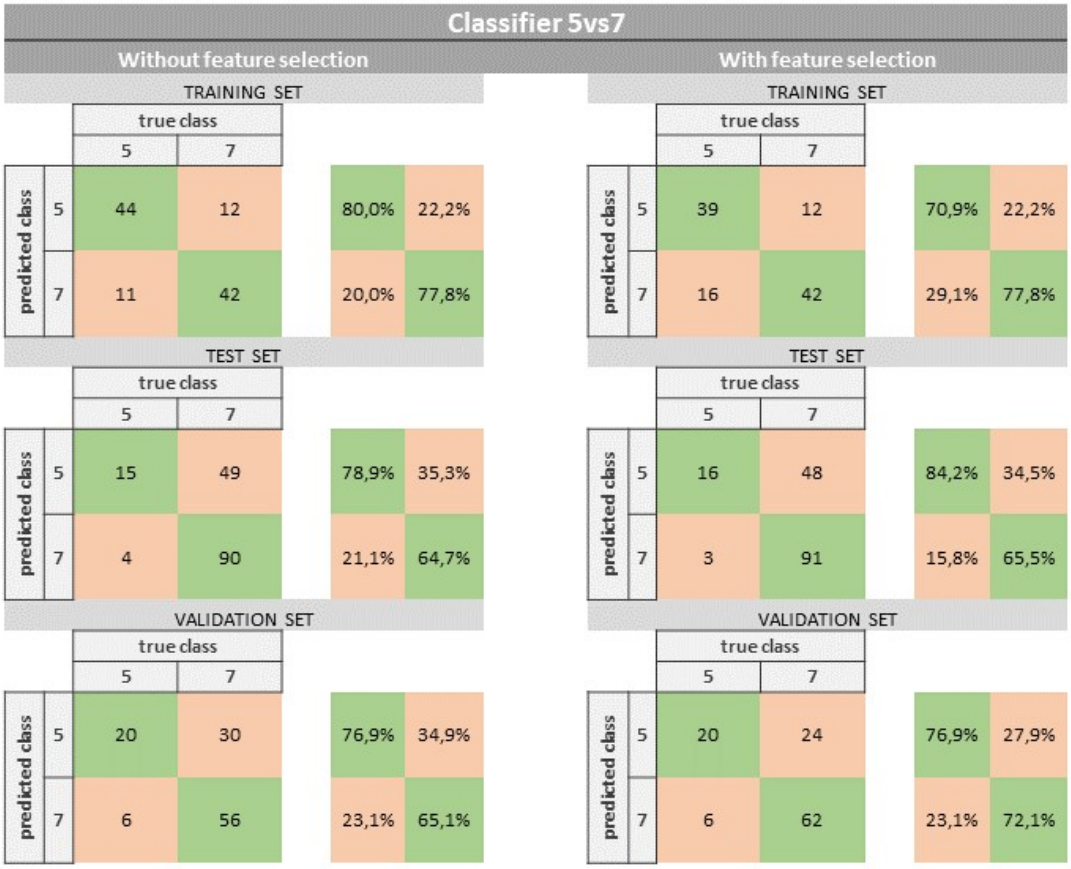

Figure 4.2.12: Classification performances of classifier 5vs7 on training set, test set and validation set. Two SVM models were created, one using all features and the other with only the selected variables.

Chapter 5

Discussions

5.1 Classifier for heart position detection

The different combinations of the SVM classifier parameters provided the classification error plots for the three classifiers (figures 4.1.7, 4.1.8, 4.1.9), which show a great similarity between the classification results obtained on the training set and those obtained on the test set. This aspect suggests that, for all three classifiers, the elements selected for the training set serve as good representatives for the items in the test set, whatever the technique adopted for the training set construction. Although all three classifiers obtained a high percentage of correctly classified elements, classifier 2 performed worse than the other two models on all three datasets (figures 4.1.12, 4.1.13). The reason for this result can be sought by analyzing the features of the data that were utilised for the construction of these models. In particular, figure 5.1.1 shows, for all 3 classifiers, the distribution of the x-values and y-values of the peaks belonging to the validation set. Peaks relative to the heart of the classifier 2 are more scattered than the heart peaks reported for the other classifiers. This characteristic may have negatively affected the classifier 2 performance, making it difficult to identify a hyper-surface which is able to separate the two classes.

5.2 Classifiers for possible centering corrections

5.2.1 Classifier for classes 2, 3, 7

This classifier was created in order to assess if the patient/detector configuration during the examination was correct or if it needed to be changed. In particular, for the upright position, the goal was to check whether the patient chair was in the right position (class 7) or if it was necessary to raise or lower it (class 2 and 3

respectively). For the supine configuration, the issue concerned the assessment of the detector head position, which could be moved towards the patient's feet (class 2) or towards the patient's head (class 3).
Previously it was underlined that on average:

- images belonging to class 2 showed the peak relative to the heart with a lower y-value;
- pre-scans in class 3 reported the heart peak in a higher position;
- class 7 acquisitions presented the heart region at an intermediate height compared to the other two classes.

These factors strongly influenced the classification of these elements. Indeed, the feature importance estimation reported in figure 4.2.3 shows that peak y-values of the front and side view images are the two most important variables.
The performances reported in figure 4.2.6 indicate that the developed classifier failed to evaluate the right class for some elements. This result may be explained considering the distribution of the peak y-values of pre-scans belonging to the three different classes under consideration (figure 5.2.1). Although most of the peaks show characteristics consistent with expectations, some elements present values which do not fall within the range typical of their class.
To provide an example, the front view and side view images reported in figure 5.2.2 were labelled as belonging to class 2, even if the region related to the heart is located in a high position, where class 3 peaks should be placed.
The classification of this kind of pre-scans certainly led to a deterioration in performance, as the classifier was trained on elements which show different characteristics.

5.2.2 Classifier for classes 5 and 7

This classifier was developed in order to discern between two other classes: acquisitions with a too high extra-cardiac activity and images which do not need any corrections (class 5 and 7, respectively). For class 5 elements, it is suggested to make the patient drink cold water.
22 statistical features were extracted from the segmented area relative to the heart, in order to identify possible differences between the two classes. These variables were obtained from the front and top view images, since on average these views showed less marked heart region boundaries for class 5 pre-scans. Some of these features played a more prominent role in the classification problem, as indicated by the feature importance estimation reported in figure 4.2.9. In particular, the information measure of correlation and the homogeneity calculated from the heart region in the front view image resulted the two most important features.

Figure 4.2.6 shows that the constructed model reached good performance, even if some elements were not predicted successfully by the classifier. In order to understand the differences between correctly classified pre-scans and misclassified ones, three scatter plots (one for each set) show information measure of correlation (Inf) and homogeneity (Hom) values for both correct and incorrect predictions (figure 5.2.3). Generally the classifier assigned the class 5 to the acquisitions with a low Inf and a high Hom, whilst elements presenting large values for Inf and small values for Hom were predicted as class 7. Indeed, in the scatter plots incorrect predictions are positioned outside the value ranges just described. In the test set the greatest percentage of misclassified acquisitions for class 7 is present: these elements showed features similar to the class 5 pre-scans and so the constructed model failed to classify them.
The two front view images reported in figure 5.2.4 shows very similar characteristics, but the operators labelled the first as belonging to class 5 and the second as class 7 element. Feature values extracted from these two pre-scans are almost equal (first image: Inf=0.32 and Hom=0.87; second image: Inf=0.32 and Hom=0.85) and classifier prediction was class 5 for both images. The choice to assign two different classes to these two similar images could be motivated as follows: the assessments performed were characterized by inter-operator and intra-operator variability.

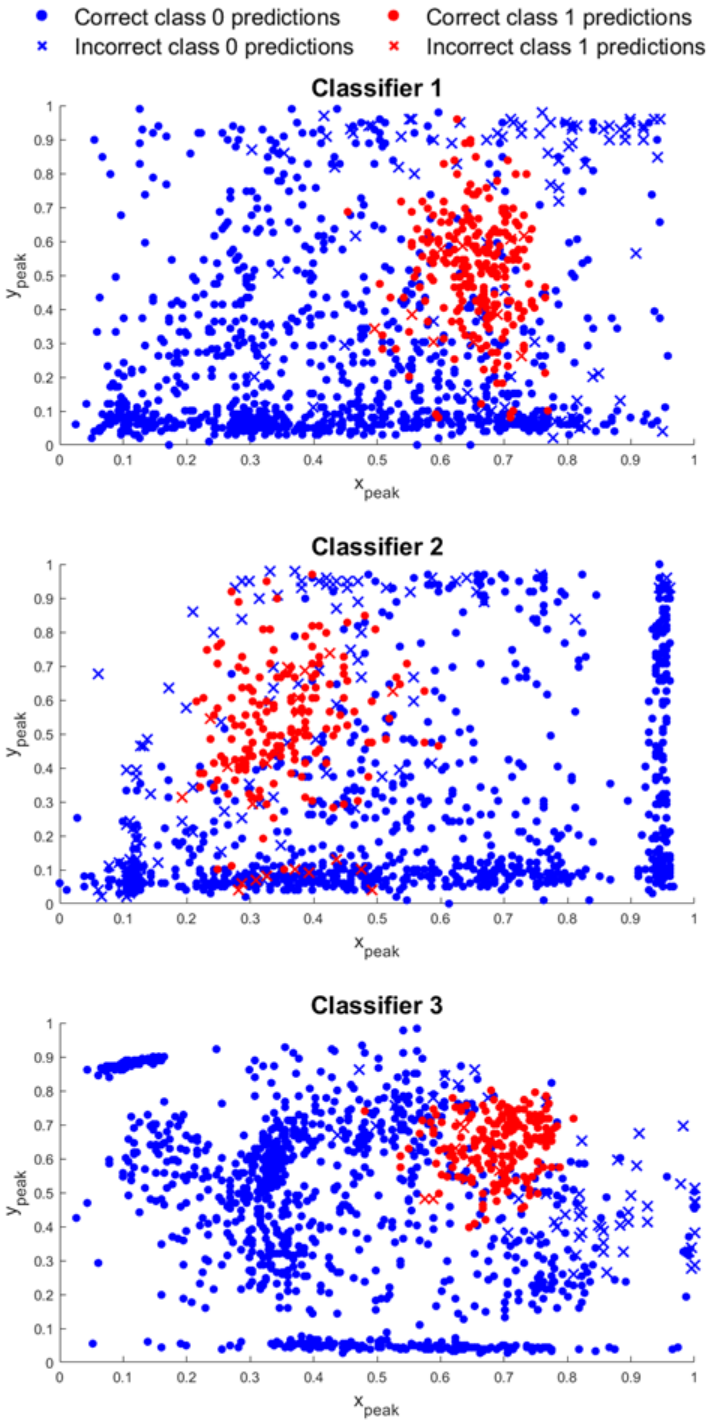

Figure 5.1.1: Scatter plots of the x and y values of the peaks relative to the heart (class 1) and non-relative ones (class 0) for the three classifiers. Correct and incorrect predictions of the three models were distinguished.

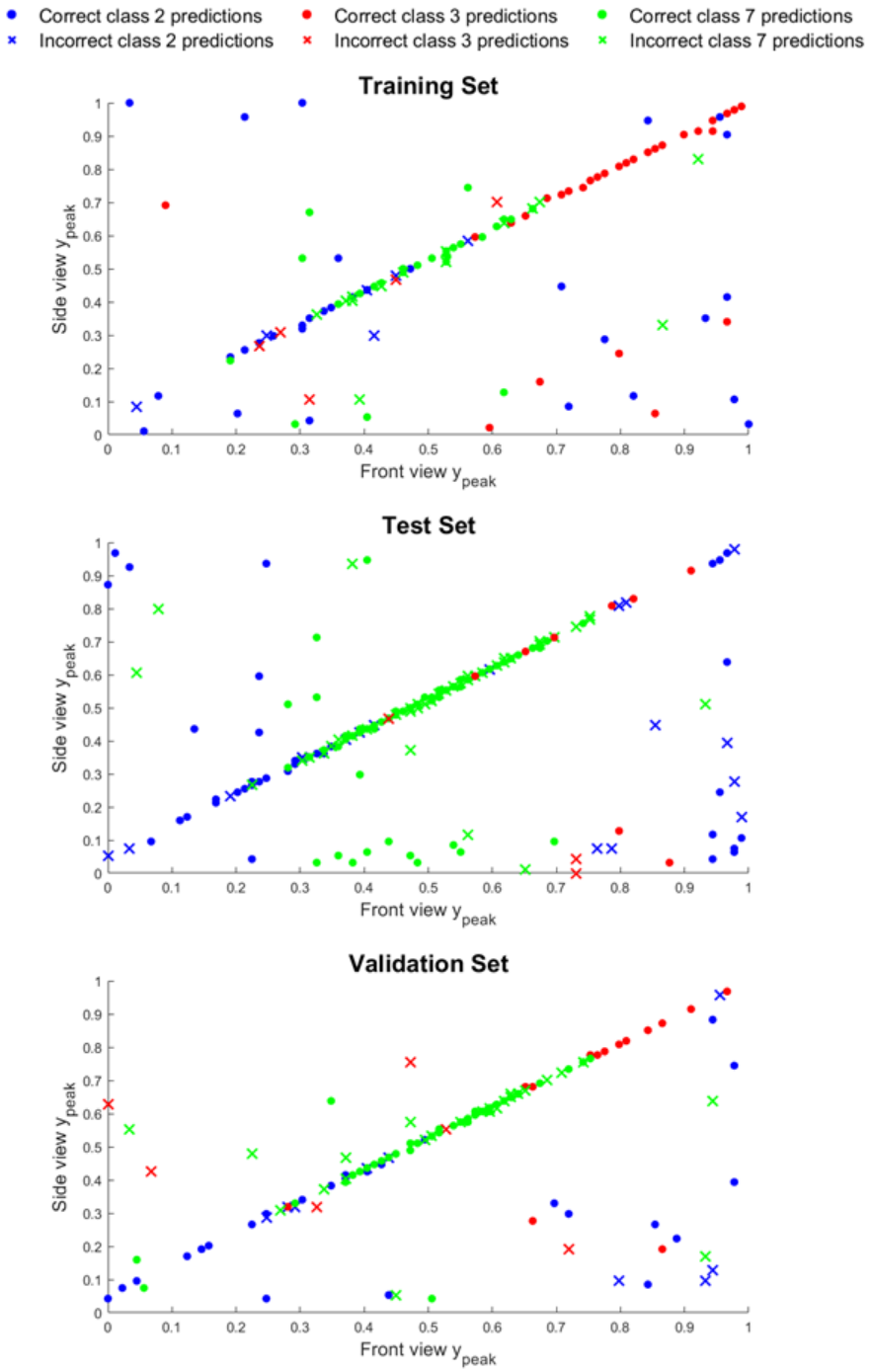

Figure 5.2.1: Scatter plots of the peak y-values of the front and side view images for classifier 2vs3vs7. Correct and incorrect predictions on the three sets were distinguished.

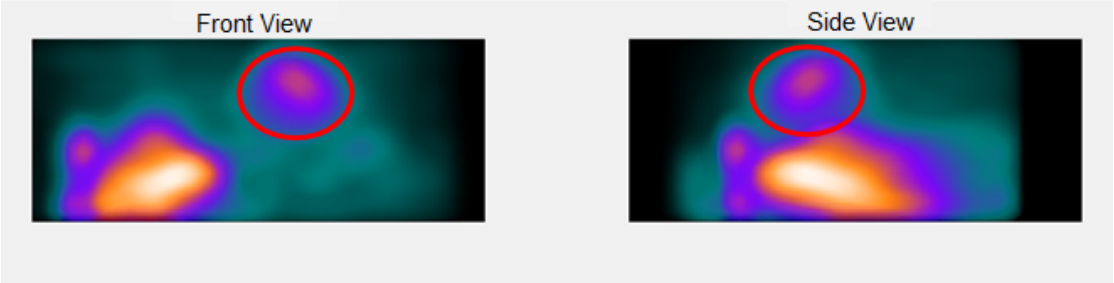

Figure 5.2.2: Example of front and side view images labelled as class 2 but reporting a heart peak with a high y-value, typical of class 3 elements. The red ellipse indicates the region related to the heart.

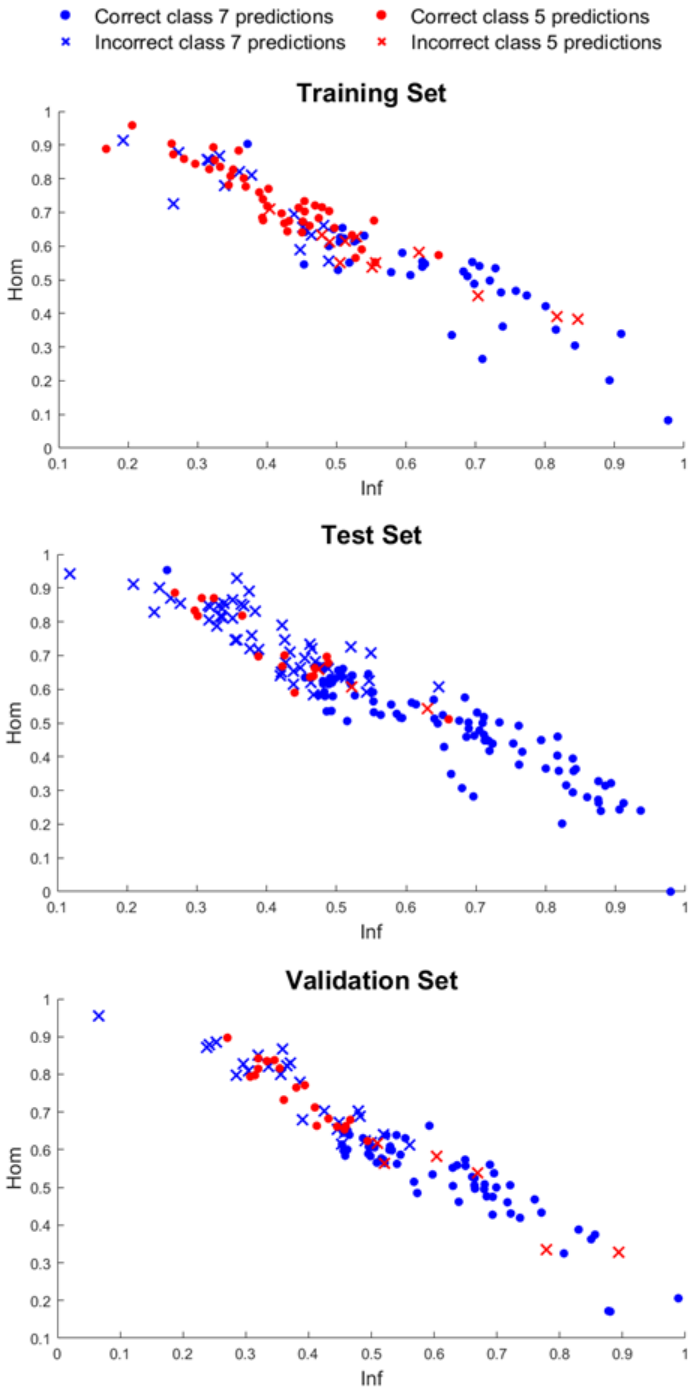

Figure 5.2.3: Scatter plots of information measure of correlation (Inf) and homogeneity (Hom) for classifier 5vs7. Correct and incorrect predictions on the three sets were distinguished.

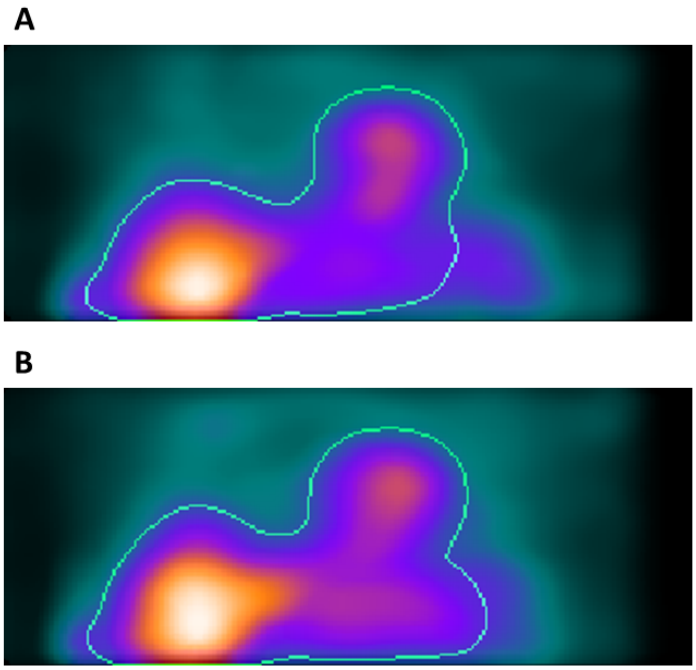

Figure 5.2.4: Example of two front view images for classifier 5vs7. A) This acquisition was labelled as class 5 and the classifier predicted correctly its class. This image showed the following values: Inf=0.32 and Hom=0.87. B) The real class of this acquisition was 7 while the predicted class was 5. It reported the following values: Inf=0.32 and Hom=0.85. Green pixels indicate the boundaries of the segmented region on which the feature calculations were performed. Inf: information measure of correlation. Hom: homogeneity.

Chapter 6

Conclusions

This work was aimed at developing artificial intelligence algorithms to facilitate cardiac SPECT examination, providing the operator with indications about the patient positioning and the heart location in the preliminary scan.

A graphical user interface (GUI) was developed in order to collect data: 711 scans related to 158 different patients were acquired using a D-SPECT system. For each preliminary scan, experts indicated the heart position and possible corrections to the patient-detector configuration. Specifically, the technicians denoted the pre-scans for which the head detector or the patient chair are not in the right position. They also labelled the acquisitions which presented a great extra-cardiac activity, suggesting the patient to drink cold water.

Support vector machine (SVM) models were trained by using the collected information. To detect the heart position in the three pre-scan images, three classifiers were developed. On the validation set sensitivity values from 89.3% to 96% were obtained, while specificity ranged from 88.1% to 95.3%.

Two other classifiers were developed to support the operator in the positioning of the patient and of the detector head. The first classifier had the goal of distinguishing among three different pre-scan categories: raise the chair, lower the chair or leave the chair as it is for the semi-upright position; for the supine configuration, move the detector head towards the patient's feet, towards the patient's head or leave the detector head as it is. This model reached an accuracy of 70.4% on the validation set. The second classifier was created to discern between two other classes: make the patient drink or not drink cold water, depending on the external activity. An accuracy of 73.2% was obtained by this algorithm.

Some aspects of this work could be improved by future developments. First of all, the models constructed to indicate possible corrections during the cardiac SPECT examination failed to classify some elements. This defect could be solved by employing different procedures:

- A data cleaning process may identify the elements which present characteristics that are inconsistent with those of the membership class. Removing this data could lead to improved performance of the classifiers.
- Feature selection should be performed with more accurate methods, which can consider several feature combinations. A ranking method may exclude some variables that are actually informative only when used in conjunction with others.
- Classifier parameters could be optimized according to the selected features by automatic techniques.

Furthermore, it was not possible to develop algorithms to provide some of the possible corrections to the patient-detector configuration (such as suggesting to change the detector head inclination) as not enough data was collected. In the future new images could be acquired in order to obtain other representative elements of these categories. Finally, the future perspective is to implement the optimized classifiers within a software that assists the clinical activity during this diagnostic test.
In conclusion, this was the first time for the company Tecnologie Avanzate that artificial intelligence algorithms were employed to create a support system for cardiac SPECT examinations. Even if the developed classifiers did not achieve optimal results, they are surely a good starting point to make the diagnostic work easier for the operators.

Bibliography

[1] M. Al Moudi, Z. Sun, and N. Lenzo. "Diagnostic Value of SPECT, PET and PET/CT in the Diagnosis of Coronary Artery Disease: A Systematic Review". In: *Biomedical Imaging and Intervention Journal* 7.2 (Apr. 1, 2011), e9. ISSN: 1823-5530. DOI: 10.2349/biij.7.2.e9. pmid: 22287989. URL: https://www.ncbi.nlm.nih.gov/pmc/articles/PMC3265156/.

[2] Rayjanah Allie et al. "Pitfalls and artifacts using the D-SPECT dedicated cardiac camera". In: *Journal of nuclear cardiology : official publication of the American Society of Nuclear Cardiology* 23 (Sept. 2015). DOI: 10.1007/s12350-015-0277-2.

[3] G. P. Aurigemma. "Diastolic heart failure - A common and lethal condition by any name". In: *New England Journal of Medicine* 355.3 (2006), pp. 308–310. DOI: 10.1056/NEJMe068128.

[4] Tomasz Bednarski et al. "Calibration of photomultipliers gain used in the J-PET detector". In: *Bio-Algorithms and Med-Systems* 10 (Dec. 2013). DOI: 10.1515/bams-2013-0110.

[5] S. Ben-Haim et al. "Clinical value of supine and upright myocardial perfusion imaging in obese patients using the D-SPECT camera". In: *Nuclear Cardiology* 21.3 (June 2014), pp. 478–485. DOI: 10.1007/s12350-014-9853-0.

[6] Simona Ben-Haim, John Kennedy, and Zohar Keidar. "Novel Cadmium Zinc Telluride Devices for Myocardial Perfusion Imaging—Technological Aspects and Clinical Applications". In: *Seminars in Nuclear Medicine* 46 (July 2016), pp. 273–285. DOI: 10.1053/j.semnuclmed.2016.01.002.

[7] J. P. Bourdarias. "Coronary reserve: concept and physiological variations". In: *European Heart Journal* 16 (Aug. 1995). DOI: 10.1093/eurheartj/16.suppl_i.2.

[8] Penelope Bouziotis et al. "Radiolabeled iron oxide nanoparticles as dual-modality SPECT/MRI and PET/MRI agents". In: *Current topics in medicinal chemistry* 12 (Jan. 2013). DOI: 10.2174/1568026611212230007.

[9] Jerrold T. Bushberg et al. *The Essential Physics of Medical Imaging*. Vol. 30. 7. Medical Physics, Jan. 2003.

[10] Jerrold T. Bushberg et al. *The essential physics of medical imaging; 3rd ed.* Philadelphia, PA: Lippincott Williams & Wilkins, 2012. URL: https://cds.cern.ch/record/1425946.

[11] M. D. Cerqueira et al. "Standardized myocardial segmentation and nomenclature for tomographic imaging of the heart. A statement for healthcare professionals from the Cardiac Imaging Committee of the Council on Clinical Cardiology of the American Heart Association". In: *Circulation* 105.4 (2002), pp. 539–42. DOI: 10.1161/hc0402.102975.

[12] S. R. Cherry, J. A. Sorenson, and M. E. Phelps. *Physics in Nuclear Medicine*. Elsevier Health Sciences, Jan. 2012. DOI: 10.1016/C2009-0-51635-2.

[13] Ryan A. Dvorak, Richard K. J. Brown, and R. Corbett James. "Interpretation of SPECT/CT myocardial perfusion images: common artifacts and quality control techniques". In: *JRadiographics : a review publication of the Radiological Society of North America* 31.7 (2011), pp. 2041–57. DOI: 10.1148/rg.317115090.

[14] Andrew Einstein et al. "Current worldwide nuclear cardiology practices and radiation exposure: Results from the 65 country IAEA Nuclear Cardiology Protocols Cross-Sectional Study (INCAPS)". In: *European heart journal* 36 (Apr. 2015), pp. 1689–1696. DOI: 10.1093/eurheartj/ehv117.

[15] Kjell Erlandsson et al. "Performance evaluation of D-SPECT: a novel SPECT system for nuclear cardiology". In: *Physics in medicine and biology* 54 (May 2009), pp. 2635–49. DOI: 10.1088/0031-9155/54/9/003.

[16] Shweta Gambhir et al. "A Novel High-Sensitivity Rapid-Acquisition Single-Photon Cardiac Imaging Camera". In: *Journal of nuclear medicine : official publication, Society of Nuclear Medicine* 50 (May 2009), pp. 635–43. DOI: 10.2967/jnumed.108.060020.

[17] Ernest V. Garcia, Tracy L. Faber, and Fabio P. Esteves. "Cardiac Dedicated Ultrafast SPECT Cameras: New Designs and Clinical Implications". In: *Journal of Nuclear Medicine* 52.2 (2011), pp. 210–217. ISSN: 0161-5505. DOI: 10.2967/jnumed.110.081323. eprint: https://jnm.snmjournals.org/content/52/2/210.full.pdf. URL: https://jnm.snmjournals.org/content/52/2/210.

[18] M. L. Geleijnse et al. "Dobutamine stress myocardial perfusion imaging". In: *Journal of the American College of Cardiology* 36.7 (2000), pp. 2017–27. DOI: 10.1016/s0735-1097(00)01012-3.

[19] B. B. Ghoshhajra, R. C. Cury, and R. D. White. *Multimodal Cardiovascular Imaging: Principles and Clinical Applications*. Ed. by O. Pahlm and G. S. Wagner. New York: The McGraw-Hill Companies, Jan. 2011. Chap. 20. Ischemic Heart Disease. ISBN: 9780071613477.

[20] M. W. Groch and W. D. Erwin. "Spect in the year 2000: basic principles". In: *Journal of Nuclear Medicine Technology* 28.4 (2000), pp. 233–244.

[21] Europe PMC Funders Group. "Global, regional, and national age-sex specific all-cause and cause-specific mortality for 240 causes of death, 1990-2013: a systematic analysis for the Global Burden of Disease Study 2013". In: *Lancet* 385.9963 (2015), pp. 117–71. DOI: 10.1016/S0140-6736(14)61682-2.

[22] M. Henzlova et al. "Stress protocols and tracers". In: *Journal of nuclear cardiology : official publication of the American Society of Nuclear Cardiology* 16.6 (2006), e80–90. DOI: 10.1016/j.nuclcard.2006.08.011.

[23] B. Hesse et al. "EANM/ESC guidelines for radionuclide imaging of cardiac function". In: *European journal of nuclear medicine and molecular imaging* 35.4 (Apr. 2008), pp. 851–85. DOI: 10.1007/s00259-007-0694-9.

[24] International Atomic Energy Agency. *Nuclear Cardiology: Guidance on the Implementation of SPECT Myocardial Perfusion Imaging*. 2016. ISBN: 978-92-0-107616-8.

[25] A. S. Iskandrian et al. "Effect of exercise level on the ability of thallium-201 tomographic imaging in detecting coronary artery disease: analysis of 461 patients". In: *Journal of the American College of Cardiology* 14.6 (1989), pp. 1477–86. DOI: 10.1016/0735-1097(89)90385-9.

[26] Naruepon Kampa. "Renal scintigraphy in dogs". Ph.D. Uppsala: Swedish University of Agricultural Sciences, Aug. 2006.

[27] Linda E. Ketchum. "New Equipment in Nuclear Medicine, Part 1: Solid-State Detectors". In: *Journal of Nuclear Medicine* 39.11 (1998), 15N–36N. ISSN: 0161-5505. eprint: https://jnm.snmjournals.org/content/39/11/15N.full.pdf. URL: https://jnm.snmjournals.org/content/39/11/15N.

[28] Johan Kihlberg. "Magnetic Resonance Imaging of Myocardial Deformation and Scarring in Coronary Artery Disease." Ph.D. Linköping, Sweden: Linköping University, Dec. 7, 2017. ISBN: 9789176854310. DOI: 10.3384/diss.diva-143028. URL: http://urn.kb.se/resolve?urn=urn:nbn:se:liu:diva-143028.

[29] C. Kim et al. "Pharmacologic stress testing for coronary disease diagnosis: A meta-analysis". In: *American heart journal* 142.6 (2001), pp. 934–44. DOI: 10.1067/mhj.2001.119761.

[30] Michael A. King et al. "Chapter 22 - Attenuation, Scatter, and Spatial Resolution Compensation in SPECT". In: *Emission Tomography*. Ed. by Miles N. Wernick and John N. Aarsvold. San Diego: Academic Press, 2004, pp. 473–498. ISBN: 978-0-12-744482-6. DOI: 10.1016/B978-012744482-6.50025-9. URL: https://www.sciencedirect.com/science/article/pii/B9780127444826500259.

[31] Maurits Konings et al. "Non-invasive measurement of volume-time curves in patients with mitral regurgitation and in healthy volunteers, using a new operator-independent screening tool". In: *Physiological measurement* 38 (Jan. 2017), pp. 241–258. DOI: 10.1088/1361-6579/38/2/241.

[32] Elaine Nicpon Marieb. *Essentials of human anatomy & physiology*. San Francisco, CA: Pearson/Benjamin Cummings, 2006.

[33] Spectrum Dynamics Medical. *Data QC and Image Quality Guide*. Confidential material.

[34] Task Force Members et al. "2013 ESC guidelines on the management of stable coronary artery disease: The Task Force on the management of stable coronary artery disease of the European Society of Cardiology". In: *European Heart Journal* 34.38 (Oct. 2013), pp. 2949–3003. DOI: 10.1093/eurheartj/eht296.

[35] Shanthi Mendis et al. *Global Atlas on Cardiovascular Disease Prevention and Control*. 2011.

[36] Emma Menzies-Gow and Christine Spiers. *Rapid Cardiac Care*. 1st ed. John Wiley & Sons, Ltd, 2018. DOI: 10.1002/9781119547808. URL: http://onlinelibrary.wiley.com/doi/10.1002/9781119547808 (visited on 08/29/2021).

[37] Mathew Mercuri et al. "Estimating the Reduction in the Radiation Burden From Nuclear Cardiology Through Use of Stress-Only Imaging in the United States and Worldwide". In: *JAMA Internal Medicine* 176.2 (Feb. 2016), pp. 269–273. DOI: 10.1001/jamainternmed.2015.7106.

[38] Luca Mesin. *Neuromuscular System Engineering*. 2019, pp. 293, 347. ISBN: 978-8-892-36188-1.

[39] P. K. Metha, J Wei, and N. K. Wegner. "Ischemic heart disease in women: a focus on risk factors". In: *Trends in Cardiovascular Medicine* 25.2 (2015), pp. 140–51. DOI: 10.1016/j.tcm.2014.10.005.

[40] A. E. Moran et al. "Temporal trends in ischemic heart disease mortality in 21 world regions, 1980 to 2010: the Global Burden of Disease 2010 study". In: *Circulation* 129.14 (Apr. 2014), pp. 1483–92. DOI: 10.1161/circulationaha.113.004042.

[41] A. Movahed et al. *Integrating Cardiology for Nuclear Medicine Physicians: A Guide to Nuclear Medicine Physicians*. Jan. 2009, pp. 1–544. ISBN: 978-3-540-78673-3. DOI: 10.1007/978-3-540-78674-0.

[42] R. Nakazato et al. "Myocardial perfusion imaging with a solid-state camera: simulation of a very low dose imaging protocol". In: *Journal of nuclear medicine* 54.3 (Mar. 2013), pp. 373–379. DOI: 10.2967/jnumed.112.110601.

[43] R. W. Nesto and G. J. Kowalchuck. "The ischemic cascade: Temporal sequence of hemodynamic, electrocardiographic and symptomatic expressions of ischemia". In: *The American Journal of Cardiology* 59.7 (1987), pp. C23–C30. DOI: 10.1016/0002-9149(87)90192-5.

[44] European Association of Nuclear Medicine. *Myocardial Perfusion Imaging. A Technologist's Guide*. Ed. by Helen Ryder et al. 2014. URL: https://www.eanm.org/publications/technologists-guide/myocardial-perfusion-imaging/.

[45] World Health Organization. *Atherosclerosis*. 2016. URL: https://www.nhlbi.nih.gov/health-topics/atherosclerosis. (accessed: 02.08.2021).

[46] R. Seeley, T. Stephens, and P. Tate. *Anantomy and Physiology*. 6th ed. Chap. 20 "Cardiovascular System: The Heart", pp. 667–709.

[47] Peter F. Sharp, Howard G. Gemmel, and Alison D. Murray. *Practical Nuclear Medicine*. Springer London, 2005. URL: http://link.springer.com/10.1007/b136183.

[48] Leslee Shaw et al. "Prognosis in the era of comparative effectiveness research: where is nuclear cardiology now and where should it be?" In: *Journal of nuclear cardiology* 19.5 (Oct. 2012), pp. 1026–43. DOI: 10.1007/s12350-012-9593-y.

[49] Jinhua Sheng et al. "Hybrid cardiac imaging integrating elliptical orbit SPECT with CT". In: *IEEE Access* PP (Dec. 2019), pp. 1–1. DOI: 10.1109/ACCESS.2019.2960387.

[50] Patmaa Sridharan. "Hybrid CCTA Reading with Integrated Vessel-Specific Calcium Quantification". PhD thesis. May 2016. DOI: 10.13140/RG.2.2.10200.14080.

[51] H. G. Stratmann et al. "Prognostic value of dipyridamole technetium-99m sestamibi myocardial tomography in patients with stable chest pain who are unable to exercise". In: *The American journal of cardiology* 73.9 (1994), pp. 647–52. DOI: 10.1016/0002-9149(94)90927-x.

[52] Roland X. Stroobandt, S. Serge Barold, and Alfond F. Sinnaeve. *ECG from Basics to Essentials*. 1st ed. John Wiley & Sons, Ltd, 2015. DOI: 10.1002/9781119066446. URL: http://onlinelibrary.wiley.com/doi/10.1002/9781119066446 (visited on 08/29/2021).

[53] C. Sylvén. "Mechanisms of pain in angina pectoris - A critical review of the adenosine hypothesis". In: *Cardiovascular Drugs and Therapy* 7.5 (1993), pp. 745–759. DOI: 10.1007/BF00878926.

[54] *Understanding Your Nuclear Medicine Stress Test*. Digirad. June 21, 2018. URL: https://www.digirad.com/understanding-your-nuclear-medicine-stress-test/ (visited on 09/13/2021).

[55] Theo Vos et al. "Global Burden of 369 Diseases and Injuries in 204 Countries and Territories, 1990–2019: A Systematic Analysis for the Global Burden of Disease Study 2019". In: *The Lancet* 396.10258 (Oct. 2020), pp. 1204–1222. ISSN: 01406736. DOI: 10.1016/S0140-6736(20)30925-9. URL: https://linkinghub.elsevier.com/retrieve/pii/S0140673620309259.

[56] Douglas Wagenaar. "CdTe and CdZnTe Semiconductor Detectors for Nuclear Medicine Imaging". In: *Emission Tomography: The Fundamentals of PET and SPECT* (Dec. 2004), pp. 269–291. DOI: 10.1016/B978-012744482-6.50018-1.

[57] Paul Wicker and Sara Dalby. "Anatomy and Physiology: The Cardiovascular System". In: *Rapid Perioperative Care*. John Wiley & Sons, Ltd, 2016. Chap. 17, pp. 78–81. ISBN: 9781119548935. DOI: https://doi.org/10.1002/9781119548935.ch17. eprint: https://onlinelibrary.wiley.com/doi/pdf/10.1002/9781119548935.ch17. URL: https://onlinelibrary.wiley.com/doi/abs/10.1002/9781119548935.ch17.

[58] N. D. Wong. "Epidemiological studies of CHD and the evolution of preventive cardiology". In: *Nature Reviews* 11.5 (May 2014), pp. 276–89. DOI: 10.1038/nrcardio.2014.26.

[59] Habib Zaidi and B. Hasegawa. "Overview of Nuclear Medical Imaging: Physics and Instrumentation". In: July 2006, pp. 1–34. ISBN: 0-387-23854-9. DOI: 10.1007/0-387-25444-7_1.

[60] G. Zeng et al. *Emission Tomography: The Fundamentals of PET and SPECT*. Vol. 23. Elsevier Academic Press, Jan. 2004. Chap. 7, pp. 127–152. URL: http://www.scribd.com/doc/28417300/%20emission-tomography-the-fundamentals-of-PET-and-SPECT.